NASA CONTRACTOR REPORT

RESEARCH AND DEVELOPMENT OF HIGH TEMPERATURE GAS BEARINGS

I - Analysis and Design of Three Gas Bearings for High Temperature Operation

by H. Cheng, D. Wilson, E. B. Arwas, and V. Castelli

Prepared by
MECHANICAL TECHNOLOGY INCORPORATED
Latham, N. Y.
for Lewis Research Center

NATIONAL AERONAUTICS AND SPACE ADMINISTRATION • WASHINGTON, D. C. • NOVEMBER 1969

NASA CR-1476

RESEARCH AND DEVELOPMENT OF HIGH TEMPERATURE GAS BEARINGS

I - Analysis and Design of Three Gas Bearings for High Temperature Operation

By H. Cheng, D. Wilson, E. B. Arwas, and V. Castelli

Prepared under Contract No. NAS 3-9433 by
MECHANICAL TECHNOLOGY INCORPORATED
Latham, N.Y.

for Lewis Research Center

NATIONAL AERONAUTICS AND SPACE ADMINISTRATION

For sale by the Clearinghouse for Federal Scientific and Technical Information
Springfield, Virginia 22151 – Price $3.00

FOREWORD

The research described herein, which was conducted by Mechanical Technology Incorporated under NASA Contract NAS 3-9433, was performed under the project management of Mr. Henry B. Tryon, Space Power Systems Division, NASA Lewis Research Center. The report was originally issued as Mechanical Technology Incorporated Report MTI-69TR21, volume I.

TABLE OF CONTENTS

Table of Contents (Cont'd)

LIST OF TABLES

LIST OF FIGURES

LIST OF FIGURES (con't.)

NOMENCLATURE

C	Radial Clearance, inches.
D	Journal bearing diameter, inches.
d	Thrust plate thickness, inches.
FHP	Friction Horsepower, HP.
f	Radio of actual friction power loss in thrust bearing to couette power loss.
h	Film thickness, inches.
h_{min}	Minimum Film Thickness, inches.
h_o	Thrust bearing film thickness, neglecting distortion effect, inches.
h_p	Pivot point film thickness, inches.
J	Conversion factor, thermal to mechanical energy units $J = 9336 \frac{\text{in lbs}}{\text{BTU}}$
K	Stiffness, lbs/inch (used also to denote dimensionless curvature as defined on Page 47).
K_p	Angular stiffness in the pitch direction, in. lbs/radian.
K_r	Angular stiffness in the roll direction, in. lbs/radian.
K_{xx}, K_{yy}	Foil bearing stiffness, lbs/inch.
k	Thermal conductivity, BTU/in. sec.^{o}F.
L	Length of journal bearing, inches.
ℓ	Length, inches.
N	Angular speed, RPS.
N_p	Pad natural frequency in pitch, RPS.
N_R	Pad natural frequency in roll, RPS.
p_a	Ambient pressure, psia.
q''	Heat flux, BTU/sec.

R	Journal bearing radius, inches. (Also used to denote radius of curvature of thermally distorted thrust plate, inches, as shown on Page 46).
R_i	Inside radius of thrust bearing, inches.
R_o	Outside radius of thrust bearing, inches.
r	Radius, inches.
r_i	Inside radius of shaft, inches.
r_o	Outside radius of shaft, inches.
T	Temperature, ^oF.
t	Thickness, inches.
W	Load, lbs.
W_o	Load capacity of thrust bearing neglecting thermal distortion effects, lbs.
$\bar{W}$	Dimensionless load capacity of thrust bearing, $\bar{W} = W/[\pi \cdot P_a \cdot (R_o^2 - R_i^2)]$
x, y, z	Coordinates, inches.
α	Thermal expansion coefficient, $in/in \cdot {}^oF$.
Δ	Normalized distortion parameter defined on Page 47.
δ	Groove depth, inches.
θ	Angular coordinate, radians.
Λ	Thrust bearing compressibility number, $= 3\mu\omega(R_o^2-R_i^2)/P_a h_o^2$
μ	Absolute viscosity, $lb \cdot sec/in^2$.
τ	Time, seconds.
ϕ	Attitude angle, radians. (Also used to denote heat flow factor defined on Page 50).
ω	Angular velocity, radians/second.

I. INTRODUCTION

The ability of gas-lubricated bearings to operate at elevated temperatures is an important attribute to their utilization in Brayton Cycle machinery for dynamic power conversion in space vehicles, as well as in other high-speed, high-temperature rotating machinery. Since the cycle gas itself serves as the lubricant, there should be, neglecting distortion, no inherent limit on the operating temperature of the bearings, such as exists where oil lubricated bearings are used. Furthermore, since the viscosity of gases increases with temperature, so does the theoretically achievable load capacity of self-acting (hydrodynamic) gas-lubricated bearings.

To date limited advantage has been taken of this property. The gas bearings of the current generation of Brayton Cycle machines are designed to operate at moderate temperatures (generally equal to or less than 500 F) and, more significantly, in a near isothermal environment. To do this, the bearing locations may have to be other than optimum from load sharing and rotor-bearing dynamics standpoints. Certain design complexities, such as the use of heat dams, thermal shunts and local heat exchangers have to be resorted to in order to control the temperature distribution at the bearing locations. Liquid or gas cooling of the bearings has to be used, with a consequent lowering of the thermodynamic efficiency of the system.

The pre-requisites for successful development of uncooled, high temperature gas bearings which, in the interest of improved machine design and thermodynamic efficiency, will be used in future compact Brayton Cycle machines comprise:

(a) gas bearing designs that can tolerate large temperature gradients with minimum distortions and without suffering appreciable loss of load capacity or other static and dynamic characteristics, and

(b) bearing surface materials or coatings that have the desired compabilities at elevated temperatures.

The technology program reported in this two-volume final report was intended to arrive at bearing designs and surface materials or coatings that satisfy these two pre-requisites.

The analytical and design phase of the program comprised the selection, analysis and design of two journal and one thrust bearing configurations that have high potential for operating, without external cooling, in a high temperature, non-isothermal environment. The selection of the bearing configurations was made in an earlier task of the program, based on a screening analysis of various gas bearing types, and it is reported in Ref. 1. The detailed analysis and design of the selected bearing types is given in this volume of the final report. Layout drawings and materials lists for the selected bearing configurations were separately prepared and issued to the NASA.

The parallel experimental phase of the program comprised selection and test of bearing materials and surface coatings. In this phase, three combinations of structural substrate materials and surface coatings were selected for evaluation at 900F. Similarly, a second set of three bearing materials and surface coatings were selected for evaluation at 1400F. The selection of the materials was based on a study of the literature and of the results of related programs. The selected materials and surface coatings combinations were experimentally evaluated at 900 and at 1400F, in both a journal-pad and a spiral-grooved thrust-bearing configurations, under start-stop and high-speed rub test conditions. The results of the materials investigation is reported in the second volume of this final report.

2. SUMMARY, CONCLUSIONS AND RECOMMENDATIONS

2.1 Summary

In summary, the work conducted during the analytical and design phase of the technology program on high-temperature, self-acting (hydrodynamic), gas-lubricated bearings for Brayton Cycle machinery which is reported in this first volume of the final report comprised:

1. A screening analysis of several journal and thrust bearings from the standpoint of their relative merits for operation without external cooling in a high temperature, non-isothermal environment in compact, high-speed rotating machinery. This screening study led to the selection of one "rigid" surface journal bearing concept, one "conformable" surface journal bearing concept and one thrust bearing concept for detailed design and analysis.

2. Design of the selected bearing concepts, including preparation of a detailed layout drawing and materials list for each concept. These layout drawings and materials list have been separately issued to the NASA.

3. Detailed analysis and computation of the performance of the selected bearing concepts, in a high temperature non-isothermal environment and including the influence of thermal distortions, for a specified range of operating conditions.

The materials phase of the program, which has been separately reported in the second volume of this final report, comprised:

1. A review of the literature and of related programs, leading to the selection of three combinations of substrate materials and surface coatings suitable for use in gas-lubricated bearings operating in an inert gas environment at temperatures up to 900 F, and of a similar set of substrate materials and surface coating combinations that are suitable for operation in an inert gas environment at up to 1400 F.

2. Experimental evaluation of the selected materials combinations at their appropriate maximum operating temperature levels (900 F for the first three combinations and 1400 F for the second three). These consisted of a specified set of test conditions that included start-stop rub tests and high speed impact rub tests. In each case the tests were conducted with a journal bearing pad geometry and repeated with a spiral grooved thrust bearing configuration.

2.2 Selected Bearing Types

The three bearing concepts selected from the screening study were as follows:

- "Rigid" Surface Journal Bearing Concept: Foil Supported Tilting Pad Bearing
- "Conformable" Surface Journal Bearing Concept: Foil Bearing with Variable Preload
- Thrust Bearing Concept: Helical Grooved Thrust Bearing with Flexure Supported Stator

The screening study that led to this selection is described in Ref. 1 and a summary of its findings is given in Section 3 of this report. It is desirable to note here, however, that the selection of the bearings listed above is not intended to imply that these are the only appropriate high temperature, non-isothermal gas bearing concepts. Since only one type was chosen in each category for detailed analysis, the selection was based on comparative performance calculations for several bearing types, which were made assuming very severe thermal gradients in the bearing rotor and stator elements.

In particular, in the case of the rigid surface journal bearing, the tilting pad-bearing was selected over other promising bearing types, that included the herringbone grooved bearing. This was done primarily on the basis of the comparative tolerance of each of these two bearing concepts to extremely severe axial thermal gradients. In the presence of these gradients, the tilting pad bearing (by virtue of the ability of the pads individually to roll so as to maintain near parallelism with a thermally coned rotor) was shown to suffer much smaller loss of film thickness than the full cylindrical, herringbone grooved sleeve bearing. This latter bearing, however, has certain advantages primarily from the standpoint of simplicity (as it is of single piece construction and does not require a complex support system) that make it an

attractive back-up bearing concept. This is particularly true in cases where the thermal gradients are less severe than those used in the screening study.

2.3 Principal Conclusions

Gas bearing designs that have high tolerance of thermal gradients, so that they can operate without cooling in compact Brayton Cycle turbomachinery, appear to be entirely feasible. Specifically, the analytical and design phase of the present study has shown:

1. For a 1400 F inlet turbine temperature, the temperature level of the turbine end journal bearing, without cooling provisions, is about 600 F to 800 F, depending on the thermal shielding used and the effectiveness of the thermal shunt.

2. The transient, temperature gradients in the rotor-bearing pads combination are dominated by the heat generated in the bearing film. In general, the journal temperature is higher than the bearing temperature throughout, and the most severe variation in the local shaft to pad temperature differences appear to occur at the steady state condition.

3. In the case of the thrust bearing, very large variations in the thermal differential between the runner and the stator occur during start up.

4. The tilting pad bearing exhibits a very high tolerance of thermal gradients. Large radial temperature differences between the shaft and bearing housing of the order of 400 F can be tolerated by suitable preload design. The stiffness of the preloading spring or flexure has to be selected based on the anticipated radial temperature difference and the allowable limits on preload variations.

5. Where pivots with relative sliding between the members (such as the conventional Hertzian contact pivots commonly used in present-day tilting pad bearings) are not desired, a foil support system can be used as described in Section 5 of this report and in the drawing and materials list prepared for the foil supported tilting pad bearing type. For the elevated temperature condition of interest here (up to 1400 F operating temperature), the system uses 0.020" thick x 0.40" wide Inconel X foils. These provide calculated restraints on the pitch and roll motions of the pads that are about two orders of magnitude smaller than the corresponding stiffnesses of the gas film. This should permit satisfactory, stable operation of the bearing.

6. The foil support does not automatically provide for freedom of motion in the yaw direction. The need for this, for example, to facilitate accurate alignment and preserve this alignment under thermal cycling needs to be experimentally established. For the present, it is felt that freedom of motion in the yaw direction is desirable and provision for it has been included in the design by attaching each pad to its foil support element through a Rene 41 flexure pivot.

7. Detailed performance maps were prepared for the foil supported tilting pad bearing including thermal distortion effects and these confirmed that the loss of load capacity and other bearing characteristics was small, generally of the order of 10 percent or less for the specified conditions ofoperation.

8. A general study of thermal coning and thermal crowning of the shaft, relative to the pads was also made allowing for a wide range of values of axial thermal gradients, and of temperature differential between the journal center and journal ends. The results, shown in Figs. 37, 38 and 39, showed that thermal coning has very little effect on the pivot point film thickness due to the ability of the pads to roll about their points of support to compensate for it. Thermal crowning will, however, result in significant reduction in the pivot film thickness, as illustrated in Fig. 39. Thermal crowning can be limited by continuing the use of a thermal shunt made of copper or other high thermal conductivity material in the rotor (and if needed in the pads also) to minimize the temperature gradients that induce crowning.

9. Review of the present analytical methods for predicting onset of instability in tilting-pad, gas-lubricated bearings showed these to be lagging behind the experimental and field experience. Accordingly, the clearance values (and, hence, the magnitude of preload) used in the field maps was based on prior experimental observations recorded during development of the dynamic simulator of the axial flow turbocompressor (Ref. 2.). This should provide for stable operation of the tilting pad bearing designed herein, however, further combined analytical and experimental analysis of gas bearing stability is needed to obtain a general solution of this problem.

10. A foil bearing was designed with variable preload and performance maps obtained for it over the specified operating range. While this bearing has high stability, it tends to have low radial stiffness unless very high operating preload is used, which increases power loss. With low stiffness, on the other hand, large journal center excursions will be experienced.

11. The presence of large thermal gradients has very little influence on the film thickness of the foil bearing, but it does cause displacement of the journal center.

12. A double acting, helical grooved thrust bearing was designed and analyzed, which allows support of thrust loads in either direction.

13. Thermal gradient effects in the thrust bearing were controlled by: 1. use of a TZM stator which by virtue of its low thermal expansion coefficient (α) and high thermal conductivity (k), suffers virtually negligible distortions, 2. designing the Rene 41 rotor such that the crowning induced by the axial thermal gradients is almost completely compensated for by the dishing of the runner caused by the radial thermal gradients. With these design features, it was concluded that loss of load capacity due to thermal gradients can be limited to the order of 10 percent at normal operating films of the order of 0.001".

The conclusions of the materials phase of the study are separately covered in Volume 2 of this final report. Briefly, however, the preferred materials combination among those tested, at both the 900 and the 1400 F levels was found to be a combination of Al_2O_3 coating sliding against a nickel-chrome bonded chrome carbide coating. The NASA furnished eutectic fluoride film was also found to be effective in preventing surface damage but problems encountered in using this film indicated that more development effort is needed.

2.4 Recommendations

The analytical and design phase of the program has led to certain bearing designs that appear to have a very high potential for satisfactory operation in a high temperature, non-isothermal environment and will not require cooling. It is recommended that, as the next phase of this development, these three bearing

concepts be fabricated and tested under controlled thermal gradient conditions. Simplifications of the bearing designs that have been arrived at here on the basis of analytical and design-room studies should be sought and achieved during fabrication and test.

The recommendations of the materials phase have been separately covered in the second volume of this final report. Briefly, however, these comprise (a) further evaluation and optimization of the use of chrome carbide combinations as surface coatings for high temperature bearings and (b) further development in the areas of composition, application and evaluation of solid lubricant films including the NASA's eutectic fluoride and the Dow Corning ceramic bonded MoS_2 films.

3. SUMMARY REVIEW OF THE SCREENING ANALYSIS

Prior to conducting the detailed analysis of the high temperature non-isothermal gas bearings described in this report, a screening study was made to select the bearing types for the detailed analysis. This screening analysis was conducted as Task I of the overall program and it has been reported in Ref. 1. Here, a brief summary of the results of this preliminary task will be briefly reviewed.

The scope of the screening analysis was as follows:

1. Based on a qualitative assessment of various known journal and thrust bearing types, select four candidate journal bearing types and two candidate thrust bearing types that have most promise for operation in an uncooled environment, under specified operating conditions, (described below) that are characteristic of anticipated, compact Brayton Cycle machinery.
2. Conduct a preliminary (screening) analysis of these bearing types in order to select two journal and one thrust bearing types for detailed analysis and design.

The selection criteria for the screening analysis included:

a. large value of the minimum film thickness
b. high stability threshold during both steady-state and transient conditions
c. tolerance of steady-state and transient thermal gradients
d. thermal tracking ability
e. low power loss

Prime consideration was to be given in the comparative studies to the tolerance of the bearings to transient and steady-state thermal gradients.

The operating conditions that were used for the comparative studies of bearing performance were:

a. shaft diameter: 2 inches

b. shaft speeds: 10,000 to 50,000 rpm
c. ambient temperatures: 900F to 1400F
d. temperature gradients: up to 400F between support mount and shaft
e. load (total/length x diameter): zero to 5 psi
f. ambient gas pressure: 5 to 25 psia (compressor inlet)
g. cycle fluid: air, argon and krypton
h. design life, min.: 50,000 hours

The outcome of the screening analysis was to be two preferred journal bearing concepts and one preferred thrust bearing concept. It was,however, required that at least one of the journal bearing concepts be of the conformable type. It was also required that pivots having relative sliding between the bearing pads and the mounts (such as the Hertzian contact pivots used in conventional tilting pad bearings) not be used.

3.1 Journal Bearings Concepts Considered during the Screening Study

From a qualitative assessment of eight gas lubricated journal bearing types the following four were selected for the screening analysis:

1. Wire supported tilting pad bearing
2. Herringbone grooved bearing supported in tangential flexures
3. Hydrostatically supported full cylindrical bearing
4. Foil bearing with variable preload

Some of the factors favoring these bearing choices were as follows:

The tilting pad bearing is the most widely used self-acting gas bearing in high speed turbomachinery. This is principally because of its excellent stability characteristics and inherent self alignment capability. Furthermore, the fact that the bearing consists of a number of individually supported pads, is advantageous from the standpoint of tolerance of thermal gradients. By use of preloading,variations in bearing clearance due to differential thermal (and centrifugal) growths of the rotor relative to the bearing housing can be minimized. Furthermore, the ability of the pads individually to align with the shaft surface allows them to adjust to conical journal distortions induced by axial thermal gradients, thus maintaining a uniform film thickness in the

axial direction. Conventionally, the tilting pad bearing uses Hertzian contact pivots (e.g. a ball and socket arrangement) to support the individual pads and allow them freedom to pitch, roll or yaw, in response to translatory and conical orbits of the shaft. In the present design study, however, this type of support was precluded. Instead, an alternate support scheme was sought which would allow the desired freedom of motion of the pads but which would not have its elements subjected to relative sliding in the inert gas, high temperature environment. A wire support system (later changed to one utilizing 0.4 inches wide x 0.020 inches thick Inconel X foils) was selected as providing minimum restraint on the freedom of motion of the pads in both the pitch and roll directions, with relatively low stress levels (less than 20,000 psi) in the support elements.

The herringbone grooved bearing has achieved increasing importance in recent years as a practical gas bearing for high speed turbomachinery. It is produced by inserting shallow herringbone grooving in either the stator or rotor elements. The grooving makes the bearing operate as a zero flow, viscous compressor, with large pressures generated around the circumference of the bearing, even when the journal is running concentric within the bearing clearance. It has been shown both analytically and experimentally that this bearing has both high radial stiffness and a high stability threshold. Unlike the tilting pad bearing it is of a simple, one-piece construction. The herringbone grooving imposes no serious manufacturing problem, even for small or moderate size bearings since it can be inscribed in the rotor. The grooves can be inscribed by machining, or, preferably, they can be achieved by coating the rotor through an appropriate screen, after which the lands are ground to achieve the desired groove depth. The bearing is generally supported in a diaphragm to provide some alignment capability. For the present study, where large thermal gradients between the rotor and the bearing housing are present, the bearing support comprised a set of tangential flexures to provide high radial stiffness, while allowing the bearing to grow radially, relative to its housing, in response to temperature differences between it and the housing. Furthermore, by using a relatively thin bearing sleeve(and since the tangential spoke support reduces the conductive heat path to the housing) the bearing should be capable of tracking the rotor temperature during thermal transients.

The third, rigid surface bearing concept comprised a cylindrical bearing supported on a hydrostatic gas film. The selection of this bearing was based on earlier theoretical analysis and experimental studies that showed that the stability threshold of a plain circular, gas bearing can be considerably enhanced by providing external damping. For low temperature applications, this principle was applied successfully by supporting the gas bearing in an elastomer ring. For operation at elevated temperatures, the external damping can be provided by supporting the bearing on a hydrostatic film. Self-alignment was provided by spherically crowning the hydrostatic support. Tolerance of thermal gradients was sought by using a thin, low mass bearing sleeve and by flexibly attaching the hydrostatic seat to the housing. The hydrostatic support was to be designed for low flow and supplied either from compressor discharge or by gas bled off from the hydrodynamic film. During the screening study, a herringbone grooved bearing was used in place of the plain circular one to further enhance its stability.

The above three bearings are all of the "rigid" geometry type so that only one of these could be selected at the completion of the screening analysis. The "conformable" geometry bearing reviewed in the screening study was a foil bearing. This bearing type has the advantage of very high stability, due to the fact that the foil "pads" are nearly massless. A variable preload feature was incorporated in the bearing to minimize pad load variations due to large temperature differences between the rotor and the housing to which the foil ends are attached.

3.1.1 Preliminary Analysis

In order to perform the comparative calculations for the selected bearings, the following preliminary work was conducted.

a. an approximate thermal analysis was made from which the temperature distributions in the rotor and bearings were calculated over the transient from start up to steady-state conditions. This calculation was made for very severe operating conditions, assuming a step jump in the turbine temperature to 1400F at start up. The calculations indicated that during the transient, the difference between the axial thermal gradients in the shaft and in the bearing at the turbine end may be as high as 50 F/inch.

b. the computer programs for tilting pad and herringbone grooved bearings were modified so that: (1) the thermal distortions in the shaft and bearings are computed for any given temperature distributions in the shaft and bearings, and (2) the bearing performance is calculated for the distorted film shape.

3.1.2 Results of the Comparative Performance Calculations

a. The performance characteristics (film thickness, power loss and film stiffness) were first calculated and compared for the four journal bearing concepts noted above, for the steady-state operating conditions and in the absence of thermal distortions. These results did not show any overriding advantage for one bearing over the others.

b. The load capacity reductions due to thermal distortions under thermal transients were then calculated, using the temperature distributions obtained from the transient thermal analysis and using the bearing performance computer programs for thermally distorted film shapes. These calculations were made for both the tilting pad and the herringbone grooved configurations. The results, shown in Figs. 1 through 4, showed that the fully cylindrical herringbone grooved bearing suffers a much higher loss of film thickness than does the tilting pad bearing. For the most severe temperature gradients during the transient, the herringbone grooved bearing was found to lose as much as 79 percent of its minimum film thickness, whereas the loss in the tilting pad bearing was on the order of 33 percent. Physically, the reason for this is as follows. The axial thermal gradients produce a tapered film clearance along the bearing. Accordingly, in the case of the herringbone grooved bearing, the clearance is small at the turbine end and large at the opposite end of the bearing. At the turbine end, the clearance ratio was reduced to 0.0003"/", from its mean design value of 0.0007 "/" due to the fact that the shaft is about 50°F higher in temperature than the bearing at this end. The minimum film thickness at that end is correspondingly very small (0.11×10^{-3} inches, compared to 0.53×10^{-3} inches at the mean clearance value)*. In the case of the tilting pad bearing, on the other hand, while there is a comparable loss in the difference between the pad and shaft curvatures, the pads are free to roll about their supports,

* at 50,000 rpm, 5 psia ambient and 12 lb load

thus tending to more nearly equalize the actual bearing clearance along the length of the bearing. The use of individual pads, with freedom of pitch and roll motions, therefore, offers an important advantage, where large temperature differences are anticipated between the bearing and the shaft.

c. A stability investigation was conducted for herringbone grooved bearings, over a wide range of the geometrical parameters of the bearing as tabulated below. Based on this and on the speed and ambient pressure ranges of the operating conditions specified for this study, 10,000 to 50,000 rpm and 5 to 25 psia respectively, the clearance ratio for the herringbone grooved bearing was set at 0.7×10^{-3} inches/inch. This is the largest clearance that can be used without encountering instabilities within the operating range.

FULLY GROOVED SPIRAL GROOVED JOURNAL BEARING (Grooves Rotating, L/D = 1)

Geometry	h_g/h_r (groove depth ratio)	a_g/a_r (groove width ratio)	(groove angle)
(A)	2.1	1.0	32.8°
(B)	2.1	0.5	32.8°
(C)	2.1	2.0	32.8°
(D)	2.1	1.0	25.0°
(E)	2.1	1.0	45.0°
(F)	1.5	1.0	32.8°
(G)	3.0	1.0	32.8°

d. A further stability analysis was made for the herringbone grooved bearing under zero load and with the thermally distorted film profile to establish whether the bearing continues stable, despite the thermal distortions. This calculation was made using an orbital program and the result is illustrated in Fig. 5. It was found that the journal center trajectory did not spiral out, thus indicating that operation continues stable.

e. The tilting pad bearing has inherently a high stability threshold due to the absence of a tangential force on the shaft (i.e. the attitude angle is zero degrees). Based on the experience gained with the Brayton cycle

axial-flow turbocompressor simulator developed and tested at speeds up to 60,000 rpm for the NASA (Ref.2), a clearance ratio of 0.7×10^{-3} to 0.8×10^{-3} inches/inch is satisfactory from stability standpoint for the operating conditions specified in this study.

f. With the additional damping provided by hydrostatic mount, the clearance ratio of a herringbone grooved bearing can be increased to about 1×10^{-3} inches/inch still maintaining stability for the operating conditions specified for this study. The hydrostatic mount, however, is a penalty due to additional complexity and due to its requiring pressurized gas either from the compressor, or from the hydrodynamic bearing film. The latter reduces the load capacity of the hydrodynamic bearing.

3.1.3 Conclusions of the Journal Bearings Screening Analysis

The principal conclusions of the journal bearing analysis, with regard to the choice of bearings for the detailed analysis and design were as follows:

a. Rigid surface journal bearing concept

Both the tilting pad and the herringbone grooved configurations can be designed for high temperature, non-isothermal applications over the specified range of operation conditions, from the standpoints of load capacity and stability. The herringbone grooved bearing has the advantages of construction simplicity and slightly (about 10 to 20%) less power loss. The tilting pad bearing, however, has substantially better tolerance of large thermal gradients, as illustrated by its much smaller loss of minimum film thickness in the thermally distorted condition. This is an inherent advantage that is due to the fact that the bearing consists of individual pads that freely pitch and roll to compensate against loss of clearance at the bearing ends. This greater tolerance of thermal distortions gives the tilting pad bearing an added measure of reliability in non-isothermal environment and makes it the preferred, rigid-surface journal bearing concept for high temperature applications.

Wire (or foil) support of the tilting pad bearing was preferred over radial or tangential flexures because it combined a high strength support system with very small restraint on the freedom of motion of the individual pads.

The foil supported tilting pad bearing was, therefore, the "rigid surface" grooved bearing concept selected for detailed analysis and design.

b. Conformable journal bearing concept

The foil bearing with variable preload feature to compensate for differential thermal growths between the rotor and the anchor points of the foil in the bearing housing was selected as the "conformable surface" journal bearing concept selected for detailed analysis and design.

3.2 Thrust Bearings Selection for the Screening Study

The two bearing types selected for the screening study were:

1. Flexure mounted spiral groove bearing
2. Flexure supported tilting pad bearing

Thus, a full annular ring type of thrust bearing and a thrust bearing comprising a set of individually supported pads were considered. The full, annular ring type of bearing has the advantage of higher load capacity, but it is more susceptible to loss of load capacity in the event of thermal distortions. Conversely, the tilting pad bearing,consisting of a number of individually supported sector shaped pads, exhibits good tolerance of thermal gradients, but has a smaller load capacity potential.

For the annular type bearing, the helical grooved bearing was selected because of the fact its performance is very nearly independent of gas compressibility effects up to very high values of the compressibility number (Λ). Particularly, in the end of the specified speed range (up to 50,000 rpm maximum) and the low end of the specified ambient pressure range (down to 5 psia minimum), it has a higher load carrying ability than other known self-acting, gas-lubricated thrust bearings. It has also a record of successful applications in gas-lubricated Brayton cycle units, motor driven circulators and other, similar rotating machinery.

3.2.1 Results of Comparative Performance Calculations

The heat transfer analysis indicated that the thermal gradients in the thrust bearing plate and thrust runner will be governed principally by the heat generated in the bearing, rather than by the heat conducted to the bearing region, along the rotor.

The screening analysis was made for a 4-1/2"O.D. x 2" I.D. thrust bearing size, assuming an operating speed of 50,000 rpm and a minimum film thickness of 0.001". For a viscosity of 6×10^{-7} lb.sec/in^2, the load capacities of the two bearings neglecting thermal distortions were calculated to be:

Herringbone grooved bearing at P_a = 5 to 15 psia:	110 lbs
Tilting pad bearing at 15 psia:	33 lbs
Tilting pad bearing at 5 psia:	18 lbs

The calculations were then repeated for the same operating conditions, but now allowing for thermal distortion effects. The calculations were made for six materials combinations indicated from a separate study of high temperature bearing materials conducted under another task of the program. The results of the calculations are tabulated below.

Material Combination (stator vs rotor)	Herringbone Grooved Bearing at 5 to 15 psia ambient (lbs)	Tilting Pad Bearings at: 15 psia ambient (lbs)	5 psia ambient (lbs)
TZM vs TZM	92	33	18
AISI 4340 vs AISI 4340	38	33	18
TD Nickel vs Haynes 25	31	33	18
Rene 41 vs Rene 41	24	33	18
A 286 vs A 286	21	33	18
Haynes 25 vs Haynes 25	19	33	18

In the above table, account was taken of the reduction in load capacity due to thermal distortion in the case of the spiral groove bearing, but neglected in the case of the tilting pad bearing. Furthermore, no allowance was made for design features to minimize thermal distortions* and hence for improving load capacity in the case of the spiral groove bearing. The spiral groove bearing was, therefore, judged to be superior from a load capacity standpoint. The spiral groove bearing has the further advantage of construction simplicity, being essentially a flexibly supported annular plate. The tilting pad thrust bearing on the other hand requires a load equalizer mechanism, which is typically a double row of pivoted or flexure supported leveling links.

*(The development of such features, which would significantly reduce the loss of load capacity due to thermal distortions, would be one of the principal objectives of the final design task.)

It was noted also, that the thermal distortions and, hence, the loss of load capacity, is a function of the ratio of the coefficient of thermal expansion of the material (α) to its thermal conductivity (k). Figure 6, reproduced here from Ref. 1 is a plot of the calculated load capacity versus (α/k).

3.2.2 Conclusions of the Thrust Bearing Screening Analysis

In view of its much higher load capacity potential, the spiral grooved thrust bearing, with a flexurally supported stator was selected for the detailed analysis and design. As noted in Ref. 1, however, the emphasis on this design would need to be placed on materials selection and design features to minimize thermal distortions.

3.3. Minimum Lift Off Speed in the Journal Bearings

A requirement of the program was to establish the minimum desirable level of ambient pressure in the bearing cavities at start up. In order to establish this, the lift off speed was calculated assuming a starting load of 5 lbs supported on a 2" diameter x 2" long journal bearing. The calculations took account of slip flow at low ambient pressures using the method and data of Ref. 17. The calculations were reported in Ref. 1. The results are plotted in Fig. 7, reproduced here from Ref. 1. It will be noted that the speeds required to achieve pivot film thickness in the range of 0.1 to 0.2 x 10^{-3} inches, start to rise very sharply at ambient pressure below about 1.6 psia. Thus, it is recommended that the ambient pressures in the bearing cavities be brought to at least 1.6 or, preferably, about 2 psia prior to hydrodynamic starts.

4. TRANSIENT THERMAL ANALYSIS

In studying the performance of gas-lubricated bearings for high-speed, high-temperature turbomachinery, it is necessary to determine both the transient and steady-state temperature distributions in the journal and thrust bearing regions. These temperature distributions are used to calculate the corresponding thermal distortions of the bearing elements and, hence, to establish their effect on the performance characteristics of the bearings. The temperature distribution in any given system will depend on a number of factors including the temperatures of the aerodynamic and electrical components, the gas flow paths and velocities, the heat generated on the bearing films, the windage losses, the cooling provisions, the materials used, the mechanical design of the machine including the heat dams and thermal shunts and others. Accurate determination of thermal maps for the compact, high-temperature, Brayton Cycle machines is expensive and time consuming, however, the calculation procedures and computer programs required have been developed and are available. Such thermal maps were obtained, for example, during development of the current generation of Brayton Cycle machines, including the NASA's axial flow turbocompressor and the turboalternator, as well as the radial flow turbocompressor and the single shaft Brayton Rotating Unit (BRU). In all these machines, however, either gas or liquid cooling was provided for each bearing to maintain the gas bearing temperature at or below 500F and to minimize thermal gradients.

As part of the present study, thermal calculations were made to determine the range of bearing temperatures and, more importantly, bearing temperature gradients that would be anticipated if the cooling provisions were omitted. These calculations were made for the full transient from start-up of the machine, until achievement of steady-state thermal distribution. An approximate thermal analysis was used, as described below and in Appendix A, since the purpose of these calculations was to investigate the effect of eliminating bearing cooling provisions on the temperature distribution in the bearing area, rather than on establishing the exact thermal maps for a specific machine.

4.1 Rotor-Bearing Configuration Used for the Transient Analysis

The dimensions of the rotor-bearing system used for studying the transient temp-

erature of uncooled journal and thrust bearings are shown in Fig. 8(a). It consists of an integral shaft with a turbine disk attached at one end and a compressor at the other end. The shaft is supported radially by two journal bearings and is held axially by a double-acting thrust bearing located near the compressor wheel. A copper shunt is used between the two journal bearings in order to reduce the local axial temperature gradient of the shaft at the two journal bearings.

The choice of the turbine and compressor disk sizes, overall axial dimensions, and journal and thrust bearing sizes are typical of current practice in the 8 to 10 KW NASA Brayton cycle turbomachinery developed to date.

4.2 Conditions and Assumptions of the Analysis

The analysis was made, for the following conditions:

1. The system is initially at a uniform temperature (assumed to be 100F)
2. At time τ = 0, the face of the turbine disk is subjected to turbine inlet gas at 1400F. (The compressor outlet temperature was assumed to be 250 F).
3. Heat is generated in the bearings at a rate corresponding to 50,000 rpm and film thicknesses of 0.001 inches in each journal bearing, 0.001 inches in the active thrust bearing face and 0.003 inches in the reverse thrust bearing face.

The heat transfer equations were solved repeatedly, at time increments of 250 seconds* and the temperature map in the system obtained for each of these increments, until steady-state conditions were achieved.

The simplified heat transfer analysis that was made used the following assumptions.

1. Temperature distributions are axisymmetric (i.e. the temperatures are uniform about the axis of rotation).

* except for the first 250 seconds which were divided into 5 increments of 50 seconds each, and the temperature distribution calculated at each of these increments.

2. Radiant heat transfer was neglected
3. The enclosure temperature was treated as uniform at each time step and governed by the overall heat balance for each time step.
4. The turbine and compressor wheels were represented by thin disks of uniform thickness.

Writing the finite difference approximations for the heat transfer equations of the turbine disk and thrust bearing in the radial direction and for the rotor in the axial direction, a set of 3 x 3 matrices are obtained and the method of Ref. 18 is used to calculate the transient temperature distribution at each time step. The thermal analysis and the derivation of the matrices are given in Appendix B.

4.3 Results

Figure 8(b) shows the thermal conductivity and the surface convective heat transfer coefficients used in the calculation. The thermal conductivities used for the rotor elements are those for a high temperature alloy such as Rene 41. A TZM thrust bearing housing was assumed, since TZM has a very low value of the ratio $(\alpha/k)^*$ and, thus, suffers very low distortion making it an excellent material of construction for the stator of gas lubricated thrust bearings operating at elevated temperatures and in the presence of high thermal gradients.

The calculations were made for three cases. In Case A, a 0.25" thick annular copper shunt (r_p-r_s) in Figure 8(a) was assumed and the convective heat transfer coefficient on the back face of the turbine wheel (H_A in Fig.8(b)) was assumed to be 2 BTU/(hrxft^{2}x$^\circ$F).

The transient and steady-state temperature distribution in the shaft between the back face of the turbine and the thrust runner are shown in Fig. 9 at 250, 500, 3000 and 5500 seconds after start up. At 5500 seconds, the temperature distribution no longer varies with time and is considered to have reached the steady-state condition. As seen in Fig. 9, the steady-state temperatures for both journal bearings are under 600 F and the axial thermal gradients are moderate.

* where α is the coefficient of thermal expansion and k is the thermal conductivity.

In assessing the performance of the gas film during thermal transients, two effects of temperature gradients and consequent thermal distortions have to be considered. The first of these is the change in the operating bearing clearance due to the temperature difference between the rotating journal and the bearing housing to which the individual pads are attached (as well as any difference in thermal expansion coefficients if dissimilar materials are used). The flexure supports of the pads and preload mechanism, if any, have to be designed so as to control the change in operating clearance (and, hence, the change in preload), to keep it within tolerable limits. The second effect is the change in the difference between the radii of curvature of the pads and of the rotating journal, due to the temperature difference between the journal and the bearing pads (as well as any difference in thermal expansion coefficients if dissimilar materials are used). Furthermore, this difference in radii of curvature will, in general, vary axially, i.e. along the length of the bearing. Figures 10 and 11 show the axial temperature distributions in the pads and in the rotating journal at four time intervals during the transient. It is seen that the pads track the shaft temperature fairly well. In no instance does the local pad to shaft thermal differential exceed 40 F. Furthermore, this thermal differential does not exhibit wide variations axially, i.e. along the length of the bearing.

Temperatures in the thrust runner and stator during transients are plotted in Figs. 12 and 13. These curves show that during start up, the rotor is considerably hotter than the thrust bearing. As the heating continues, the temperature of the stator catches up with the rotor temperatures and eventually rises above it. The stator temperature varies very little in the radial direction because of the high thermal conductivity of TZM. However, large radial temperature gradient exists in the runner since most of the heat generated in the gas film is carried into the shaft by conduction.

It should be noted that Case A represents a rather ideal condition where the thermal shield at the turbine end was assumed to be very effective and where the conduction through the shaft was highly efficient because of the thick copper shunt.

A second case, Case B, was then run, reducing the effectiveness of the thermal

shielding of the turbine wheel, by increasing the surface heat transfer coefficient H_A from 2 to 10 BTU/hrxft^{2}x$^\circ$F. The same 0.25" thick copper shunt was retained.

The results of Case B illustrated in Fig. 14, show that the final, steady-state temperature of the turbine end journal bearing increased to 640 F, (from its value of 580F in Case A).

In Case C, the effect of copper shunting is investigated by reducing its thickness from 0.25 inches to 0.05 inches. Other conditions in Case C are the same as Case A. As shown in Fig. 15, the increase in thermal resistance in the axial direction causes the steady-state shaft temperature at the turbine end bearing to increase from about 580 F to about 780 F. Moreover, the temperature rise at the center of the journal bearing length is more pronounced than in Case A, and this will cause the shaft to crown at the journal bearing and may reduce the gas film thickness appreciably. The effect of shaft crowning on the tilting pad gas film performance is discussed in detail in Section 5 of the report.

From the foregoing results, the following conclusions are reached:

a. The temperatures of uncooled journal and thrust bearing can be maintained at a level considerably lower than the turbine inlet temperature by effective thermal shielding and shunting of the shaft. For example, the maximum temperature of the turbine end journal bearing for a turbine inlet temperature of 1400 F can be maintained in the range 600 F - 800 F depending on the thermal shielding and shunting design, but without external cooling.

b. At high surface speeds (about 5000 in/sec in the instance considered here), the transient temperature gradients are dominated by the heat generated in the gas film rather than by the heat conducted from the hot turbine wheel. Under such conditions, the journal bearing temperature is always higher than the shaft temperature and the most severe axial variation of the thermal differential between the shaft and bearing occurs at steady-state rather than at any stages during start up.

c. For the thrust bearing, the variation of the thermal differential between the runner and stator during start up is much larger than that in the journal bearings.

5. THE FOIL SUPPORTED TILTING PAD BEARING

Based on the results of the screening analysis (described in detail in Ref. 1 and summarized in section 2 of this report), the "rigid" journal bearing concept selected for detailed analysis was of the tilting pad type, but excluded the conventional, Hertzian contact type of pivots. The exclusion of pivots having relative sliding motions between the pads and mounts was in accordance with the NASA specifications for this study.

The tilting pad type of bearing was selected because the screening analysis showed it to have much higher tolerance of thermal distortions than the other bearing types investigated. Flexure mounting of the individual pads was, however, found to provide higher than desirable restraint in the freedom of motion of the pads, with adverse effects on the stability threshold of the bearing. Review of other support means, led to the selection of foil supported tilting pad bearings.

The foil supports for the bearing pads, described herein, offer very low restraint to the freedom of motion of the pads – the restraining moment in each axis is about two orders of magnitude smaller than the angular stiffness of gas film in the corresponding axis. Thus, the dynamic performance of the foil supported bearing should be very nearly the same as that of the conventional pivoted pad bearing. This was achieved at the cost of some complexity in design. It should be noted, however, that the work to date on the design of a foil supported tilting pad bearing has been entirely analytical. As the design is reduced to practice through manufacture and test, design simplifications that do not materially reduce its performance should be effected. It should be noted also that the steady-state and dynamic characteristics calculated and presented in the latter part of this section of the report are applicable to bearings with conventional pivots as well as to the foil supported tilting pad bearing since the restraints on pad motion are in both cases very small, compared to the angular stiffnesses of the gas film.

5.1 Design Specifications

The design specifications established by the NASA for this study were as follows:

a. Shaft diameter: 2 inches
b. Shaft speeds: 10,000 to 50,000 rpm
c. Ambient temperatures: 900 F to 1400 F
d. Temperature gradients: up to 400 F between support mount and shaft
e. Unit load (total load/length x diamter): 0 to 5 psi
f. Ambient gas pressure: 5 to 25 psia (compressor inlet)
g. Cycle fluid: air, argon and krypton
h. Design life objective: 50,000 hrs.

5.2 Bearing Dimensions

The bearing dimensions used for the study were as follows:

a. Shaft diameter: 2 inches
b. Pad to shaft clearance radii at design point(i.e. ratio of the difference between the pad and shaft ratio of curvature, to the radius of curvature of the shaft): 0.0025 inches/inch.
c. Length to diameter ratio: 1
d. Pad wrap angle (i.e. angular length of pad): 85 degrees
e. Pivot position (i.e. ratio of angular distance from leading edge of pad to pointof attachment to the foil support, to the total arc length of the pad): 0.65
f. Pad thickness: 0.10 inches

5.3 Details of Mechanical Design

The final bearing design of the foil-supported, tilting-pad bearing is detailed on Fig. 16. The design and materials of construction were selected to permit operation of the bearing at ambient temperatures as high as 1400 F.

5.3.1 Bearing Pads

The bearing pads are of the conventional four pad type, designed to minimize pad inertia, similar to the ones used in the NASA's axial flow turbocompressor

simulator and the turboalternator. The pad thickness is 0.10 inch, which gives it ample rigidity, with low pad weight and inertia.

5.3.2 Foil Support Design

Each pad is attached to an Inconel-X flexure strip, 0.020 inches thick x 0.40 inches wide. The pads are attached to the foil through a cantilever type flexure which provides the freedom of motion in the yaw direction. This cantilever type flexure and the method of attachment are described later in this section.

The foil type, Inconel flexure strip permits movements of the pad in both the pitch and roll directions. The restraint imposed by the foil in the pitch direction is approximately 67 inch1bs/radian while the roll resistance is less than 18 inch1bs/radian.

The restraints were computed considering the foil as a simply supported beam. In the case of pitch, a beam supported at either end (with movable supports) subjected to an applied moment at the center was considered. Following this approach the foil restraint in the pitch direction becomes:

$$m/\theta = \frac{12}{\ell} EI = K_p$$

$$I = \frac{bh^3}{12}$$

$$K_p = -\frac{bh^3}{\ell} E \quad \frac{in1b}{rad}$$

$$K_p = -\frac{4 \times 10^{-1} \cdot 2^3 \times 10^{-6}}{1.386} \times 29 \times 10^6$$

$$K_p = 67 \quad \frac{in1b}{rad}$$

where:
- m = applied moment (in.lbs)
- θ = angular displ.(rad.).
- ℓ = foil length between supports (inches)
- E = foil modulus of elasticity (lbs/in^2)
- I = cross sectional inertia (in^4)
- b = foil width (in)
- h = foil thickness (in^3)

In the roll direction of the pad, the foil was treated as a cantilever with an applied moment across the width of the foil. For this case:

$$\frac{M}{\theta} = \frac{0.33\ G\ h^3 b}{\ell/2} = K_R$$

where G is the foil torsion modulus (lb/in^2)/radian

$$\text{Hence, } K_R = \frac{0.33 \times 11.5 \times 10^6 \times 2^3 \times 10^{-6} \times 0.4}{0.693}$$

$$K_R = 18 \text{ in.lbs/radian}$$

These angular restraints of the foil supports are small compared to the angular stiffnesses of the fluid film. For the 2" diameter x 2" long bearing considered here, the values of the fluid film stiffness of the pads at 50,000 rpm in the pitch direction ranged from 2410 inlbs/radian for the preload* pads to 9380 inlbs/radian for the other pads. In the roll direction, the corresponding fluid film stiffness for each pad ranged from 3720 inlbs/radian for the preload pads to 17,250 inlbs/radian for the loaded pads. Thus, the restraints offered by the foil or the pitch and roll directions are small compared with the corresponding film stiffnesses and should permit accurate tracking of rotor orbits, as required for stable operation. The foil support is, however, relatively rigid in the yaw direction. Freedom of motion of the pads in the yaw direction is important principally from the standpoint of permitting accurate alignment of the pads both at assembly and following thermal cycling. Whether or not special provisions for insuring low restraint in the yaw direction are necessary is not readily determinable in a design study such as the present one. Experimental evaluation of the bearing would be desirable at elevated temperatures and under thermal cycling. For the purpose of the present design study, however, a provision for angular freedom of the pads in the yaw direction has been provided by attaching each pad to its foil support through a flexure pivot as illustrated in Fig. 16. This flexure is made of Rene 41 for high temperature opration. It permits freedom of motion of the pad in the yaw direction with a restraint of 1.6 in.lbs/radian. The flexure is rated for infinite life when cycled within $\pm$ 0.08 radians under the full pad load.** The flexure is rated at 60 lbs. load, which is well above the maximum pad load

* The pair of adjacent pads which are supported on radial springs (See Fig. 16) are referred to here as the "preload" pads since their spring supports serve to impose a radial preload on the bearing.

** The actual yaw oscillations of the pads or a tilting pad, gas bearing in operation are of the order of 10^{-4} to 10^{-3} radians.

of 34 lbs. (maximum external load plus maximum preload). The attachment of the pad flexure is by electron beam welding. The assembly is, in turn, electron beam welded to the 0.020 inches thick by 0.40 inches wide Inconel X foil which has been preformed to the necessary shape.

In order to insure long life at elevated temperatures, the stresses in the foil and support members were maintained below 10,000 psi. A creep rate well below 10^{-3} percent per 1000 hours is given in the manufacturers' literature on the selected materials at 1200 F for periods to 10,000 hours, at the design values of stress levels.

5.3.3 Preload Design

To complete the pad assembly, the flexible preformed foil sheet is assembled to pins at either end. The pin at one end is pressed in a clamp arm. Essentially this clamp, which contains a threaded stud at the other end, permits adjustment of the pad position. This is accomplished by changing the adjusting cap position on the threaded screw. By threading the cap further on to the screw, the pad will move radially inward and unscrewing it will move the pad radially outward. A dummy shaft, or the final shaft, containing discs to simulate the compressor and turbine wheels may be assembled in the bearings and positioned to running position with shims between the wheel OD and housing ID at either end. The adjusting cap for each of the bottom pads can adjust to position the pads in contact with the shaft. The upper pad adjusting caps are used to adjust the compressed height of the preload springs to insure a high preload. After all the adjusting caps are locked into position, an unloading bellows is installed on the preloaded upper pads. Pressure applied to the bellows increases the preload to the desired value.

The preload spring has a stress of 50,860 psi at room temperature and approximately 39,000 psi at 1400 F. This is well within material stress capabilities over the temperature range although some spring relaxation may be encountered over periods in excess of 1000 hours at temperatures above 1200 F.

A 20 percent change in spring preload height from material creep, will result in a 2 lb. reduction in load, for a design value of preload of about 16 lbs, which will not impair operation.

A further change in preload is possible due to thermal gradients between shaft and the housing mounting point. Due to the fact, that the bottom pads are fixed, the upper pads must assume any required variations. It should be noted, however, that high shaft temperatures will cause high pad temperatures such that the most significant gradient will occur primarily along the foil support. If the average foil temperature is assumed to fall midway between the shaft temperature and the housing temperature, then the change in foil length necessity to accept a 400 F temperature differential between housing and shaft is $.16 \times 10^{-3}$ inches. This implies that there essentially is no change in preload due to thermal gradients at steady state conditions. Consequently, it was assumed that under transient conditions the required change in foil length remained below 1×10^{-3} inches, representing a load change of 3.5 lbs.

In order to maintain the pad natural pitching frequency above the operating speed, it is necessary to maintain the pad preload above 12 lbs. Considering both long term creep and the very high radial temperature gradients, the design maintains this minimum required preload. It is also desirable to maintain the preload below 20 lbs to limit the pad eccentricity and power loss. The design also falls within this requirement up to a radial temperature differential of 200 F between the pad and the foil support if the initial preload is set at 16 lbs.

5.4 Tilting Pad Journal Bearing Analysis

The methods in determining the steady-state performance of a multi-pad tilting pad journal bearing have been highly developed (Refs. 3,4,5). A common procedure is to first calculate charts for the performance of the individual pad and then to determine the multi-pad performance of the total journal bearing by interpolation of these data manually or, more generally, using a computerized procedure.

While the above conventional procedure works well for an undistorted pad, it becomes somewhat impractical for pads with a distorted geometry mainly because for each distorted geometry, a new set of pad data is required in order to determine the multi-pad journal bearing performance for a given operating

condition. If performance of several distorted pads is to be calculated, the quantity of individual pad data needed will be enormous. For this reason, an alternative approach was adapted here to calculate directly the steady-state performance of the complete foil supported tilting pad journal bearing.

Briefly, the alternative method solves the dynamics of the single pad by considering the center of shaft to be fixed. The attitude of the pad is described by the radial displacement of the pivot position, the pitch angle, and the roll angle, all of which are calculated simultaneously with the gas film forces and moments, which are governed by the transient Reynolds equation. For a given load, pitch and roll moments, the program calculates the equilibrium attitude of the pad from a given initial attitude from the pad equations of motion and the transient gas film equation. This approach for seeking steady-state solutions is expensive in computer time because a time consuming, matrix inversion is required at each time step through the transient. It is, however, the most practical method to use, when the thermal distortion of the individual pads has to be calculated and factored with the bearing performance calculations. Furthermore, recent advances in development of a semi-implicit method for treating the time transient gas lubrication equation (Ref. 19), have resulted in about an order of magnitude reduction in computer time requirements. For the thermally distorted pads, the performance for the multi-pad bearing, including thermal distortion effects, is obtained by the following steps which are built into the computer program:

1. Calculate the individual load imposed on each pad from the prescribed load and the preload, by virtue of statics.
2. Calculate the thermally distorted film shape that results from the axial thermal gradients in the shaft and bearing pads, as well as the radial temperature gradient across the pads. These thermal gradients have to be obtained separately from a thermal map of the bearing region in which the heat flow through the rotor and bearings and the heat generation in the bearing film are included. (Temperature differences between the shaft and the bearing housing, produce a change in the bearing preload. This is separately calculated and the bearing performance calculations are conducted for the corrected value of preload).

3. Calculate the attitude angles, film thickness and pressure distributions for the loaded pads and the preload pads, in their thermally distorted shapes.

4. Calculate the change in pitch angle for a perturbed pitch moment to determine the resonant frequency of the gas film-pad in the pitch mode.

5. Calculate the change in roll angle for a perturbed roll moment to determine the resonant frequency of the gas film-pad in the roll-mode.

6. Calculate the change in radial displacement of the shaft for a perturbed bearing load to determine the total radial stiffness of the journal bearing.

7. Calculate the viscous loss for each pad and sum up to obtain the horsepower loss of the entire journal bearing.

The details of this analysis are included in Appendix B.

5.5 Performance Maps

A total of 11 cases were studied for the tilting-pad journal bearing. The condition for each case is listed in Table 1. Discussions of these cases are given in the following sections.

5.5.1 Reference Case

Figures 17 and 18 show the performance characteristics for a Reference case with which the other cases are compared. Two sets of curves are presented in these figures. The solid curves are for undistorted pads and the dotted curves are for thermally distorted surfaces. The thermal distortions are calculated by using the steady-state temperature distributions for the journal bearings in Figs. 10 and 11. It is seen that the distortions even for these fairly pronounced thermal gradients have very small influence upon the performance of the tilting pad bearing. This further confirms the conclusion in the screening analysis that the freedom of the pads to roll and pitch provides them with a very high tolerance to thermal distortions.

The pivot film thickness of the loaded as well as the preload pads increases

with the speed and gradually tapers off above 50,000 rpm due to the centrifugal growth of the shaft and the compressibility effect of the lubricant. For speeds greater than 20,000 rpm, the pivot film for the loaded pad is above 0.0005 inches. The radial film stiffness for the 4-pad configuration is symmetric in all directions and decreases with speed.

Both the trend and the magnitude of the power loss curve agree well with those calculated in Fig. II-4 of Ref. 2 for a four-pad bearing operating under comparable conditions.

In Fig. 18, the ratio of the resonant to the operating frequencies was plotted for the loaded as well as the preload pads both in the pitch and in the roll modes. The frequency ratio in the roll mode is shown to be always slightly higher than the pitch frequency ratio. At lower speeds, these resonant frequencies are all far above the running frequency. As the speed approaches 50,000 rpm, both the pitch and roll frequency ratios of the preload pads may have to be increased slightly in order to make this ratio greater than unity. The data for a higher preload will be presented later. On the other hand, it has been demonstrated both experimentally and analytically in Refs. 2 and 6 that the preload pads can operate near the pitch or roll resonant frequency without large amplitude oscillations because of the gas film damping, so that an increase in preload should not be necessary.

5.5.2 Effect of Ambient Pressure

Case B (Figs. 19 and 20) shows that when the ambient pressure is increased from 15 to 25 psia, the film thickness and the power loss improves slightly with the higher ambient, but all other performance curves remain essentially the same as the Reference case.

The influence of a reduction of ambient pressure from 15 to 5 psia as shown in the curves for Case C (Figs. 21 and 22) seems to be strong. Pivot film thicknesses are severely reduced, and the power losses are correspondingly increased, relative to the Reference case, at all speeds.

5.5.3 Effects of Bearing Load

Cases D and E (Figs. 23 through 26) give the performance for a 10 pound bearing load at ambient pressure equal to 15 and 25 psia. As expected, the frictional loss and the pivot film thickness are improved with the bearing load reduced by half. There is a slight reduction in the resonant frequency ratio for the lower loaded pads. The case of vertical operation or zero bearing load is plotted in Fig. 27.

5.5.4 Effect of Viscosity

Case G (Figs. 28 and 29) shows that the increase in viscosity from 6 to 8 x 10^{-9} $lb.sec/in^2$ introduces the expected change in performance. The film thickness for the loaded pads is higher and the friction horsepower also increases by about 30 percent, compared with the Reference case.

5.5.5 Effect of Clearance Ratio

In Case H (Figs. 30 and 31) the influence of reducing the machined-in clearance ratio is seen to be significant, particularly at higher speeds where the centrifugal growth is large. At 50,000 rpm, the pivot clearance reduces to about half that for the Reference case, and the power loss also is doubled for these small clearances. However, the resonant frequency ratio is much improved at high speeds for the preload pads.

The effect of increase in clearance ratio at a preload of 20 pounds instead of 12 pounds is shown in Case I (Figs. 32 and 33). This case should be compared with Case J (Figs. 34 and 35) instead of the Reference case because of the change in preload. As expected, the film thickness and power loss are improved with the larger machined in clearance ratio.

5.5.6 Effect of Preload

With a 12 pound preload, it was found that the pitch and roll resonanting frequencies of the preload pads are very close to the running frequency at speeds approaching 50,000 rpm. Case J shows the resonanting frequency ratios of these pads can be increased by more than 50 percent at 50,000 rpm if the preload is raised from 12 pounds to 20 pounds. However, the increase of preload also reduces the pivot film thickness of all pads, and this results

in approximately a 30 percent increase in power loss.

The performance under vertical operation with a preload of 20 pounds is shown in Fig. 36.

5.5.7 Effect of Thermal Distortion

In Case A, the performance of a thermally distorted tilting pad journal bearing was calculated and compared with the undistorted journal bearing. It was shown that the thermal distortions of an uncooled tilting pad bearing, in that case, did not have a significant influence on the performance.

It is now of interest to determine how the loaded pad will behave when more severely distorted. A study of the transient and steady-state temperature distribution reveals that thermal distortions come from two sources, the axial thermal gradient of the shaft (referred to as the coning temperature distribution) and the rise of shaft temperature at the center of the bearing (referred to as the crowning temperature distribution). Typical coning and crowning thermal conditions are shown in Fig. 37. The pivot and minimum film thickness plotted as Figs. 38 and 39 are for the operating conditions used for the Reference case at 50,000 rpm. From Fig. 38, it can be seen that both the pivot and the minimum film thickness are not much affected by the coning of the shaft even with an axial thermal gradient of 100 F/in. This result is not surprising since the pad is free to roll and the rolling compensates for the coning of the shaft.

The reduction of pivot and minimum film thicknesses due to crowning of the shaft, as seen in Fig. 39, is quite large. For a crowning temperature rise of 100° F, approximately 40 percent of the pivot and minimum film thicknesses are lost by shaft crowning.

The above results confirm the physically evident result that crowning of the shaft has a much stronger effect on bearing film thickness than does a coning type of distortion. The reason for this, as earlier noted, is that the bearing pads roll about their points of support to maintain alignment with the shaft when when it exhibits a linear coning type of distortion, but they cannot compensate as readily for a crowning type of distortion which involves a

curvature of the journal or bearing surfaces in the axial direction. Figures 37, 38 and 39 are useful in that they permit ready assessment of the effects of these two types of distortions on the bearing film thicknesses once the temperature gradients and, hence, the pad distortions can be estimated.

It should be noted that in the case of the bearings considered here, the maximum gradients or temperature differences calculated in the approximate thermal analysis given in Section 4 were as follows,

temperature gradient including coning: 50 F/inch

temperature differential inducing crowning: 40 F

The maximum temperature differential causing crowning was found in the case (Fig. 15) where the copper shunt thickness was reduced to 0.05 inches. Even at this condition, and without allowing for the fact that some crowning of the pads also occur which compensates in part for the shaft crowning, Fig. 39 shows that the loss of pivot point film thickness relative to an undistorted pad is only about 80μ inches, (i.e. $h_{pivot} = 0.69 \times 10^{-3}$ inches for the undistorted case and 0.61×10^{-3} inches for a 40 F crowning temperature rise).

The crowning temperature rise is due principally to the heat generated in the bearing film and it can be reduced in the shaft by use of the copper shunt in the journal region.

The above results, however, are encouraging in that they indicate the wide tolerance of tilting pad gas bearings to the presence of thermal gradients.

5.5.8 Gas Film Stability

In high speed rotating machinery, it is not uncommon to encounter rotor whirl. When the amplitudes associated with the whirl become large (comparable for example, to the magnitude of the minimum film thickness) so that the safety of the equipment is endangered, it becomes necessary to correct the conditions that give rise to the whirl. Basically, these comprise (a) identifying and eliminating or at least reducing the source of excitation or, (b) making design changes to control the whirl amplitude by providing additional damping.

In identifying the source of whirl excitation, it is necessary to differentiate between forced excitation and self excitation.

In the first case, the rotor is forced into whirl in response to excitation which is largely independent of the whirl amplitude. Examples are: rotor mass unbalance, unbalanced magnetic forces in electrical machinery and unbalanced pressure forces in aerodynamic components. Usually, this type of excitation associated with a clearly identifiable frequency (synchronous in the case of rotor unbalance, some multiple of the electrical frequency in electrical machinery, or some multiple of the number of struts, discharge ports or dissymmetry in the aerodynamic path in turbomachinery). The remedies are: to reduce the excitational force (better balancing, modifications in the magnetic field, "smoothing" the air passages, etc), to detune the system (i.e.by stiffening the rotor or changing the stiffness of the bearings) or provide sufficient damping to reduce the amplitude to acceptable limits.

In the case of self-excitation, the rotor axis does not have a stable equilibrium position. The rotor is in a condition where, once it gets away from the equilibrium position, due to any small disturbance, energy will be fed into the whirling of the rotor, and the amplitude will build up rapidly. This energy normally derives from the drive torque, but the source responsible for the self-excitation is, of course, the mechanism which is capable of converting "rotation energy" into "whirl energy". Since damping is commonly accepted as a "mechanism" which extracts energy from a vibration, whereas self-excitation, as just discussed, implies that energy is supplied to the vibration, one may say that the "mechanism" responsible for self-excited whirl behaves as a "negative damping". Thus, at the threshold of self-excitation, the overall system damping is zero, and the rotor will tend to whirl with a frequency equal to its lowest natural frequency, namely, the first critical speed, similarly to the response to an undamped resonance. This is typical of most forms of self-excited whirl, and it is one of the criteria used in identifying this type of excitation.

Thus, one obvious way of overcoming self-excited whirl is to provide sufficient additional damping to neutralize the amount of negative damping deriving from the source of the self-excitation. When this is not feasible, or can only be done to a limited extent, it is necessary to identify the source and find other corrective measures.

The most common "mechanism" of self-excited whirl is hydrodynamic instability, encountered in some fluid film bearings. Such bearings have "negative damping" for whirl frequencies less than approximately half of the rotational frequency which means that instability may be encountered at roughtly twice the first critical speed. Hence, high-speed rotors employ"anti-whirl" bearings of which the tilting pad journal bearing is a typical example. If the inertia of the pads and the friction of the pivots are ignored, this bearing is "inherently" stable and for this reason, this bearing type is the most commonly used one for high-speed rotors, especially in gas-lubricated machinery.

Recent investigations (e.g. Refs. 7 and 8) have shown that when the pad inertia is included in the analysis, the tilting pad gas-lubricated bearing has a finite stability threshold. This calculated stability threshold is, however, relatively high being of the order of 100,000 rpm for typical compact, space power Brayton cycle machines that have been run to date, such as the dynamic simulator of the axial flow turbocompressor described in Ref. 2. By making some assumptions regarding the friction restraint in bearing pivots or by otherwise imposing restraints on the pads, the calculated stability threshold can be reduced down to the order of 50,000 rpm or less. Experimentally, also, sub-synchronous whirl has been observed, e.g. in the axial flow turbocompressor simulator as described in Ref. 2, as well as in the radial flow gas generator developed elsewhere for the NASA. In both these cases, the whirl was effectively suppressed by reducing the operating clearance of the bearing, i.e. by increasing the level of preload.

At present, however, the state-of-the-art of stability analysis of tilting pad gas bearings is lagging the experimental observations and it has been useful principally in exploring possible causes of observed instabilities — after the instabilities are observed in particular machines. Accordingly, at this time, the stability threshold maps prepared from the experimental observations during development and operation of the axial flow turbocompressor simulator (and given in Figs. IV-15 to IV-17 of Ref.2) were used to establish the maximum operating bearing clearance at which stable operation is expected. Based on this data, which was obtained with a 2.125" diameter bearing and a rotor weight of approximately 11 lbs the maximum operating diametral clearance allowable without incurring sub-synchronous rotor whirl was 2.3 mils at speeds up to 50,000 rpm. This limit has been observed for the cases presented in the field maps.

6. DESIGN OF CONFORMABLE JOURNAL BEARING

For the conformable journal bearing, the three-foil journal bearing concept has been selected for the detailed analysis and design. This foil bearing is designed according to the same specifications as those given earlier (in Section 5.2) for the tilting pad journal bearing.

6.1 Bearing Dimensions

The major dimensions for the three-foil bearing described and analyzed herein were:

a. Shaft diameter: 2.00 inches
b. Length of foil: 2.00 inches
c. Number of foils: 3
d. Thickness of foil: 0.001 inch
e. Foil wrap angle: 60 degrees
f. One foil preloaded

6.2 Details of Foil Bearing Mechanical Design

The foil bearing design underwent several progressive changes before arriving at the configuration shown on Fig. 40. Initially, the approach was to utilize three separate foils each supported on a hammock-type sling support system. For high temperature operation, a design stress limit of 15,000 psi was selected for the mount support system to insure that long term creep could be maintained within design control. This, however, resulted in support wires of 3/16 inch diameter or greater which reduced the support system flexibility excessively. At lower temperatures, where stresses of 60,000 psi could be tolerated, the sling type mounting configuration appears to offer distinct advantages in alignment capability. At temperatures above 600 F, the flexibility of this support system diminishes and other methods of mounting the foil bearing become more attractive.

An important, practical design problem that became quickly apparent in the present design study (and which has in fact materialized in cases where foil bearings have been built and tested)is that of the end connections of the foil.

The end connections must be achieved without crimping the foil or otherwise causing it to deform or be non-uniformly stressed along its width. Partly to reduce the number of end connections, and also because of other design simplifications, a single strip is used to constitute all three pads. A somewhat similar arrangement was independently developed and is being used in another, more fundamental, analytical and experimental study of foil lubricated journal bearings conducted by another contractor for the NASA (Ref. 9).

In the single, continuous foil design concept that was considered here, and which is illustrated in Fig. 40, the foil is loosely threaded through the pins and a dummy shaft is installed and shimmed to establish the shaft center. The tension on the loosely installed foil is then increased to two pounds so that the foil securely contacts the shaft circumference. The two bottom foil segments are then locked in position to prevent further motion. Next, the preload of eight pounds is applied to the upper foil segment through the spring system. This insures that all the foil segments are maintained in tension, while permitting freedom for shaft radial and thermal growth. For small shaft diameter changes (up to .005 inches radially), an approximate 1 to 1 correspondence exists between radial dimensional shaft change and foil length change. This implies that the maximum change in foil length will not exceed plus or minus .002 inches due to centrifugal growth or to radial thermal gradients up to 500 F per inch. Utilizing a foil tension preload spring of 500 pounds per inch spring rate, results in a maximum possible change in tension of plus or minus one pound.

The complete bearing assembly is mounted on a gimbal configuration consisting of two sets of flexural pivots. The pivotal restraint of these flexures is 22 inch pounds per radian, which is very small in comparison with the angular stiffness of the bearing. The bearings, therefore, should be quite capable of maintaining alignment under thermal gradient conditions. The maximum load capabilities of the flexures is above 300 pounds which is approximately an order of magnitude greater than the required capacity.

The foil itself has a tensile stress of approximately 4800 psi which represents the highest stress element in the design. Above 1000 F, the foil may be subject to long term creep. The preload spring can accommodate some change in foil length and consequently some creep may be tolerated. Because of the limited

material data at elevated temperature, it is impossible to predict life accurately. However, the design should be suitable for a life in excess of 1000 hours at elevated temperature, in excess of 1000 F, and considerably longer life at temperature below 1000 F.

Starting and stopping operation on the foil is presently a problem because of the poor compatibility of suitable foil materials, such as Inconel X and the shaft materials. The application of coatings to improve compatibility, as used in rigid surface bearings would greatly reduce the foil flexibility. Therefore, hydrostatic jacking is utilized, supplying the jacking gas through the center of the shaft. A single set of orifice holes located centrally under the foil width is utilized. As soon as a self-generated film is produced during operation, the jacking gas may be shut off.

6.3 Multi-Pad, Foil Journal Bearing Analysis

In a recent independent, experimental study of elastohydrodynamic lubrication of individual foil bearings (Ref. 10), very good agreement was obtained between the measured and predicted film thickness distributions. This enhances the confidence in using existing foil bearing theory, which is given in Refs. 11 and 12. To calculate the performance of the present three-foil journal bearing, the theory of Ref. 11, for an infinitely long foil including the compressibility effects, has been adopted. Using the results in Ref. 13, an analysis and computer program were prepared to determine the minimum film thickness, the radial stiffness and the power loss of multi-pad bearing. In this analysis, the effects of the thermal differential between the mounting and the journal, and the effects of the foil elasticity on the radial stiffness were all included. The foil bearing analysis used here is for a three "pad" bearing with two pads fixed.

Briefly, the analysis involves first calculating the radial load exerted upon each pad from the prescribed preload and the load applied on the journal bearing. With the load upon each pad given, a set of equations is then derived to solve for the foil tension, the wrapping angle, the nominal gas film thickness, and the displacement of the shaft. These equations are derived from the geometry of the system, from the elongation of the foil due to stretching and thermal expansion, and from the infinitely long, flexible foil theory of Ref. 11.

A slight non-linearity in these equations necessitates the use of a iterative procedure to solve for the above quantities. However, the convergence of these equations is extremely rapid. The stiffness expressions in any two mutually orthogonal direction are then derived analytically by a small perturbation of load in these directions. The derivation of the analysis is included in Appendix C.

6.4 Performance Maps

Altogether 10 cases have been studied for the three-pad foil journal bearing. The operating conditions used for each case and the major results obtained from the computer program are listed in Table 2. The performance maps for these cases are plotted on Figs. 41 to 52. These performance curves include the minimum film thickness of the loaded as well as the preload foil segments, the power loss, and the radial stiffness of the journal.

6.4.1 Effect of Ambient Pressure

Cases A, B and C show the effect of the ambient pressure at a preload of 8 pounds and a bearing load of 20 pounds. At 50,000 rpm, the minimum film thickness for the loaded foil is very small, in the order of 0.2 mils and less, and the minimum film for the preloaded upper foil is in the neighborhood of half a mil. The nominal film is about 1.4 times the minimum film. Because of these small film thicknesses, the power losses are shown to be very high. At 5 psia ambient the power loss becomes 0.6 hp which is more than twice of that of the tilting pad bearing. The stiffnesses in two mutually perpendicular directions are unequal because of the preloaded three-foil configuration. The stiffnesses, as shown in Figs. 41 to 43, are insensitive to the change of ambient pressure.

6.4.2 Effect of Load

As the load decreases from 20 pounds to 10 pounds, the minumum film thickness for the loaded foil is almost doubled as indicated in Figs. 44 to 46. The decrease in load brings considerable reduction in stiffnesses. On the other hand, the power loss is much improved.

The case of zero-gravity operation is plotted in Figs. 47 to 49 for p_a = 5 to 25 psia. For these cases, all foils have the same film thickness, and power loss is the least of all cases, however, the unloaded foil bearing has a very low stiffness.

6.4.3 Effect of Viscosity

Case J, Fig. 50, was conducted for the same conditions as Case B, Fig. 42, except that the viscosity was increased to 8×10^{-7} lbsec/in^2. As would be expected, the higher viscosity provides some additional film thickness for the loaded foil pads, as well as a higher power loss for the bearing.

6.4.4 Effect of Thermal Differential Between Housing and Shaft

Cases K and L are concerned with the effects of the temperature difference between the foil and the shaft. As shown in Figs. 51 and 52, a change of 600 F in the thermal differential brings negligible change in the performance of the foil bearing. However, large thermal differential does have a strong influence on the shaft displacement.

6.5 Conclusions of the Foil Journal Bearing Performance Analysis

The foregoing results lead to the following conclusions:

a. Because they are conformable, foil bearings possess an inherent advantage in tolerating the shaft thermal coning and crowning. This, however, is obtained at some cost in increased power loss. For example, the power loss of the three-foil bearing may be as high as twice of that of the tilting pad journal bearing under the same operating conditions, when high radial stiffness is necessary to prevent sizeable excusions of the shaft center.

b. Compressibility effects are important in the foil bearing, the clearance of the loaded foil causing a reduction in the minimum film thickness.

c. The thermal differential has a strong influence on the displacement of the shaft center but has negligible influence on the film thickness.

7. HIGH TEMPERATURE THRUST BEARING

The helical grooved thrust bearing was selected for the detailed analysis in the present study, based on the results of the screening analysis which is described in detail in Ref. 1, and summarized in Section 2 of this report. The load capacity of the helical grooved bearing is nearly independent of gas compressibility effects up to very high values of the compressibility parameter Λ. Thus, over a substantial part of the operating range specified for this study, the helical grooved bearing was found to have higher load capacity than the other gas-lubricated thrust bearing types considered, such as the tilting pad thrust bearing. As with other thrust bearing types, that comprise a full annular ring, the load capacity of the helical grooved bearing does, however, suffer significant loss of load capacity when the thrust plate or collar distort, as in the presence of thermal gradients. Thus, in the present study where we are concerned with thrust bearings that are capable of operating at elevated temperatures without cooling, the principal emphasis was on the effects of thermal distortions and how these can be minimized. The design specifications for the study were the same as those given for the journal bearings in Section 5.2 of this report. The design was made for a double acting thrust bearing, capable of operation under axial loads in either direction.

7.1 Thrust Bearing Dimensions

The major dimensions of the thrust bearing and the spiral groove geometry used in the analysis and computations given in this section are as follows:

a. Outside diameter: 4.00 inches
b. Inside diameter: 2.25 inches
c. Groove arrangement: for inward pumping
d. Number of grooves: 25
e. Groove depth: .00225
f. Groove width to land width ratio: 2
g. Groove terminating radius: 2.77 inches
h. Spiral angle: 73^{o}

7.2 Mechanical Design of the Bearing

The double acting, spiral groove thrust bearing arrangement is illustrated in Figs. 53(a) and (b). A double acting bearing is used to permit load capacity in either direction of loading. The use of a double acting bearing with relatively small axial end play (of the order of 0.004", as used here), also provides a higher and more nearly uniform axial stiffness, as well as serving to accurately position the rotor in the axial direction. Furthermore, as discussed in the thrust bearing analysis provided later in this section, it also serves to reduce thermal distortions of the thrust collar.

To provide freedom for self alignment, the thrust plates assembly is mounted in a gimbal flexure. The flexures, fabricated from Rene 41, are subjected to torsion to provide the required gimbal motion with a restraining moment of 44 inch - lbs per radian. This is about two orders of magnitude smaller than the angular stiffness of the fluid film and therefore allow the thrust bearing faces to align accurately with the thrust collar. Under angular motions of the order of 0.003 radians, the flexures approach an infinite fatigue life. The use of the flexures limits the axial load capacity of the thrust support structure to a 400 lb. capability. This, however, is well above the thrust bearing load requirement. The flexure units also serve to thermally isolate (from the standpoint of heat conduction) the thrust stator assembly from the housing, thus allowing it to track more accurately the rotor temperature.

The growth of the bore of the Rene 41 thrust runner at 50,000 rpm and assuming a temperature of 1000 F is 0.0052 inches diametrally. To facilitate assembly and disassembly and to limit the bore compressive stress required, the thrust runner is assembled with a diametral interferenceof 0.004 to 0.0045 inches on an intermediate spring member which is, in turn, assembled with a 0.001 to 0.002 inches diametral interference to the shaft. Squareness of the assembly is maintained by the shoulder on the shaft. Anti-rotation pins are added to insure against rotation of the thrust runner, relative to the shaft. At 50,000 rpm and 1000 F temperature, the maximum tangential stress in the runner bore is 72,800 psi. This corresponds to a minimum life of 10,000 hours with less than 0.2% creep. The interference between the spring mount and the thrust runner assembly accommodates this creep.

As indicated above, the thrust runner is fabricated from Rene 41 material. This is to take advantage of the high strength of this alloy at elevated temperatures. The stationary thrust plates are fabricated from TZM in order to take advantage of the low thermal expansion coefficient (α) and high thermal conductivity (k) of this alloy, as well as of its good high temperature properties (in an inert gas environment). As is shown later in the analysis part of this section, the value of $(\frac{\alpha}{k})$ determines the thermal distortion of the bearing parts. With the low value of (α/k) of TZM, thermal distortions of the thrust stator are extremely small, so that only the thermal distortions of the Rene 41 thrust collar need be considered from the standpoint of their effect on the bearing load capacity. The present design calls for a TZM spacer ring between the thrust bearing faces. Since the total bearing clearance (axial end play) at design temperature will depend on the differential thermal growths between the Rene 41 thrust collar and the TZM spacer ring, allowance for this differential thermal expansion has to be made at assembly. For a bearing operating temperature 1000 F above the assembly temperature, and assuming a 0.5 inches thick thrust collar, the loss in axial clearance is 0.0025 inches. The axial clearance at the assembly temperature thus has to be 0.0065 inches, to achieve the desired clearance of 0.004 inches at an operating temperature which is 1000 F above the assembly temperature.

7.3 Thrust Bearing Analysis

The analysis of helical grooved, gas-lubricated thrust bearing is well established and is described, for example in Refs. 14 and 15. Using the analysis of Ref. 15, the normalized load capacity for the bearing having the geometrical properties defined above (in section 7.1) was calculated and is given in Fig. 54. This figure, however, neglects the loss of load capacity that occurs in event of thermal distortion of the plates. Recently, the analysis of helical grooved thrust bearings was extended to include the effects of thermally induced distortions of the bearing surfaces (Ref. 16).

This theory, adapted to the double acting thrust bearing of interest here is briefly reviewed below. This analysis was used to obtain the bearing performance charts provided later in this section.

7.3.1 Analysis of Thermally Distorted, Spiral-Grooved Thrust Bearing

The analysis is based on the well known relation governing the spherical curvature produced by a given heat flux in the axial direction. As illustrated in the sketch below, the curvature produced when a disk is heated from one side by a uniform heat flux q" (heat generated per unit area), is given by:

$$\frac{1}{R} = \alpha \left(\frac{\partial T}{\partial z} \right) = \frac{\alpha}{k} q'' \qquad (1)$$

where α is the coefficient of thermal expansion and k is the thermal conductivity.

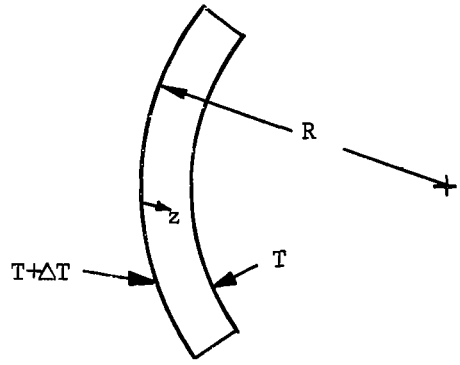

Thermal Distortion of a Thrust Plate

In a thrust bearing, the heat flux will not be uniform, but is proportional to $(\omega^2 r^2)/h$. However, the curvature produced by this non-uniform heating can be approximated by using Eq. (1) if one assumes that the heat flux q" is the average flux over the bearing area. Based on this assumption,

$$q'' = f \left[\frac{2 \pi \mu \omega^2}{J \pi (r_o^2 - r_i^2)} \int_{r_i}^{r_o} \frac{r^3 \, dr}{h_o + \frac{r^2}{2R}} \right] \tag{2}$$

where f is a friction factor to account for reduction of friction due to the larger film thickness in the grooves. f is determined by the spiral groove bearing analysis. Carrying out the integration and substituting the results in Eq. (1) a relation can be found between the dimensionless curvature K and the distortion parameter Δ.

$$K^2 \Delta = \left[\frac{1}{1 - \left(\frac{r_i}{r_o}\right)^2} \right] \ell_n \left[\frac{1 + K}{1 + \left(\frac{r_i}{r_o}\right)^2 K} \right] \tag{3}$$

where

$$\Delta = \left(\frac{2}{\mu \omega^2 r_o^2} \right) \left(\frac{k}{\alpha}\right) \left(\frac{h_o}{r_o}\right) \frac{1}{f}$$

$$K = \frac{r_o^2}{2 h_o R}$$

It is important to note that, physically, the factor K represents the ratio of the amount of non-flatness at the bearing rim(i.e. the crown height $r_o^2/2R$) to the minimum film thickness, h_o. Once the geometry, velocity, h_o, and the thermal properties are known, the distortion parameter can be readily calculated, and the crown height can be found by using Eq. (3).

In the case where distortion of the runner and stator are both considered, Eq. (3) can still be used if the α/k in the distortion parameter is taken as

$$\frac{\alpha}{k} = \frac{1}{q''}\left[\frac{\alpha_1 q_1''}{k_1} + \frac{\alpha_2 q_2''}{k_2}\right] \tag{4}$$

To determine the load capacity of a distorted spiral-grooved thrust bearing, the numerical solution of the spiral groove bearing equation is extended to a radially varied film thickness. This numerical program was used to generate the performance maps of the present double-acting thrust bearings.

7.3.2 Analysis of Double Acting Thrust Bearing

For the double acting thrust bearing shown in Fig. 53(a), the reduction of load due to thermal distortion is not as severe as that of the simple thrust bearing because the heat is generated on both sides of the runner and the axial thermal gradient of the runner is smaller than the single thrust configuration. The analysis of this bearing uses the analysis of Ref. 16, but with some modification as described below.

In the double acting thrust bearing, the load and pressure will be affected by thermal distortions of three types. The first type is due to the axial thermal gradient of the stator. This type of thermal distortion is minimized by the use of the molybdenum alloy TZM, for the stator. As was shown in the screening report (Ref. 1), the use of TZM gives very small thermal distortions for a single thrust plate running at 50,000 rpm with a diameter larger than that considered in the present design. The present stator has two stator faces bolted together with a spacer. This construction introduces additional restraint to thermal distortion. Thus, the thermal distortion for the present double acting stator made of TZM will have a negligible influence on the bearing performance and it is ignored in the analysis.

The second type of thermal distortion is produced by the axial thermal gradient in the runner. This distortion is significant for two reasons: (1) most of the heat generated in both sides of the thrust face will be conducted through the runner, (2) and low α/k type of material such as TZM can not be easily used for the runner because of strength limitations. This type of thermal distortion is accounted for in the analysis.

The third type of thermal distortion is due to the radial thermal gradient in the runner. As was shown earlier, in the transient and steady-state temperature distribution given in section 4 of this report, the temperature at the outside diameter of the runner is higher than that at the inside diameter. The expansion at the outside diameter causes a dishing effect which opposes the thermal crowning produced by the axial thermal gradient at the loaded face. This compensating effect is included in the calculations.

To determine the thermal crowning of the runner due to the axial thermal gradient, one considers that the crowned spherical curvature is related to the average axial thermal gradient by

$$\frac{1}{R} = \alpha \left(\frac{\partial T}{\partial z}\right)_{ave.} \tag{5}$$

To relate the axial thermal gradient and the heat generation in the gas film for the double acting thrust runner, the following heat balance is performed.

The sketch below show that the axial temperature distribution is represented by

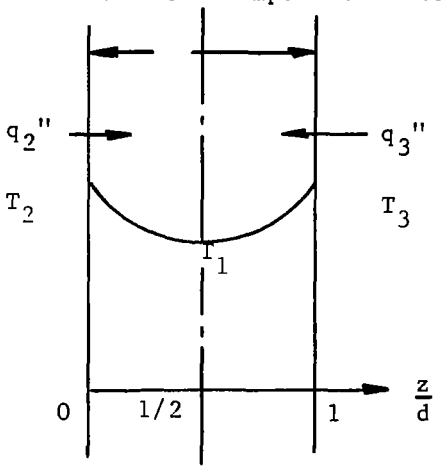

a parabola governed by the temperature at the two surfaces, T_2 and T_3, and the center temperature, T_1. This parabola can be expressed as:

$$T = T_2 + (4T_1 - 3T_2 - T_3)\left(\frac{z}{d}\right) + (-4T_1 + 2T_2 + 2T_3)\left(\frac{z}{d}\right)^2 \tag{6.}$$

The average gradient is:

$$\left(\frac{\partial T}{\partial z}\right)_{ave.} = \left(\frac{T_3 - T_2}{d}\right) \tag{7}$$

and

$$q''_2 = - k \left.\frac{\partial T}{\partial z}\right|_{z=0} = - k \left(\frac{4T_1 - 3T_2 - T_3}{d}\right) \tag{8}$$

$$q''_3 = k \left.\frac{\partial T}{\partial z}\right|_{z=d} = k \left(\frac{-4T_1 + T_2 + 3T_3}{d}\right) \tag{9}$$

Substracting Eq. (8) from Eq. (9), one obtains

$$\frac{2k}{d} (T_3 - T_2) = q''_3 - q''_2 \tag{10}$$

or

$$\left(\frac{\partial T}{\partial z}\right)_{ave.} = \frac{1}{k} \left(\frac{q''_3 - q''_2}{2}\right) \tag{11}$$

To obtain the relation between the curvature and the heat fluxes, Eq. (11) can be substituted into Eq. (5) to give

$$\frac{1}{R} = \frac{\alpha}{k} \phi q''_3 \tag{12}$$

where $$\phi = \frac{1}{2} \left(1 - \frac{q''_2}{q''_3}\right)$$

Eq. (12) shows that for a double acting thrust bearing, the curvature now depends upon the ratio of the heat flux at the two faces of the bearing. Note for $q''_2 = q''_3$, that is when the runner is at the middle position, the factor ϕ vanishes and there will be no distortion. Now if the heat flow is purely axial, then $q''_2 = - q''_3$ and the factor ϕ becomes unity. This is precisely the case of a single face thrust bearing with a purely axial heat flow.

Eq. (12) also justifies the use of the Ref. 16 analysis for the double acting thrust runner if the distortion parameter is redefined by

$$\Delta = \left(\frac{2}{\mu\,\omega^2\,r_o^2}\right)\left(\frac{k}{\alpha}\right)\left(\frac{h_o}{r_o}\right)^2\frac{1}{f\phi}$$

For the present design, the nominal operating film thickness is 0.001 inches at the loaded face and 0.003 inches at the reverse side making a total bearing gap of 0.004" at the operating condition. Assuming the heat flux is proportional to the inverse of the film thickness, the value of ϕ may be calculated by

$$\phi = \frac{1}{2}\left(1 - \frac{h_o}{.004 - h_o}\right)$$

where h_o is the center film thickness of the loaded thrust bearing. Note ϕ is 1/3 for h_o = 0.001 inches.

Figure 55 plots the curvature K against the distortion parameter Δ. Once the quantities contained in the distortion parameter are known, the crown height can be readily calculated from this figure.

Figures 56 and 57 plot the load degradation (i.e. the ratio of the thermally distorted load capacity to the undistorted load capacity) against the curvature K for two ambient pressure and for various values of h_o/r_o. Comparing these two figures, it is seen that the load degradation is not sensitive to the change of the ambient pressure. The corresponding friction factor which is defined as the actual frictional power loss divided by the Couette power loss, is plotted on Figs. 58 and 59. These data will be used to calculate the performance maps of the thermally distorted thrust bearing.

7.4. Sample Calculation

The sample calculation is for the following geometry and operation conditions.

r_o	=	outside radius	2 inches
r_i	=	inside radius	1.125 inches
P_a	=	ambient pressure	15 psia
α	=	coefficient of thermal expansion (Rene 41)	$8.5 \times 10^{-6} \frac{\text{in.}}{\text{in.}} \frac{1}{^{o}\text{F.}}$
k	=	thermal conductivity (Rene 41)	14.5 B/ft-hr-^{o}F.
h_o	=	center film thickness of the loaded face	0.001 inches
N	=	speed	50,000 rom
μ	=	viscosity	6×10^{-9} lb-sec/in.^{2}

1. Undistorted Load Capacity of the Loaded Thrust Face

For the loaded thrust face, the film thickness to groove depth ratio is

$$\left(\frac{h_o}{\delta}\right)_3 = \frac{0.001}{0.00225} = 0.445$$

where the subscript 3 refers to the loaded thrust face.

From Fig. 54:

$$\left(\frac{\overline{W}}{\frac{}{\Lambda}}\right)_3 = 0.024$$

Thus, the load capacity of the loaded thrust face is

$$(W_o)_3 = 0.024 \times \pi(r_o^2 - r_i^2) \times \frac{3\mu\omega(r_o^2 - r_i^2)}{h_o^2}$$

$$= 0.024 \times 3\pi (2^2 - 1.125^2)^2 \times 5230 \frac{6 \times 10^{-9}}{10^{-6}}$$

$$= 53.4 \text{ lb}$$

2. Undistorted Load Capacity of the Reverse Thrust Face

For the reverse thrust face, the film thickness to groove depth ratio is

$$\left(\frac{h_o}{\delta}\right)_2 = \frac{0.003}{0.00225} = 1.33$$

where the subscript 2 refers to the reverse thrust face. From Fig. 54

$$\left(\frac{\bar{W}_o}{\Lambda}\right)_2 = 0.0088$$

The load capacity for the reverse thrust is

$$(W_o)_2 = 0.0088 \times 3\pi (2^2 - 1.125^2)^2 \times 5230 \times \frac{6 \times 10^{-9}}{9 \times 10^{-6}}$$

$$= 2.18 \text{ lb.}$$

3. Total Undistorted Load Capacity

The total load capacity for the undistorted double acting thrust bearing is

$$(W_o)_T = (\bar{W}_o)_3 - (\bar{W}_o)_2 = 53.4 - 2.18$$
$$= 51.6 \text{ lb.}$$

4. Thermally Distorted Load Capacity for the Loaded Thrust Face

a, Estimate the dimensionless friction factor, f from Fig. 58 .

$f \approx 0.81$ for $\frac{h_o}{r_o} = .0005$ and no distortion

b, Calculate the factor ϕ

$$\phi \cong \frac{1}{2}\left[1 - \frac{h_o}{h_T - h_o}\right]$$

For $h_T = 0.0004$ and $h_o = 0.001$, $\phi = \frac{1}{3}$

c, Determine the distortion parameter

$$\Delta = \frac{2}{\mu\ (\omega r_o)^2} \left(\frac{k}{\alpha}\right) \left(\frac{h_o}{r_o}\right)^2 \frac{1}{f\phi}$$

For $f = 0.81$

$\phi = 1/3$

$\omega = 5230$ rad/sec.

$r_o = 2.0$ in.

$\mu = 6 \times 10^{-9}$ lb/in.^{2} sec.

$k = 14.5$ B/ft. hr.$^\circ$F

$\alpha = 8.5 \times 10^{-6}$ in/in. $^\circ$F

$$\frac{h_o}{r_o} = 0.0005$$

$$\Delta = \frac{2 \times 778}{6 \times 10^{-9} \times (5230 \times 2)^2} \left(\frac{14.5}{3600 \times 8.5 \times 10^{-6}}\right) \times (0.0005)^2 \times \frac{3}{0.81}$$

$$= 1.04$$

d, Determine the dimensionless curvature K from Fig. 55.

For $\frac{h_o}{r_o} = 0.005$ and $\Delta = 1.04$,

$K = 0.46$

e, Determine the thermal dishing due to the radial thermal gradient

For the double acting thrust runner, the outside radius is hotter than the inside radius causing the runner to dish. The amount of dishing is calculated by

$$(\Delta h)_{dishing} = -\frac{\alpha d}{2} \left[(T)\ r = r_o - (T)\ r = r_i\right]$$

For the present case

$(T)\ r = r_o - (T)\ r = r_i = 135$ F (see Fig. 13)

$d = 1/2$, hence

$$(\Delta h)_{dishing} = -\frac{8.5 \times 10^{-6} \times 0.5}{2} \times 135 = -0.000287$$

The effective curvature produced by dishing is

$$\left(\frac{r_o^2}{2R}\right)_{dishing} = \frac{-.000287}{1 - \left(\frac{r_i}{r_o}\right)^2} = \frac{-.000287}{1 - \left(\frac{1.125}{2}\right)^2}$$

$$= -0.000416$$

f. Correct the dimensionless curvature K for the dishing.

$$K_{corrected} = 0.46 - \left(\frac{r_o^2}{2R}\right)_{dishing} \frac{1}{h_o}$$

$$= 0.46 - 0.416 = 0.044$$

It is seen that for the loaded thrust face, the crowning caused by the axial thermal gradient is almost completely compensated by the thermal dishing due to the radial thermal gradient.

g. Determine the load degradation. The load reduction can be obtained from Fig. 56 .

For $\frac{h_o}{r_o} = 0.0005$ and $K = 0.044$

$$\left(\frac{\overline{W}}{\overline{W}_o}\right)_3 = 0.925$$

$$W_3 = (W_o)_3 \times 0.925 = 53.4 \times .925 = 49.5 \text{ lb.}$$

5. Thermally Distorted Capacity of the Reverse Thrust Face

For the reverse thrust face, both the axial and radial thermal gradients cause the runner face to dish. These two effects are additives both contributing to reduction of the load capacity.

Since the load contributed by the reverse thrust face is small, we may assume that the thermally distorted load capacity is equivalent to the undistorted load capacity evaluated at the mean film thickness. For the present case, the mean film is

$$h_{mean} = 0.003" - \frac{0.000602}{2}$$

$$= 0.0027"$$

The value of $\frac{h}{\delta}$ for $h_{mean} = 0.0027"$ is

$$\frac{h}{\delta} = \frac{0.0027}{0.00225} = 1.2$$

Figure 54 gives

$$\left(\frac{\bar{W}}{\Lambda}\right)_2 = 0.0102$$

Hence

$$(W)_2 = 0.0102 \times 3\pi (2^2 - 1.125^2) \times 5230 \times \frac{6 \times 10^{-9}}{(2.7)^2 \times 10^{-6}}$$

$$= 3.1 \text{ lb.}$$

6. Thermally Distorted Total Load Capacity

The total load capacity for the thermally distorted double acting thrust bearing is

$$(W)_T = (\bar{W})_3 - (\bar{W})_2 = 49.5 - 3.1$$

$$= 46.4 \text{ lb.}$$

7.5 Discussion of Performance Maps

Figures 60 to 62 plot the total thrust load of the double acting thrust plate against the minimum film of the loaded thrust face, h_{min}. At h_{min} = 0.002 inches, the thrust runner is at its mid-position corresponding to the zero load condition.

As was discussed earlier, the load capacity is affected by the crowning due to the axial thermal gradient, as well as by the dishing due to the radial thermal gradient. The lower curve in Fig. 60 shows that considerable load carrying capacity is lost when the effect of crowning due to the axial thermal gradient is included. Now, if the effect of the radial thermal gradient in the runner is also included, this load capacity is largely recovered. The load capacity considering both the crowning and dishing effects is indicated by the middle curve in Fig 60. The degree of load compensation by the dishing effect can be controlled by the thickness of the thrust runner.

It should be noted, however, that an overcompensation will result in loss of load capacity due to dishing instead of crowning. Similar trends were also found on the effects of thermal distortion on load carrying capacity at 30,000 and 10,000 rpm and they are plotted on Figs. 61 and 62.

The static axial stiffness obtained by graphical differentiation of the load curves are shown in Figs. 63 to 65 for speeds at 50,000, 30,000 and 10,000 rpm. The corresponding power losses, as calculated by the procedure indicated in the sample calculation, are plotted in Figs. 66 and 67.

Although the performance maps given in this section are for an ambient pressure of 15 psia, they are equally applicable to other ambient pressures in the range of 5 to 25 psia since, as shown in Figs. 54, 56 and 57, the load capacity and the load capacity degradation due to thermal distortions are not influenced by the ambient pressure, within the operating range of interest here.

For viscosities other than 6×10^{-9} lb-sec/in.^{2}, the load, stiffness, and power loss can be calculated from these curves by assuming that they are directly proportional to the viscosity.

7.6 Conclusions of the Thrust Bearing Analysis

a. The minimum film thickness of a double-acting spiral-groove thrust bearing is strongly affected by thermal distortions from two origins:

   1. The axial thermal gradient resulting from the difference between heat generated at the loaded and the reverse thrust faces; and
   2. The radial thermal gradient resulting from the radially inward heat flow.

   At the loaded thrust face, the axial thermal gradient causes a crowning which reduces the gas film thickness, but this reduction is compensated by the dishing resulted from the difference in the axial growth due to the radial thermal gradient.

   By designing the thickness of the thrust runner at 0.5 inch for the case considered here, it was found that the loss of gas film due to the crowning is largely recovered by the dishing action due to the radial thermal gradient over the 10,000 to 50,000 rpm speed range.

   At 50,000 rpm and 0.001" film thickness, the undistorted spiral groove theory predicts a total thrust load of 52 lb. If the crowning due to the axial thermal gradient is considered alone, the load decreases from 52 lb to 30 lb for a minimum film thickness of 0.001 inch. With the compensation from the dishing due to the radial temperature gradient, the load climbs back to 47 lb which is only a slight reduction from the undistorted load capacity.

b. From the standpoint of power loss, the thermal distortion produces some reduction in power loss. In all cases considered, it was found that there was a slight reduction in frictional horsepower loss when the thermal crowning was considered under the same load.

TABLE 1

INPUT DATA FOR TILTING PAD JOURNAL BEARING RUNS

Case Designation	Load lbs	Preload lbs	$C/Rx10^3$ inches	P_a psia	μ Reyns	$\frac{L}{D}$	$\frac{t}{D}$
A	20.0	12.0	2.5	15.0	6.0	1.0	0.05
B	20.0	12.0	2.5	25.0	6.0	1.0	0.05
C	20.0	12.0	2.5	5.0	6.0	1.0	0.05
D	10.0	12.0	2.5	15.0	6.0	1.0	0.05
E	10.0	12.0	2.5	25.0	6.0	1.0	0.05
F	0	12.0	2.5	15.0	6.0	1.0	0.05
G	20	12.0	2.5	15.0	8.0	1.0	0.05
H	20.0	12.0	1.5	15.0	6.0	1.0	0.05
I	20.0	20.0	3.5	15.0	6.0	1.0	0.05
J	20.0	20.0	2.5	15.0	6.0	1.0	0.05
K	0	20.0	2.5	15.0	6.0	1.0	0.05

TABLE 2

INPUT DATA FOR FOIL JOURNAL BEARING RUNS

Case	Load lbs	Preload lbs	P_a	μ Reyns	$\frac{L}{D}$	Foil Thickness inch	$T_{housing} - T_{shaft}$ °F
A	20.0	8.0	5.0	6.0	1.0	0.001	200.0
B	20.0	8.0	15.0	6.0	1.0	0.001	200.0
C	20.0	8.0	25.0	6.0	1.0	0.001	200.0
D	10.0	8.0	5.0	6.0	1.0	0.001	200.0
E	10.0	8.0	15.0	6.0	1.0	0.001	200.0
F	10.0	8.0	25.0	6.0	1.0	0.001	200.0
G	0	8.0	5.0	6.0	1.0	0.001	200.0
H	0	8.0	15.0	6.0	1.0	0.001	200.0
I	0	8.0	25.0	6.0	1.0	0.001	200.0
J	20.0	8.0	15.0	8.0	1.0	0.001	200.0

APPENDIX A

Transient Thermal Analysis of a Simplfied Rotor-Bearing System

NOMENCLATURE FOR APPENDIX A

c	heat capacity, BTU/lb-^{o}F
h_1, h_3	film thickness, inches
h_α, h_β	film coefficient, BTU/in^{2}xsecx^{o}F
k	conductivity, BTU/inxsecx^{o}F
q	heat flux, BTU/sec
r_1, r_2	shaft inner and outer radii, inches
r_3	bearing outside radius, inches
r,x	coordinates, inches
t_1	thickness, inches
$T_1, T_2, T_\alpha, T_\beta$	temperature, ^{o}F
U	tangential velocity, in/sec
ρ	density, lbs/in^3
τ	time, seconds
μ	viscosity, lbsec/in^2
ω	angular velocity, radians/second

Superscripts and Subscripts (A,B,C,D,E,F,G) denote the rotor sections as defined in Figure 8(a).

A. Governing Equations

Figure 8 (a) shows that the simplified rotor-bearing configuration may be divided into a number of sections. In Sections A and G, the heat flow is assumed to be one-dimensional in the radial direction. At each grid point, accounts are made for the heat convected at both faces of the disk. In Sections B, D and F, the heat flow is assumed to be one-dimensional in the axial direction. Again, the heat convection on both sides of the cylindrical surfaces are accounted at each grid point. In Sections C and E, the one-dimesional axial heatflow is considered for the shaft as well as for the bearing sleeve. The heat flow between the shaft and bearing sleeves is by conduction through the gas film. In Section H, the radial heta flow is assumed for the thrust runner and the two thrust stators on each side of the runner. The convective boundaries are considered at the oustide face of the stator.

The governing equations for each successive section are derived below.

Section A

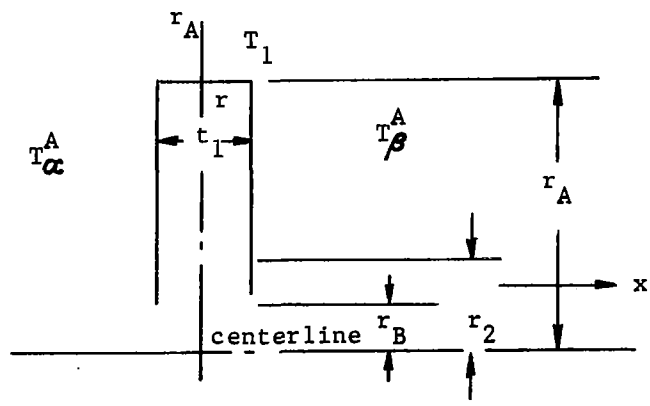

The equation governing the radial heat transfer for the Section A is

$$\frac{\partial T_1}{\partial \tau} = \left(\frac{k_1}{\rho_1 c_1}\right)^A \frac{1}{r}\frac{\partial}{\partial r}\left(r\frac{\partial T_1}{\partial r}\right) - \left(\frac{h_\alpha}{\rho_1 c_1 t_1}\right)^A (T_1 - T^A_\alpha) - \left(\frac{h_\beta}{\rho_1 c_1 t_1}\right)^A \left(T_1 - T_\beta\right)^A \quad (1)$$

The boundary conditions at $r = r_A$ is

$$- k_1^A \frac{\partial T}{\partial r} = h_\alpha^A (T_1 - T_\alpha^A) \tag{2}$$

at $r = r_B$,

$$k_1^A \frac{\partial T}{\partial r} = h_\alpha^A (T_1 - T_\alpha^A) - k_1^B \frac{(r_2+r_B)(r_2-r_B)}{2r_B \; t_1^A} \frac{\partial T}{\partial x} \tag{3}$$

Section B

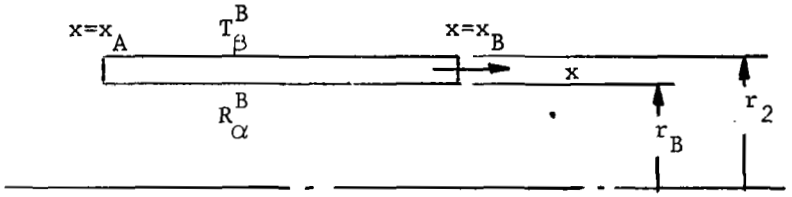

The heat conduction equation governing the interior points is

$$\frac{\partial T_1}{\partial \tau} = \left(\frac{k_1}{\rho_1 c_1}\right)^B \frac{\partial^2 T}{\partial x^2} - \left(\frac{h_\alpha}{\rho_1 c_1 t_1}\right)^B \frac{r_B}{r_m} (T_1 - T_\alpha^B) - \left(\frac{h_\beta}{\rho_1 c_1 t_1}\right)^B \frac{r_2}{r_m^B} (T_1 - T_\beta^B) \tag{4}$$

where $r_m^B = (r_2 + r_B) \times 0.5$

Boundary conditions for Section B.

At $x = x_A$, the boundary condition is the same as that for Section A at $r = r_B$.

At $x = x_B$, the boundary condition is the same as that at $x = x_B$ for Section C.

Section C

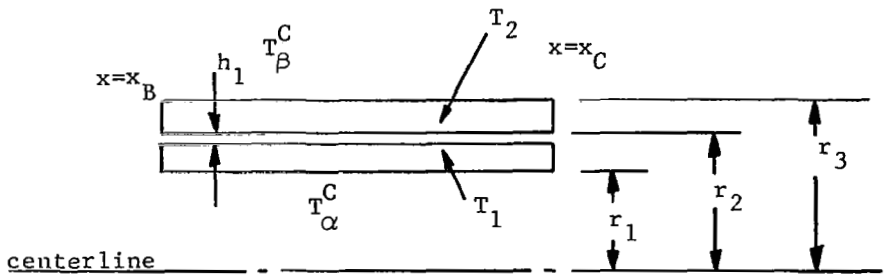

The heat conduction equation governing the interior is as follows.

$$\frac{\partial T_1}{\partial \tau} = \left(\frac{k_1}{\rho_1 c_1}\right)^C \frac{\partial^2 T}{\partial x^2} - \left(\frac{h_\alpha}{\rho_1 c_1 t_1}\right)^C \left(\frac{2r_1}{r_1+r_2}\right) (T_1 - T_\alpha^C)$$
$$+ \frac{\mu U^2}{2h_1} \left(\frac{1}{\rho_1 c_1 t_1}\right)^C \left(\frac{2r_2}{r_1+r_2}\right) + \left(\frac{k_f}{\rho_1 c_1 t_1}\right)^C \left(\frac{2r_2}{r_1+r_2}\right) \left(\frac{T_2-T_1}{h_1}\right) \quad (5)$$

$$\frac{\partial T_2}{\partial \tau} = \left(\frac{k_2}{\rho_2 c_2}\right)^C \frac{\partial^2 T}{\partial x^2} - \left(\frac{h_\beta}{\rho_2 c_2 t_2}\right)^C \left(\frac{2r_3}{r_2+r_3}\right) (T_2 - T_\beta^C)$$
$$+ \frac{\mu U^2}{2h_1} \left(\frac{1}{\rho_2 c_2 t_2}\right)^C \left(\frac{2r_2}{r_2+r_3}\right) - \left(\frac{k_f}{\rho_2 c_2 t_2}\right)^C \left(\frac{2r_2}{r_2+r_3}\right) \left(\frac{T_2-T_1}{h_1}\right) \quad (6)$$

The boundary conditions at $x = x_B$ are

$$k_1^B \; t_1^B \; (r_B+r_2) \left(\frac{\partial T_1}{\partial x}\right)^B = k_1^C \; t_1^C \; (r_1+r_2) \left(\frac{\partial T_1}{\partial x}\right)^C \quad (7)$$

$$k_2^C \left(\frac{\partial T_2}{\partial x}\right)^C = h_\beta^C \; (T_2 - T_\beta^C) \quad (8)$$

At $x = x_C$, the boundary conditions are

$$k_1^C \left(\frac{\partial T_1}{\partial x}\right)^C = k_1^D \left(\frac{\partial T_1}{\partial x}\right)^D \quad (9)$$

$$- k_2^C \left(\frac{\partial T_2}{\partial x}\right) = h_\beta^C \; (T_2 - T_\beta^C) \quad (10)$$

Section D

The governing equation of the interior points is the same as Section B; the boundary condition at $x = x_C$ is given in Section C; and the boundary condition at $x = x_D$ is the same as that at $x = x_B$.

Section E

The treatment for Section E is identical to that for Section C.

Section F

The treatment of the interior points of this section is the same as that for Section D except at $x = x_F$, the boundary condition is given in Section G.

Section G

The treatment of the interior points of this section is the same as that of Section A. The boundary condition at $r = r_1$ is

$$k_1^G \frac{\partial T_1}{\partial r} = h_\alpha^G (T_1 - T_\alpha^G) + k_1^F \left(\frac{r_1+r_2}{2r_1}\right) \frac{t_1^F}{t_1^G} \left(\frac{\partial T_1}{\partial x}\right) \tag{11}$$

where T_α^G is the compressor disk temperature. The boundary condition at $r = r_g$ is given in Section H.

Section H

The equation governing the interior points of this section are

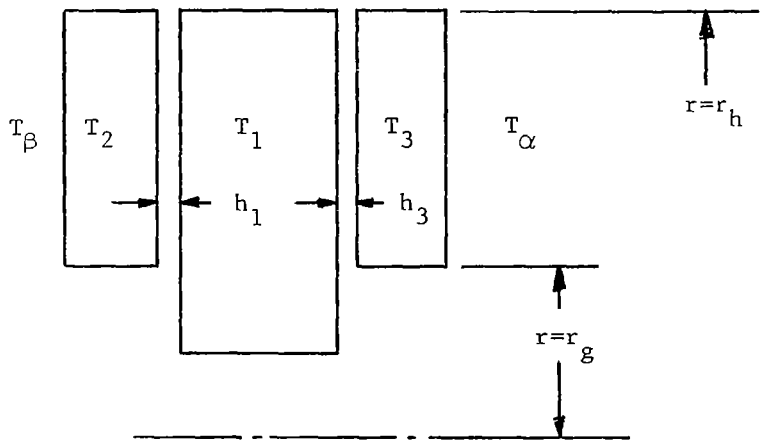

$$\frac{\partial T_1}{\partial \tau} = \left(\frac{k_1}{\rho_1 c_1}\right)^H \frac{1}{r} \frac{\partial}{\partial r} \left(r \frac{\partial T_1}{\partial r}\right) + \left(\frac{1}{2\rho_1 t_1 c_1}\right)^4 \mu\omega^2 r^2 \left(\frac{1}{h_1} + \frac{1}{h_3}\right) + \left(\frac{k_f}{\rho_1 c_1 t_1}\right)^H \left(\frac{T_2 - T_1}{h_1}\right) + \left(\frac{k_f}{\rho_1 c_1 t_1}\right)^H \left(\frac{T_3 - T_1}{h_3}\right) \tag{12}$$

$$\frac{\partial T_2}{\partial \tau} = \left(\frac{k_2}{\rho_2 c_2}\right)^H \frac{1}{r}\frac{\partial}{\partial r}\left(r\frac{\partial T_2}{\partial r}\right) + \left(\frac{1}{2\rho_2 c_2 t_2}\right)^H \mu\omega^2 r^2 \left(\frac{1}{h_1}\right) - \left(\frac{k_f}{\rho_2 c_2 t_2}\right)^H \left(\frac{T_2-T_1}{h_1}\right) - \left(\frac{h_\beta}{\rho_2 c_2 t_2}\right)^H (T_2-T_\beta) \quad (13)$$

$$\frac{\partial T_3}{\partial \tau} = \left(\frac{k_3}{\rho_3 c_3}\right)^H \frac{1}{r}\frac{\partial}{\partial r}\left(r\frac{\partial T_3}{\partial r}\right) + \left(\frac{1}{2\rho_3 c_3 t_3}\right)^H \mu\omega^2 r^2 \left(\frac{1}{h_3}\right) - \left(\frac{k_f}{\rho_3 c_3 t_3}\right)^H \left(\frac{T_3-T_1}{h_3}\right) - \left(\frac{h_\alpha}{\rho_3 c_3 t_3}\right)^H (T_3-T_\alpha) \quad (14)$$

The boundary conditions at r = rg are

$$\left(\frac{\partial T_1}{\partial r}\right)^G = \left(\frac{\partial T_1}{\partial r}\right)^H$$

$$\left(\frac{\partial T_1}{\partial r}\right)^G = \left(\frac{h_\alpha}{k_2}\right)^G (T_2 - T_\alpha{}^G) \quad (15)$$

$$\left(\frac{\partial T_2}{\partial r}\right)^G = \left(\frac{h_\beta}{k_3}\right)^G (T_3 - T_\beta{}^G)$$

The boundary conditions at r = r_h are

$$\left(\frac{\partial T_2}{\partial r}\right)^H = \left(\frac{T_2{}^{JP} - T_2{}^{JH}}{r_p - r_h}\right)$$

$$\left(\frac{\partial T_3}{\partial r}\right)^H = \left(\frac{T_3{}^{JP} - T_3{}^{JH}}{r_p - r_h}\right) \quad (16)$$

$$\left(\frac{\partial T_1}{\partial r}\right)^H = \frac{h_\gamma}{k_1{}^H} (T_1{}^{JH} - T_1{}^{JP})$$

Section P

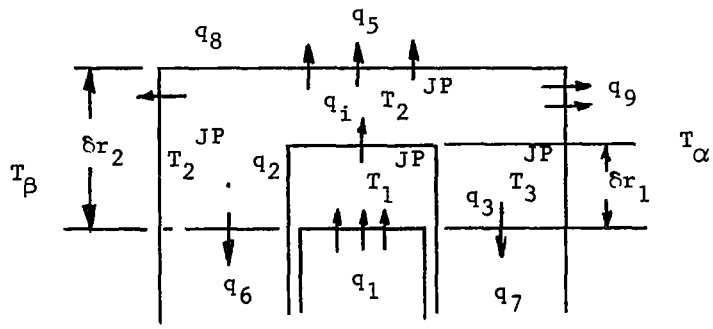

The temperature at the outside diameter of the stator is determined by the following gross heat balance of the section shown above.

$$\left.\begin{aligned} & T_3^{JP} - T_2^{JP} = 0 \\ & q_1 = q_2 + q_3 + q_4 \\ & \rho_2 c_2 \left[\pi(r_q^2 - r_h^2)(t_1+t_2+t_3) - \pi(r_p^2 - r_n^2)t_1\right] \frac{\partial T_2^{JP}}{\partial \tau} \\ & = (q_2 + q_3 + q_4) - (q_5 + q_6 + q_7 + q_8 + q_9) \end{aligned}\right\} \qquad (17)$$

where

$$q_1 = (T_1^{JH} - T_1^{JP})\ 2\pi\ t_1\ r_h\ h_\gamma$$

$$q_2 + q_3 + q_4 = (T_1^{JP} - T_2^{JP}) \left[2\pi(r_p^2 - r_h^2) + 2\pi\ r_p\ t_i\right] h_\gamma$$

$$q_6 + q_7 = \left(\frac{T_2^{JP} - T_2^{JH}}{r_p - r_h}\right) k_2^H\ 2\pi\ r_h\ t_2 + \left(\frac{T_2^{JP} - T_3^{JH}}{r_p - r_h}\right) k_3^H\ 2\pi\ r_h\ t_3$$

$$q_5 + q_8 + q_9 = (T_2^{TP} - T_\alpha^H)\, h_\alpha \left[\pi(r_q^2 - r_h^2) + 2\pi\, r_q\, (t_1+t_2+t_3)\right]$$

Calculation of Enclosure Temperature

The ambient temperature in the enclosure is calculated from the gross heat balance between the total heat released to the enclosure from all exposed facings and the heat absorbed by the gas in the enclosure. This consideration gives the following equation.

$$\int_s h\,(T_S - T_E)\, dA = \rho_g c_g\, V \frac{\partial T_E}{\partial \tau} \tag{18}$$

where

T_S = temperature of the exposed surface

T_E = enclosure temperature

ρ_g = density of the gas in the enclosure

C_g = specific gravity of the gas in the enclosure

V = volume of the enclosure

Numerical Solution

Approximating the derivatives in the above governing equations by their implicit-type, finite difference equivalents, Eqs. (1) to (18) can be put into the following matrix form.

$$A \left\{T\right\}^{j} + B \left\{T\right\}^{j-1} + C \left\{T\right\}^{j+1} = D \tag{19}$$

where $\left\{T\right\}^{j}$ represents a column of three temperatures at the jth grid point. The grid point begins at the outside diameter of the turbine disk and ends at the outside diameter of the thrust stator. Equation (19) can be readily solved by the method described in Ref. 19. to yield transient temperatures at each time interval. Between the successive time intervals, the enclosure temperature is calculated by Eq. (18).

APPENDIX B

PERFORMANCE OF DISTORTED TILTING PADS

NOMENCLATURE for Appendix B

$B_P = \frac{p_a R^4}{I_p C_r \frac{\Omega^2}{4}}$ = dimensionless pitch inertia of pad

$B_M = \frac{p_a R^2_{os}}{m_p C_R \frac{\Omega^2}{4}}$ = dimensionless mass parameter

$B_R = \frac{p_a R^4}{I_R C_R \frac{\Omega^2}{4}}$ = dimensionless roll inertia of pad

$C' = \frac{C'}{C_R}$ dimensionless radial pivot motion

C' = radial displacement of pivot point from the position in which the undistorted pad and shaft are concentric with x = y = 0, inches

C_R = reference clearance (arbitrary), inches

d = distance from pivot point to pad surface, inches

$D = \frac{d}{R}$ = dimensionless pivot-surface distance

$G(z)$ = local radial temperature gradient of pad, ^{o}F/inch

$h(\theta,Z)$ = local film clearance, inches

$H = \frac{h}{C_R}$ = dimensionless local clearance

I_p = moment of inertia of pad about pivoted pitch axis, in.lb.sec^2

I_R = moment of inertia of pad about pivoted roll axis, in.lb.sec^2

N = number of pads in a bearing

p = local film pressure, psia

p_a = ambient pressure, psia

$P = p/p_a$ dimensionless local film pressure

$P_L = \frac{\text{load}}{p_a R^2_{os}}$ = dimensionless load

Nomenclature for Appendix B (Cont'd).

$R_s(z)$ = distorted shaft radius, inches

R_{op} = undistorted pad radius, inches

R_{os} = undistorted shaft radius, inches

t = time, seconds

T = $t\frac{\Omega}{2}$ = dimensionless time

$T_p(z)$ = local radial mean of pad temperature, ^oF

$T_s(z)$ = temperature of shaft, ^oF

$w_3(z)$ = pad rib thermal distortion, inches

x,y = shaft center coordinates with respect to non moving frame, inches

Z = $\frac{z}{R_{os}}$ dimensionless axial coordinate

Z_p = $\frac{z_p}{R}$ dimensionless axial pivot position

α_s = coefficient of thermal expansion of shaft, $1/^oF$

α_p = coefficient of thermal expansion of pads, $1/^oF$

γ = pitch angle (positive if it increases leading edge clearance), radians

Γ = $\frac{\gamma R}{C_R}$ = dimensionless pitch angle

δ = roll angle (positive if it increase the clearance in the + z-direction from the pivot point), radians

Δ = $\frac{\delta R}{C_R}$ = dimensionless roll angle

θ = angular coordinate measured from the y-axis in the direction of shaft rotation, radians

Λ = $\frac{6\mu\Omega R_{os}^2}{P_a C_R^2}$ = dimensionless bearing number

μ = lubricant viscosity, $lb.sec/in^2$

φ = angular coordinate measured from the pivot point against the direction of shaft rotation

ψ = PH

Ω = shaft angular velocity, radians/second

ANALYTICAL APPROACH

Due to the inherent promise of the tilting pad configuration as a high temperature application bearing; it was deemed desirable to analyze its performance by a method sufficiently versatile to accommodate both steady-state and dynamic operation. This goal could be achieved by economically utilizing a newly developed technique which solves the time transient Reynolds equation with a substantial saving in computer time compared with previously available methods. Then, both the dynamic behavior and the steady state performance charts can be obtained by running a single routine thus affording an efficient use of manpower and funds. Another advantage offered by the use of time transient approaches in obtaining steady state information is that running speeds, lubricant viscosity, pivot position and load are the imposed parameters and the pad attitude and film configuration are the results thus obviating the need of bulidng general field maps to isolate the performance of a configuration with specified pivot position. The latter problem is common with most approaches for solving the steady state Reynolds equation by specifying the film thickness distribution and running conditions and evaluating the resulting load and its attitude.

The general purpose of the program was twofold: a) given the shaft and pad temperature distributions, evaluate their shapes; b) given the shaft and pad shpaes, the load, the speed, the pivot position and the viscosity, evaluate the running clearance distribution.

The analysis was carried out for a single pad because in a bearing with N pads of equal dimensions, symmetrically located with respect to the load line, and when (N-2) pad have a specified preload, the external shaft load completely determines the load supported by each pad.

The resulting routine can then be used for three basic tasks: 1) analyze the steady state performance of each pad; 2) analyze the dynamic behavior of each pad; 3) be made part of a larger program which calculates the performance of a general N pad bearing. Detailed analysis for the single pad as well as for the multipad performance are given in the following parts of this Appendix.

SINGLE PAD ANALYSIS

The following is a description of the single pad analysis.

a) Thermal distortion

The analysis of the thermal distortion problem for both the shaft and the pad was performed making use of some approximations which are consonant with the scope of the present work. The shaft is considered to have a purely axial temperature distribution which makes itsradius vary by thermal expansion due to the local value of the temperature (as if the shaft were cut into an axial series of thin circular disks).

$$R_s(z) = R_{os} + \alpha_s R_{os} T_s(z) \qquad (1)$$

The pads are considered as an asymmetrical rib cage where an axially oriented beam through the pivot point is the spine and many circumferential beams are the ribs (which are rigidly attached to the spine). The temperature profile is considered to be given by the superposition of a purely axial distribution and an axially varying radial temperature gradient. Then the distortion is due to three factors: 1) change in radius of each rib due to local mean temperature

$$(\Delta R_1)\ (z) = \alpha_p R_{op} T_p\ (z) \qquad (2)$$

2) change in radius of each rib due to the local radial temperature gradient. Using thin beam analysis:

$$(\Delta R_2)\ (z) = \frac{1}{2} \alpha_p R_{op}^2 G\ (z) \qquad (3)$$

3) distortion of the spine due to radial temperature gradient distribution with consequent translation of the ribs. The local deflection is governed by

$$\frac{d^2 w_3}{d z^2} = - \alpha_p G(z) \qquad (4)$$

with the boundary conditions:

$$w_3 = \frac{dw_3}{dz} = 0 \text{ at } z = z_p \text{ (pivot point)}$$

since the radial pivot translation and pad roll motion are specified elsewhere.

Equation (4) can be easily integrated numerically.

b) Film and pad dynamics

From the results of the previous section and the nomenclature introduced by Fig. B.1, the film distribution (including the effects of shaft motion, pad pitch, pad roll, and pad radial motion) is

$$h = R_{op} - R_s(z) + (\Delta R_1)(z)(1-\cos\varphi) + (\Delta R_2)(z)(1-\cos\varphi) +$$
$$+ w_3(z)\cos\varphi + x\sin\theta + y\cos\theta +$$
$$C'\cos\varphi + \gamma(d + R_{op})\sin\varphi + \delta(z - z_p)\cos\varphi$$

where C' = radial pivot motion
γ = pitch angle (+ to increase h at leading edge)
δ = roll motion (+ to increase h in the +z direction)

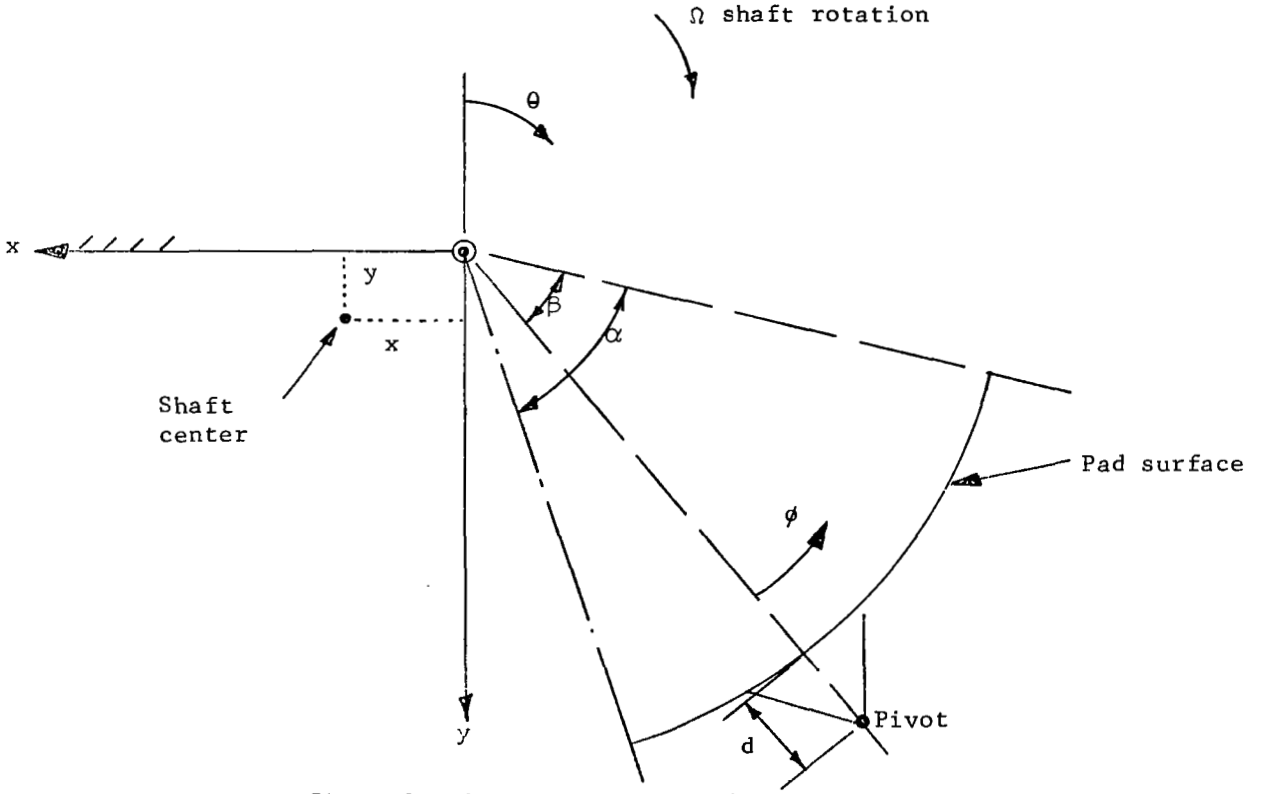

Fig. B-1 Pad Position Schematic

The dynamics of the system produce variations in the rigid body motion variables of the pad C', γ, δ (also x,y for cases in which the shaft dynamics are included).

The film dynamics and pad dynamics are coupled and the respective equations are solved by a step by step integration forward in time.

The film equation is (in dimensionless form)

$$\Lambda \frac{\partial \psi}{\partial T} = \left[H\psi \frac{\partial^2 \psi}{\partial \theta^2} - \psi^2 \frac{\partial^2 H}{\partial \theta^2} + H \left(\frac{\partial \psi}{\partial \theta}\right)^2 + \right.$$

$$- \psi \frac{\partial \psi}{\partial \theta} \frac{\partial H}{\partial \theta} - \Lambda \frac{\partial \psi}{\partial \theta} + H\psi \frac{\partial^2 \psi}{\partial Z^2} - \psi^2 \frac{\partial^2 H}{\partial Z^2} + \qquad (6)$$

$$\left. + H \left(\frac{\partial \psi}{\partial Z}\right)^2 - \psi \frac{\partial \psi}{\partial Z} \frac{\partial H}{\partial Z} \right]$$

where $\psi = PH$

$R = R_{os}$

The dynamics equations are (in dimensionless form)

$$\frac{d^2 C'}{dT^2} = B_M \left[\iint (P-1) \cos\varphi \, dZ \, d\theta - P_L \right] \qquad (7)$$

$$\frac{d^2 \Gamma}{dT^2} = B_P \iint (P-1)(D+1) \sin\varphi \, dZ \, d\theta \qquad (8)$$

$$\frac{d^2 \Delta}{dT^2} = B_R \iint (P-1)(Z-Z_P) \cos\varphi \, dZ \, d\theta \qquad (9)$$

The solution of Eq. (6) is performed in sequential time steps by the technique presented in Ref. B.1.* At each time step equations (7), (8) and (9) utilize the loads and moments in their right-hand-sides to produce a change in velocity and position of the three degrees of freedom C', Γ and Δ.

Thus, starting from some initial conditions in C', $\frac{dC'}{dT}$, Γ, $\frac{d\Gamma}{dT}$, Δ, and $\frac{d\Delta}{dT}$,

* Ref. B.1 Castelli, V. and C.H.Stevenson, A Semi-implicit Numerical Method for Treating the Time Transient Gas Lubrication Equation," MTI Report 67TR14.

and P, the transient is calculated to give dynamic characteristics and the steady-state running condition (if stable). When the steady-state position only is desired, the possibility of long transients is eliminated by imposing an external damper in the equations of motion, i.e. adding a term proportional to $\frac{dC'}{dT}$, $\frac{d\Gamma}{dT}$ and $\frac{d\Delta}{dT}$ in the Equations (7), (8) and (9)respectively.

Multi-pad Analysis

a. Load Distributions of Fixed Pads

In a preloaded N-pad journal bearing, only two pads are fixed and the rest of the pads are preloaded by specified loads, W_i. Thus, the external shaft load vector completely determines the load exerted upon each fixed pad.

Designating numbers 1 and 2 to the fixed pads, and denoting W and ϕ as the external load and attitude angle, the load exerted on the fixed pads, W_1 and W_2, can be determined from the equilibrium condition and expressed in the following matrix form:

$$\begin{Bmatrix} W_1 \\ W_2 \end{Bmatrix} = [C]^{-1} \begin{Bmatrix} -\sum_3^N W_i \cos\theta_i \\ -\sum_3^N W_i \sin\theta_i \end{Bmatrix} - W [e]^{-1} \begin{Bmatrix} \cos\phi \\ \sin\phi \end{Bmatrix} \qquad (10)$$

where i = 3,4 ... N and

$$[C] = \begin{bmatrix} \cos\theta_1 & \cos\theta_2 \\ \sin\theta_1 & \sin\theta_2 \end{bmatrix} \qquad (11)$$

2. Film Thickness Distributions for Each Pad

Knowing the load exerted upon each pad, the single pad analysis described in the preceding section can be used to determine the attitude and film thickness distributions for each pad with or without the thermal distortion.

3. Resonating Frequency Ratios

If the pad is allowed to pitch without radial translation of the pivot or roll motion, the resonating frequency in the pitch mode is governed by,

$$\omega_p = \sqrt{\frac{k_p}{I_p}} \tag{12}$$

where ω_p = pitch resonating frequency, rad/sec.
k_p = angular stiffness in the pitch direction, in.lb/rad
I_p = mass moment of inertia in the pitch direction, lb.in.sec^2

The stiffness in the pitch direction is computed by determing the change in pitch angle for a small change of pitching moment about the equilibrium position of the pad. Thus

$$k_p \cong \frac{\Delta M_p}{\Delta \gamma} \tag{13}$$

where ΔM_p is a small change of pitch moment. The ratio of the pitch resonating frequency to the running frequency becomes

$$N_p = \frac{\omega_p}{\Omega}$$

$$= \frac{1}{\Omega} \frac{k_p}{I_p}$$

or

$$\frac{N_p}{N} = \frac{1}{2}\sqrt{B_p \bar{k}_p} \tag{14}$$

where $\bar{k}_p = \frac{G_R}{p_a R^4} \frac{\Delta M_p}{\Delta \gamma}$

Likewise, the roll resonating frequency ratio can be expressed as

$$\frac{N_R}{N} = \frac{1}{2}\sqrt{B_R \bar{k}_R} \tag{15}$$

where $\bar{k}_R = \frac{C_R}{p_a R^4} \frac{\Delta M_R}{\Delta \delta}$

The mass moment of inertia of each pad is calculated according to the expression given in Ref. 3 of the main text.for tilting pads.

For the preloaded pads, it is also desirable to know the resonating frequency ratio in the radial translatory mode. This ratio is calculated in the same manner as for the pitch and roll drection. However, for the four-pad bearing considered in this report, it was found that the frequency ratio in the radial mode is considerably higher than the frequency ratio in the pitch mode. Therefore, if the pad responds well to the shaft motion in the pitch direction, it should track even more satisfactorily in the radial mode.

4. Radial Stiffness of the Multi-pad Bearing

By calculating the change in displacement in x and y directions for a small change of load in each direction, one can readily determine the direct and cross-coupling stiffness of a multi-pad journal bearing. However, for the four-pad configuration the stiffness is the same in all directions, and it is obtained by determining the change in radial displacement for a small increase in the load. The radial stiffness curves presented earlier are calculated by this procedure.

5. Power Loss

The frictional torque due to the Couette flow for each pad can be expressed as

$$T_c = \int_{-\frac{L}{2}}^{+\frac{L}{2}} \int_{0}^{\alpha} \frac{\mu U}{h} R^2 \, d\theta \, dz$$

$$= \frac{\mu \omega R^4}{C_R} \int_{-\frac{L}{D}}^{+\frac{L}{D}} \int_{0}^{\alpha} \frac{1}{H} \, d\theta \, d\bar{z} \qquad (16)$$

The frictional component due to the Poiseuille flow for each pad

$$T_P = \frac{W(R+d)}{2} \gamma = \bar{W} p_a R^2 \frac{(1+D)}{2} C_R \Gamma \qquad (17)$$

where W is the pad load.

Fhe total frictional torque for all pads can be summed as

$$T = \sum_{i=1}^{N} (T_c + T_p)_i \tag{18}$$

and the frictional hosepower is

$$FHP = \frac{T\Omega}{6600} \tag{18}$$

APPENDIX C

ANALYSIS OF MULTI-FOIL JOURNAL BEARING

NOMENCLATURE

W_1 - Load on the fixed foil #1, lb.

W_2 - Load on the fixed foil #2, lb.

W - Total load, lb.

W_x, W_y - Components of load W along x and y direction.

N - No. of foils

C Matrix defined in Eq. (2)

i - Index of foil.

θ_1 - Load angle of foil #1 (see Fig. C-1), deg.

θ_2 - Load angle of foil #2 (see Fig. C-1), deg.

ϕ - Attitude angle, deg. (see Fig. C-1).

T_i - Unit tension of i'th foil, lb/in.

b_i - Width of i'th foil, in.

β_i - Wrap angle of i'th foil, deg. (see Fig. C-2).

L_i - The distance between two terminals of the i'th foil, (see Fig. C-2), in.

ℓ_i - Length of the i'th foil, in. (see Fig. C-2).

R_i - Radius of the i'th foil, in. (see Fig. C-2).

Y_i - Center distance of the i'th foil, in. (see Fig. C-2).

ΔF_i - Temperature differential of the i'th foil, between the operation condition and the initial condition, ^{o}F.

ℓ_{oi} - Initial length of the i'th foil, in.

α_i - Coefficient of thermal expansion of the i'th foil, in/in.-^{o}F.

E_i - Young's modulus of the i'th foil, lb/in.^{2}

t_i - Thickness of the i'th foil, in.

h_i - Mean film height of the i'th foil, in.

U - Journal speed, in/sec.

p_a - Ambient pressure, PSIA

μ - Viscosity, lb-sec/in.^{2}

H_i - Defined in Eq. (9).

S_1, S_2 - Defined in Eq. (11).

G_1, G_2, G_3 - Defined in Eq. (13).

p_1, p_2 - Defined in Eq. (15).

Q_1, Q_2 - Defined in Eq. (7).

x, y - Coordinates, inches

A. Load Distribution on Each Foil

Figure C-1 shows the schematics of a multi-foil journal bearing in which the shaft is supported by a number of thin tapes. Two foils are considered to be fixed, and are designated as numbers 1 and 2 with the foil position angle θ_1 and θ_2. The remaining foils are considered to be preloaded foils having specified loads.

Denote W and $\emptyset$ as the load and its attitude angle (see Fig. C-1). The load on the fixed foils 1 and 2 are expressed as W_1 and W_2 and they can be determined from the equilibrium condition. Thus,

$$\begin{Bmatrix} W_1 \\ W_2 \end{Bmatrix} = \begin{bmatrix} C \end{bmatrix}^{-1} \begin{Bmatrix} -\sum_{3}^{N} W_i \cos\theta_i \\ -\sum_{3}^{N} W_i \sin\theta_i \end{Bmatrix} - W \begin{bmatrix} C \end{bmatrix}^{-1} \begin{Bmatrix} \cos \emptyset \\ \sin \emptyset \end{Bmatrix} \tag{1}$$

where i = 3,4 .... N and

$$\begin{bmatrix} C \end{bmatrix} = \begin{bmatrix} \cos\theta_1 & \cos\theta_2 \\ \sin\theta_1 & \sin\theta_2 \end{bmatrix} \tag{2}$$

B. Unit Tension (per unit width) in Each Foil

Once the load on each individual foil is found, the foil tension can be established from the foil geometry (Fig. C-2).

Under the equilibrium, one has

$$T_i = \frac{W_i / b_i}{2 \sin\frac{\beta_i}{2}} \tag{3}$$

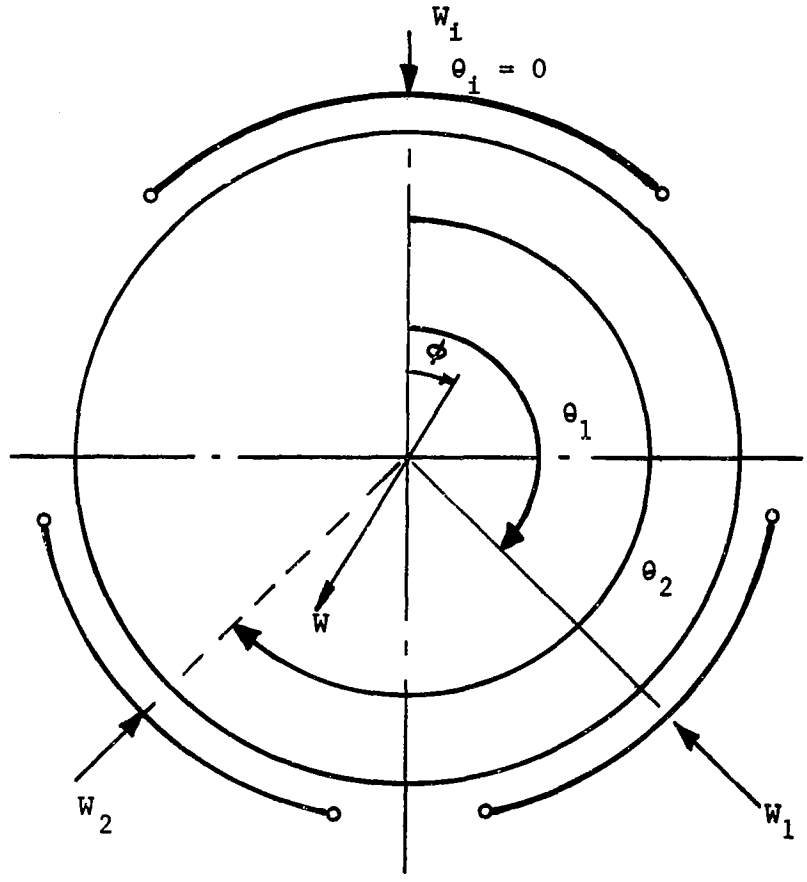

Fig. C-1 Schematic of a Multi-Foil Journal Bearing

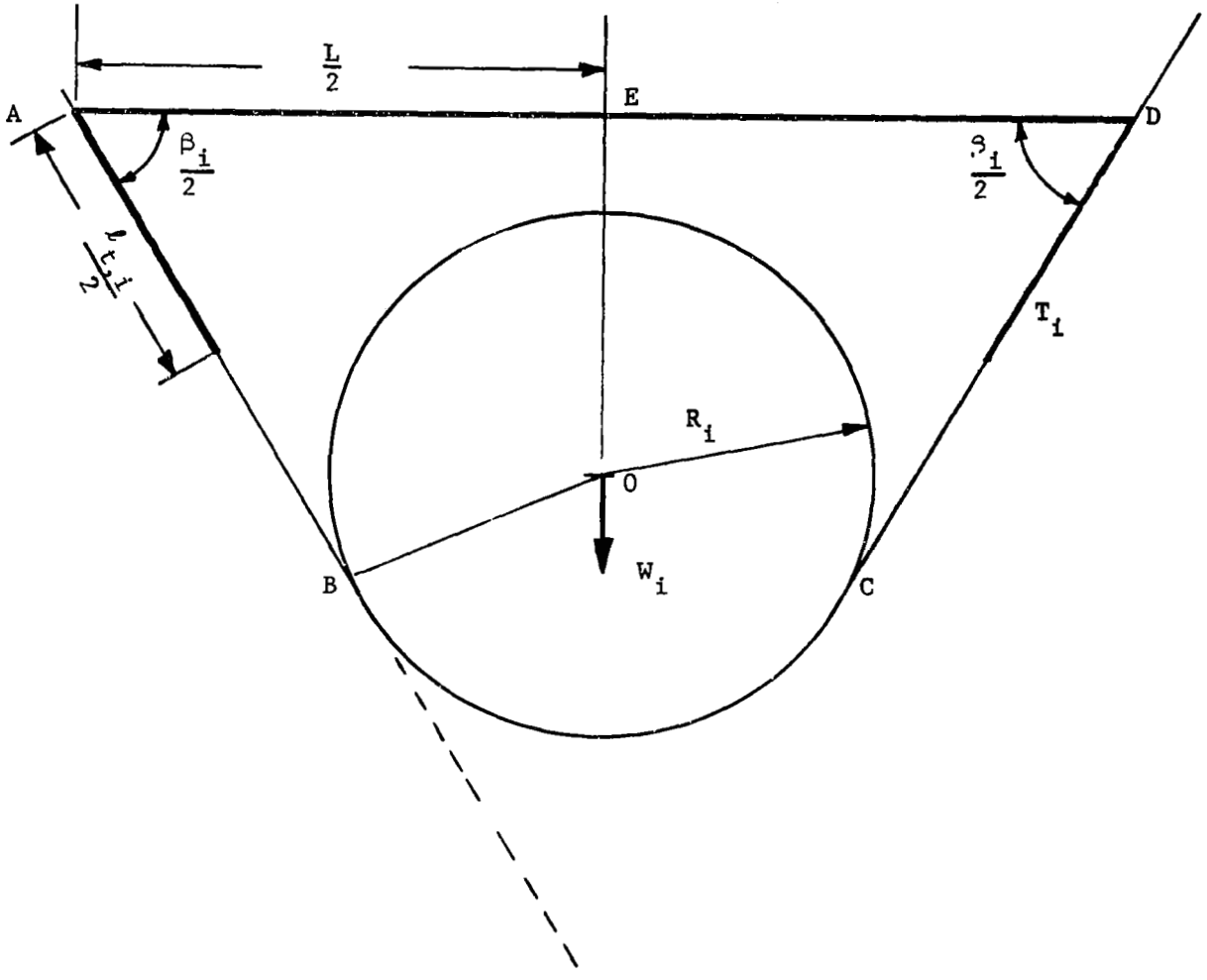

Fig. C-2 Geometry of a Typical Foil

Where T_i = unit tension per unit of width, lb/in.

β_i = wrap angle

b_i = width of foil, in.

C. Geometrical Relationship Between Foil Length, Wrap Angle, Center Distance and the Bearing Radius

From Fig. C-2, one obtains

$$\sin \frac{\beta_i}{2} \left[\frac{\ell_i}{2} - \frac{R_i \beta_i}{2} \right] = Y_i + R_i \cos \frac{\beta_i}{2} \tag{4}$$

$$\frac{L_i}{2} = \left(\frac{\ell_i}{2} - \frac{R_i \beta_i}{2} \right) \cos \frac{\beta_i}{2} + R_i \sin \frac{\beta_i}{2} \tag{5}$$

where L_i = AD, the distance between the two terminals of a tape (see Fig. 2), in.

ℓ_i = Individual tape length, in.

R_i = Radius of foil bearing, in.

D. Length of Foil Under Stretching and Heating

$$\frac{\ell_i}{2} = \frac{\ell_{oi}}{2} (1 + \alpha_i \Delta F_i) \left(1 + \frac{T_i}{E_i t_i} \right) \tag{6}$$

Where ℓ_{oi} = initial length of the foil.

α_i = coefficient of thermal expansion, in/in-^{o}F.

E_i = Young's modulus of each individual tape, lb/in.

t_i = thickness of each individual tape, in.

E. Radius of Foil Bearing Under Heating and Loading

$$R_i = R_o (1 + \alpha_i \Delta F_i) + h_i$$

where R_o = Initial radius of journal, in.

h_i = Mean film height of each foil, in. (7)

F. Mean Film Height of Foil

From Ref. 13, one can obtain the nominal film thicknesses of the foil to be

$$h_i = H_i R_o (1 + \alpha_i \Delta F_i) \left(\frac{6 \mu U}{T_i}\right)^{2/3} \quad (8)$$

where H_i is a function of the foil stiffness in bending and the compressibility number defined as

$$\lambda = \frac{T_i}{P_a R_o (1 + \alpha_i \Delta F_i)}$$

From the data published in Ref. 13, one can deduct H_i as an empirical expression in terms of H_i^* and λ. The expression is

$$H_i = H_i^* e^{\lambda (.044\lambda - .344)} \quad (9)$$

H_i^* is a function of the foil stiffness in bending. For a perfectly flexible foil, H_i^* is equal to 0.643. This value is used in this report.

G. The Relationship Between Load and Journal Center of Each Individual Foil

From Ews. (3), (4), (6), (8), and (9) one can express the variation of ΔY_i, change of journal center, in terms of ΔW_i, change of load for each foil, as follows:

Differentiating, Ews. (3) and (6), one has

$$\frac{d\ell_i}{2} = S_1 dW_i + S_2 \, d \frac{\beta_i}{2} \quad (10)$$

$$\text{where } S_1 = \frac{\ell_{oi}}{2E_i\ t_i} \quad x \quad \frac{(1 + \alpha_i \Delta F_i)}{2\ b_i \sin \frac{\beta_i}{2}} \tag{11}$$

$$S_2 = S_1\ W_i \cot \frac{\beta_i}{2}$$

Differentiating Eq. (4), one has

$$d\frac{\beta_i}{2} = G_1\ d\left(\frac{\ell_i}{2}\right) + G_2\ dY_i + G_3\ dR_i \tag{12}$$

$$\text{where } G_2 = \frac{1}{\left(\frac{\ell_i}{2} - \frac{\beta_i}{2} R_i\right) \cos \frac{\beta_i}{2}}$$

$$G_1 = -G_2 \sin \frac{\beta_i}{2}$$

$$G_3 = \left(\cos \frac{\beta_i}{2} + \frac{\beta_i}{2} \sin \frac{\beta_i}{2}\right) G_2 \tag{13}$$

Differentiating Eq. (5), one has:

$$d\frac{\beta_i}{2} = P_1\ d\left(\frac{\ell_i}{2}\right) + P_2\ dR_i \tag{14}$$

$$\text{where } P_1 = \cos \frac{\beta_i}{2} \Big/ \left(\frac{\ell_i}{2} - R_i \frac{\beta_i}{2}\right) \sin \frac{\beta_i}{2} \tag{15}$$

$$P_2 = \left[\tan \frac{\beta_i}{2} - \frac{\beta_i}{2}\right] P_1$$

Differentiating Eqs. (8) and (9), one has

$$dR_i = Q_1\ dW_i + Q_2\ d\frac{\beta_i}{2} \tag{16}$$

$$\text{where } Q_1 = -\frac{h_i}{3\ T_i\ b_i \sin \frac{\beta_i}{2}} \left[1 - \frac{3}{2}\lambda\ (.008\lambda - .344)\right]$$

$$Q_2 = -\ Q_1\ W_i \cot \frac{\beta_i}{2} \tag{17}$$

Finally, eliminating dR_i, $d\frac{\ell_i}{2}$ and $d\frac{\beta_i}{2}$ from Eqs. (10), (12), (14) and (16), one can express dW_i in terms of dY_i,

$$dW_i = \frac{G_2}{\frac{1-G_1S_2-G_3Q_2}{1-S_2P_1-P_2Q_2}\ (P_1S_1 + P_2Q_1) - G_1S_1-G_3Q_1} dY_i \tag{18}$$

H. The Stiffness Components of Foils 1 and 2

The sketch below shows the journal position after it is displaced from the origin of the coordinates. The geometric relation is

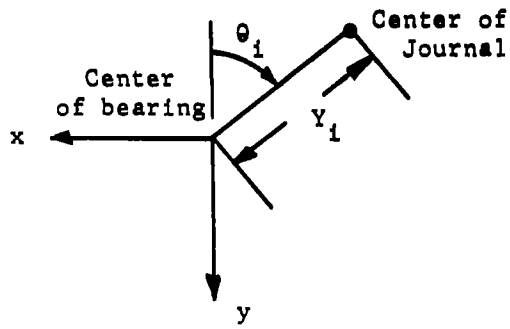

Sketch of the Geometric Relation of the Bearing and Journal Center

$$x \sin \theta + y \cos \theta_i = -Y_i,\ i = 1,2 \tag{19}$$

Differentiating Eq.(19), one has

$$\sin \theta_i\ dx + \cos \theta_i\ dy = -dY_i \tag{20}$$

The stiffness components can be obtained by differentiation of the total load with respect to the coordinates.

From Eq. (1), we can obtain the components of W in the x and y directions, i.e. W_x and W_y respectively. Writing W_x and W_i in terms of W_i we have:

$$W_y = -W_1 \cos\theta_1 - W_2 \cos\theta_2 - \sum_{3}^{N} W_i \cos\theta_i \tag{21}$$

$$W_x = -W_1 \sin\theta_1 - W_2 \sin\theta_2 - \sum_{3}^{N} W_i \sin\theta_i \tag{22}$$

From Eqs. (21), (22), and (20), one has

$$\left.\begin{aligned} \frac{dW_x}{dx} &= \frac{dW_1}{dY_1} \sin^2\theta_1 + \frac{dW_2}{dY_2} \sin^2\theta_2 \\ \frac{dW_y}{dy} &= \frac{dW_1}{dY_1} \cos^2\theta_1 + \frac{dW_2}{dY_2} \sin^2\theta_2 \\ \frac{dW_x}{dy} &= \frac{1}{2}\frac{dW_1}{dY_1} \sin 2\theta_1 + \frac{1}{2}\frac{dW_2}{dY_2} \sin 2\theta_2 \\ \frac{dW_y}{dx} &= \frac{dW_x}{dy} \end{aligned}\right\} \tag{23}$$

$\frac{dW_i}{dY_i}$ are calculated according to Eq. (18)

I. Method of Computation

The given quantities for a foil bearing design are:

W, $\emptyset$, b_i, L_i, α_i, ΔF_i, E_i, t_i, R_o. It is seen that ℓ_i and β_i are implicitly expressed in Eqs. (4), (5), (6), and (8). An iterative procedure is adopted to solve for ℓ_i and β_i, by first guessing β_i at no thermal gradient and tension. After the corrected values of ℓ_i and β_i are found, the fluid film thickness and the stiffness components are readily determined from Eqs. (8) and (23). respectively.

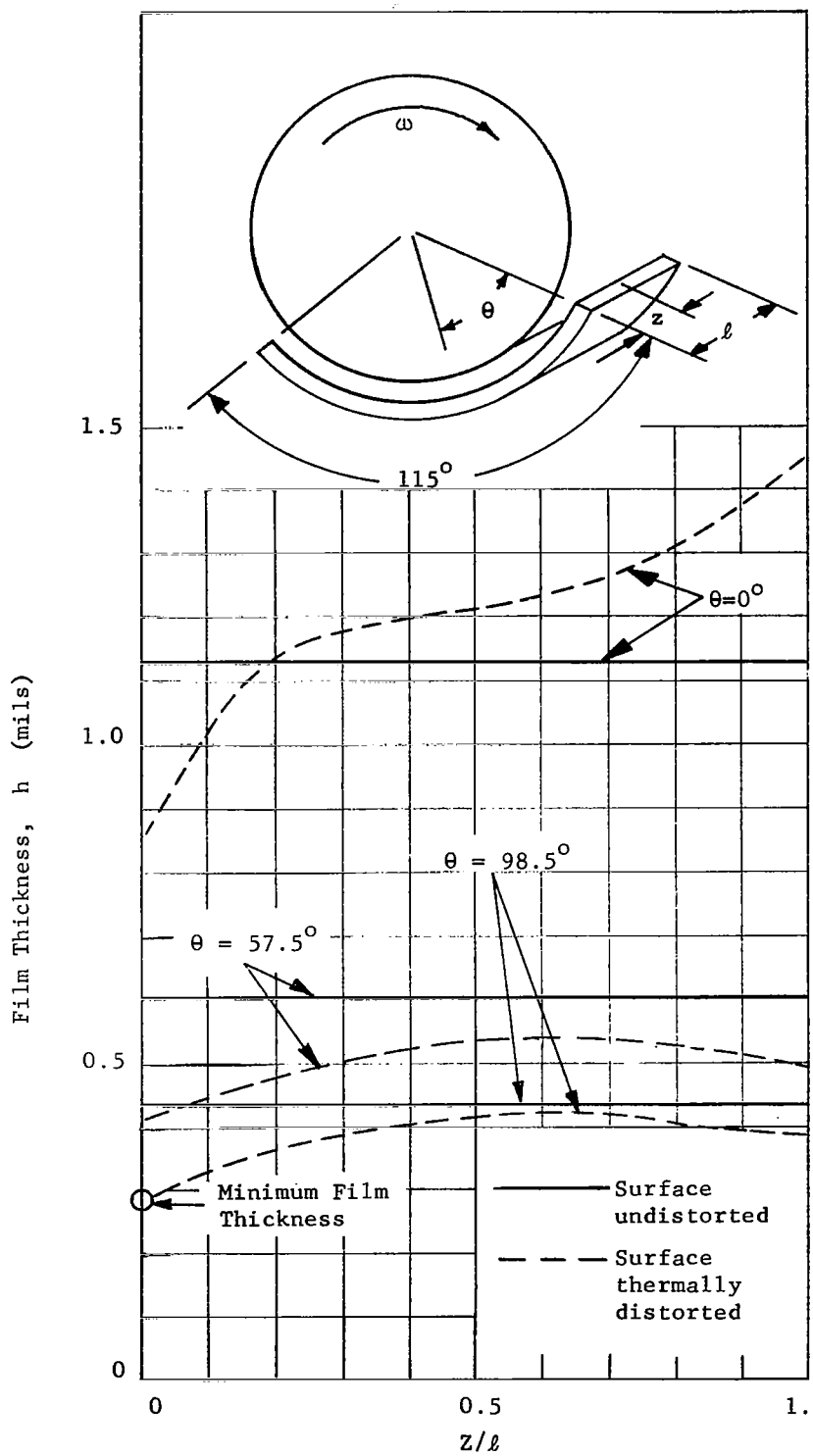

Fig. 1 Axial Film Thickness Distributions for Thermally Distorted Tilting Pad Journal Bearings, (case A, p_a = 5 psia).

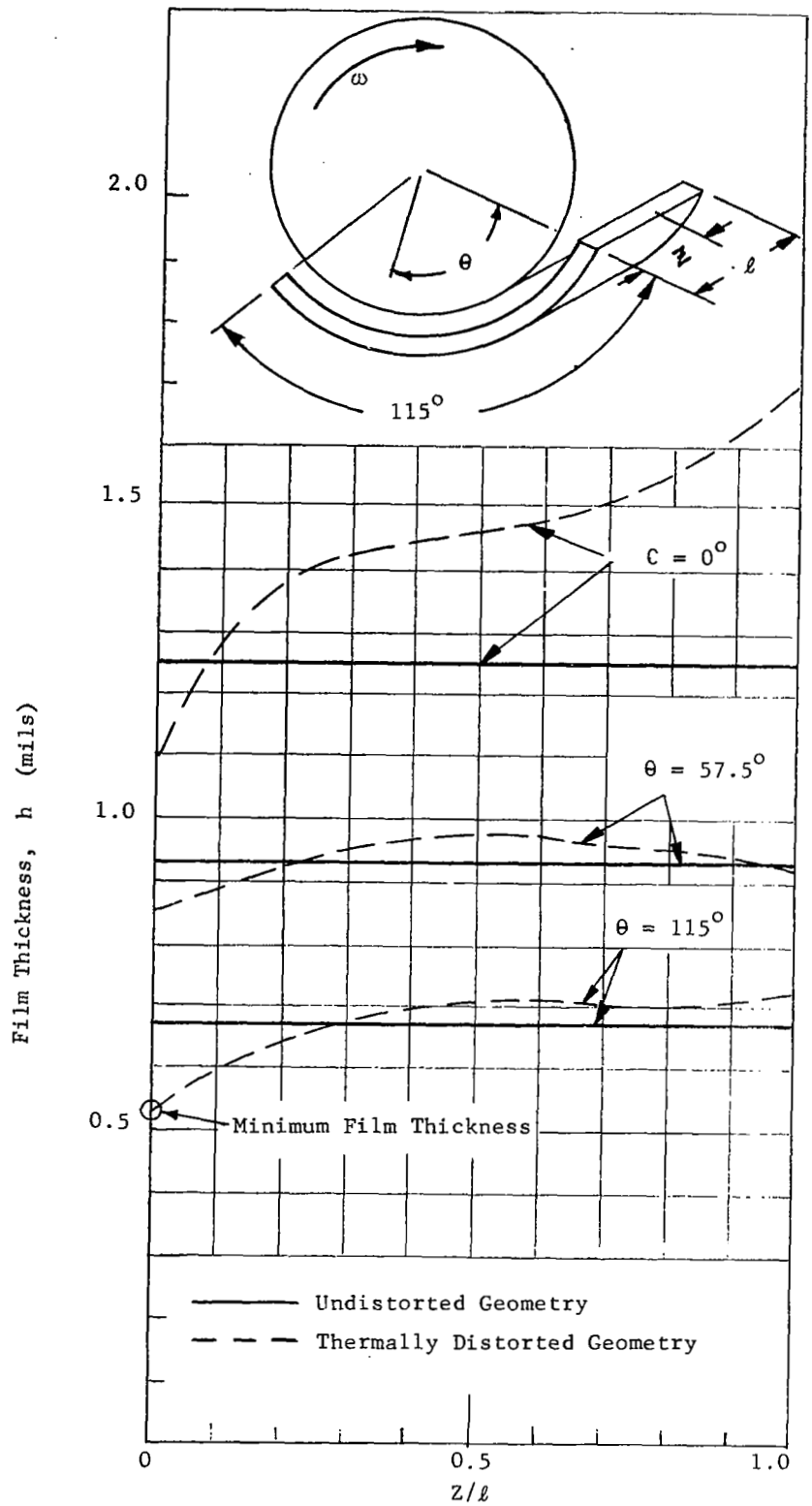

Fig. 2 Axial Film Thickness Distributions for Thermally Distorted Tilting Pad Journal Bearing (Case B, p_a = 15 psia)

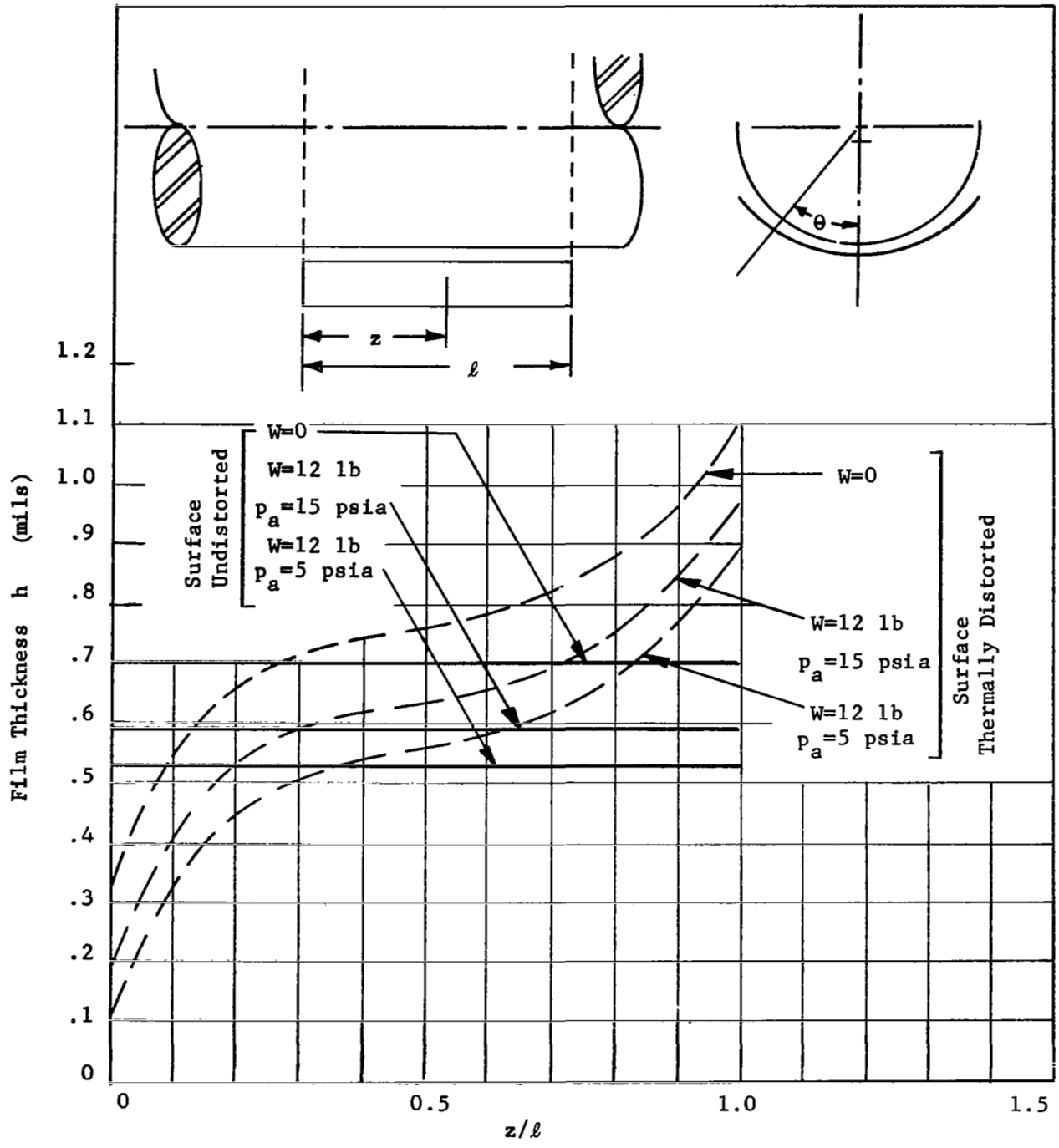

Fig. 3 Herringbone Journal Bearing Axial Film Thickness Distribution at θ = 0.

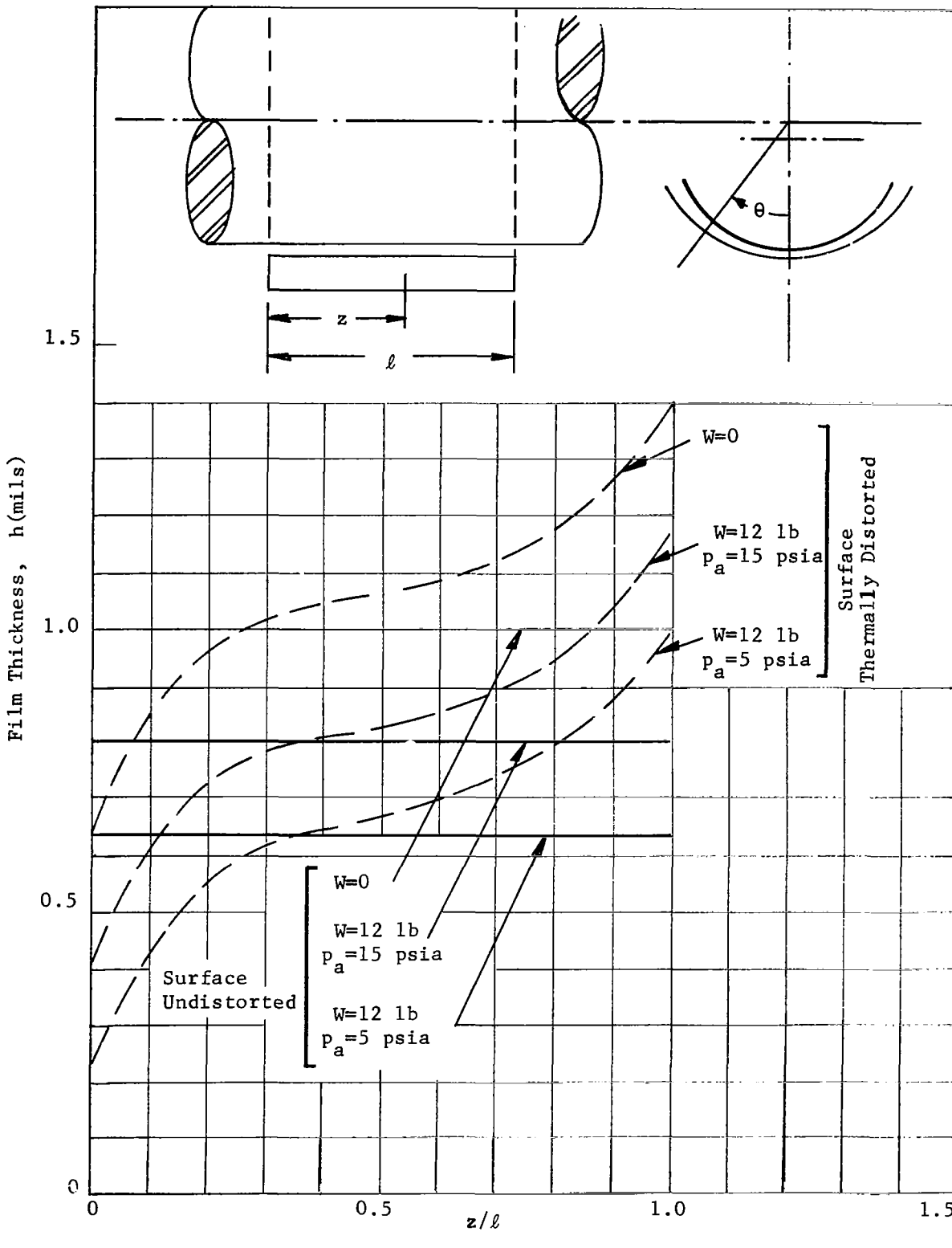

Fig. 4 Hydrostatical Mounted Cylindrical Axial Film Thickness Distribution at θ = 0

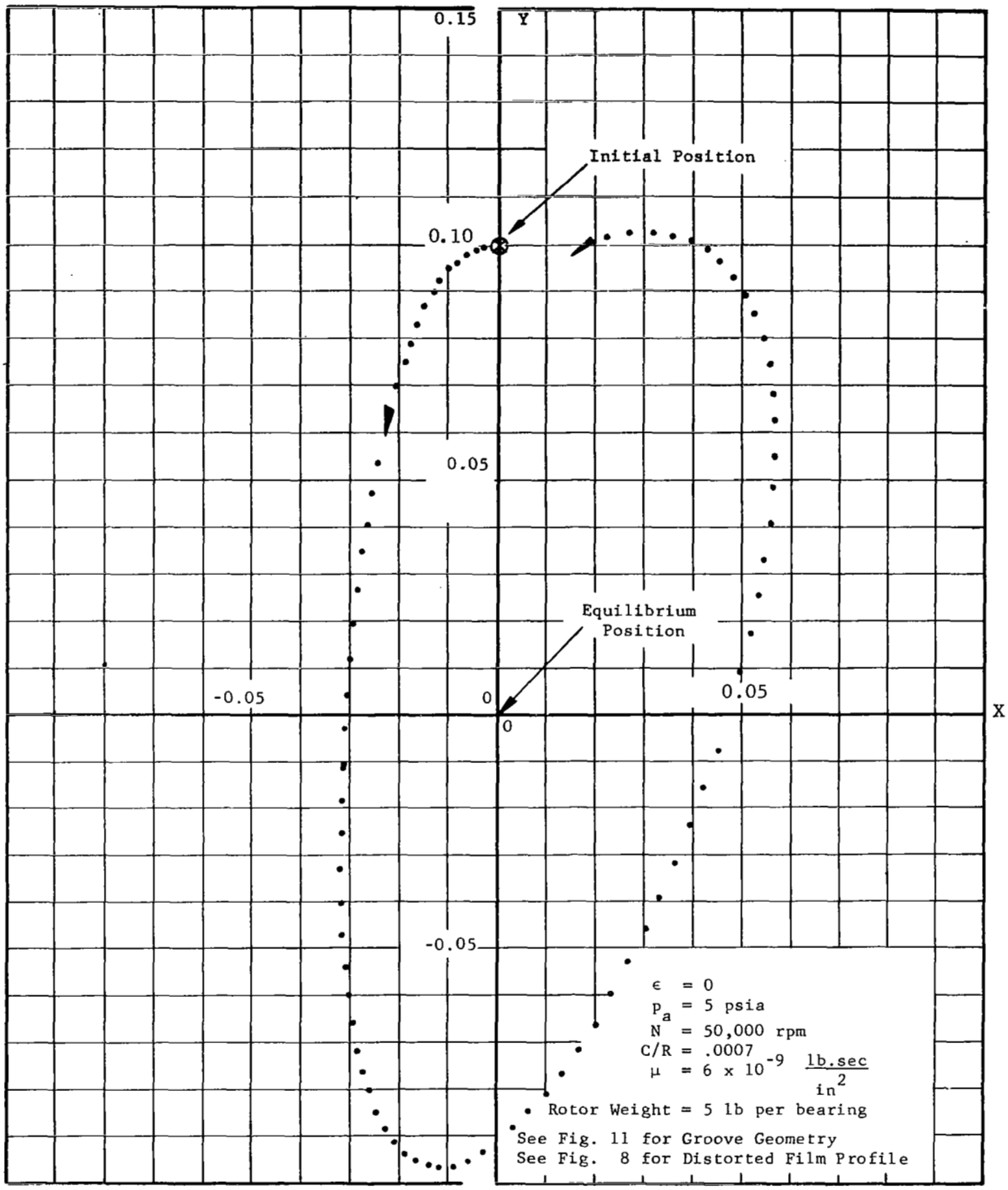

Fig. 5 Trajectory of the Journal Center for Herringbone Journal Bearing under Thermally Distorted Surfaces.

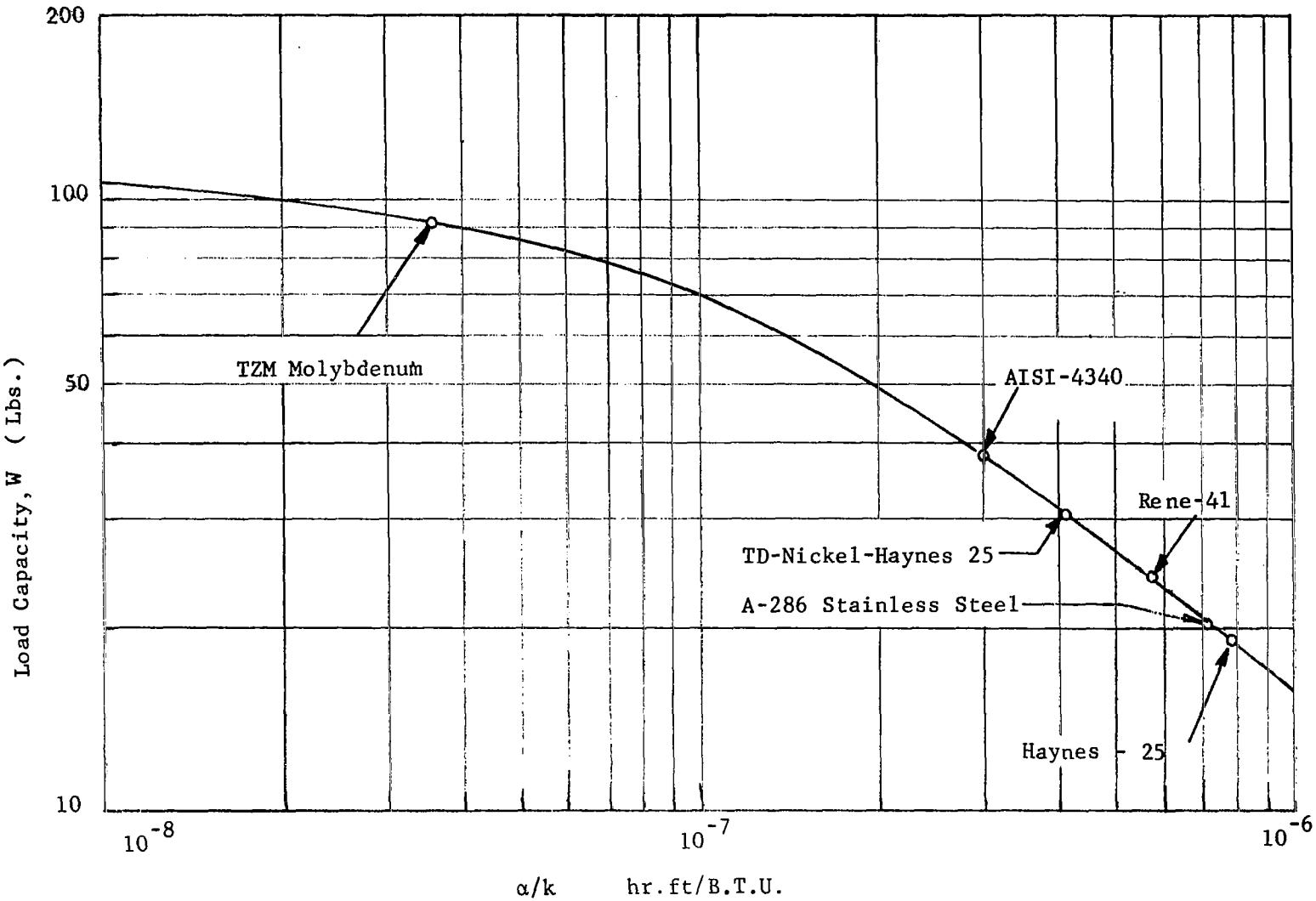

Fig. 6 Effect of α/k on Load Capacity of Spiral Groove Thrust Bearing

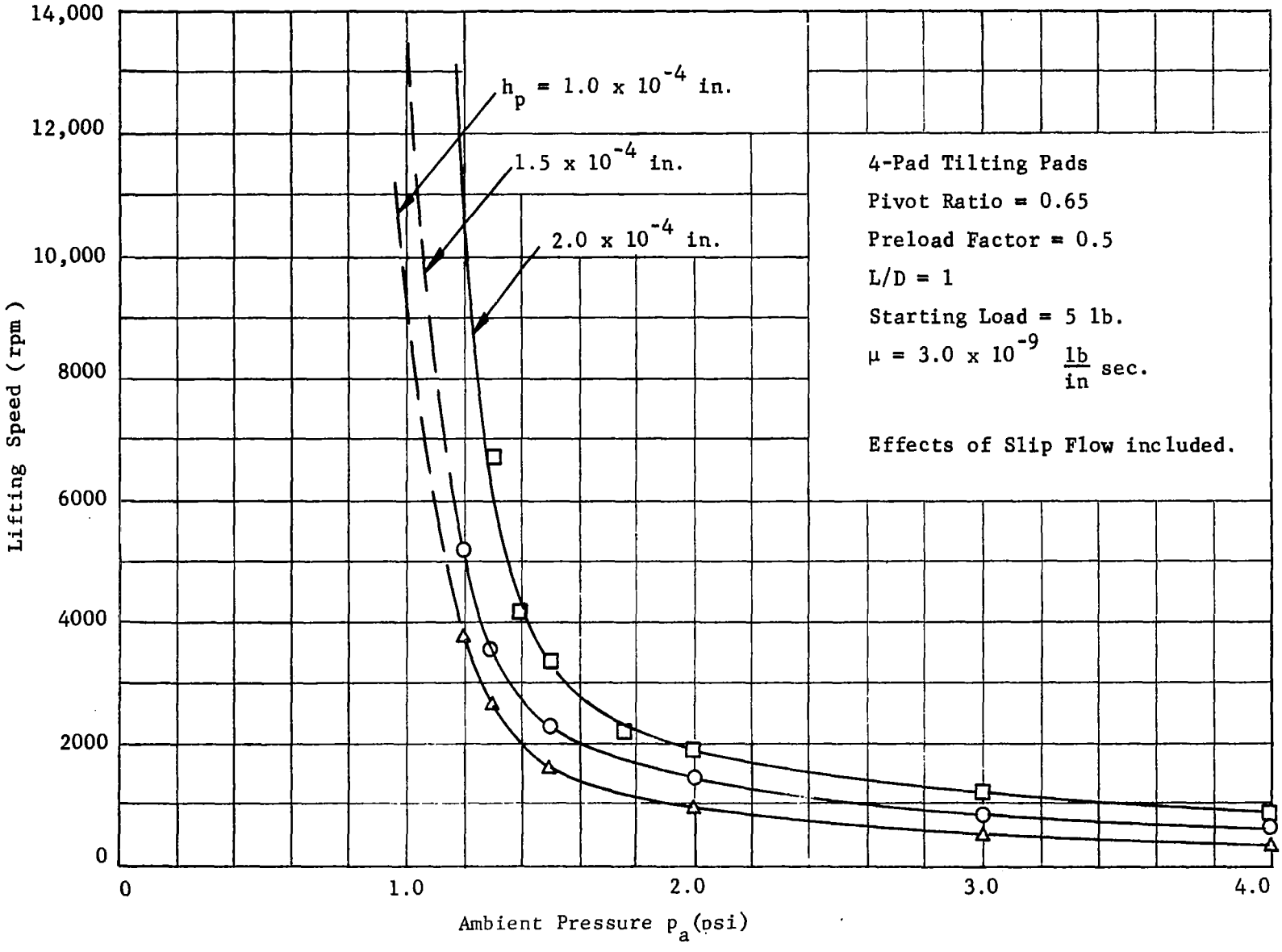

Fig. 7 Lifting Speed vs Ambient Pressure

T_E = Temperature of the enclosure

T_i = Initial ambient temperature

T_c = Temperature of the compressor disc

Speed = 50,000 rpm

Viscosity of the gas = 6×10^{9} lb-sec/in^2

Unit of T = ^{o}F

Unit of H = BTU/hr - ^{o}F - ft^2

Unit of k = BTU/hr - ^{o}F - ft

Unit of ρ = lb/in^3

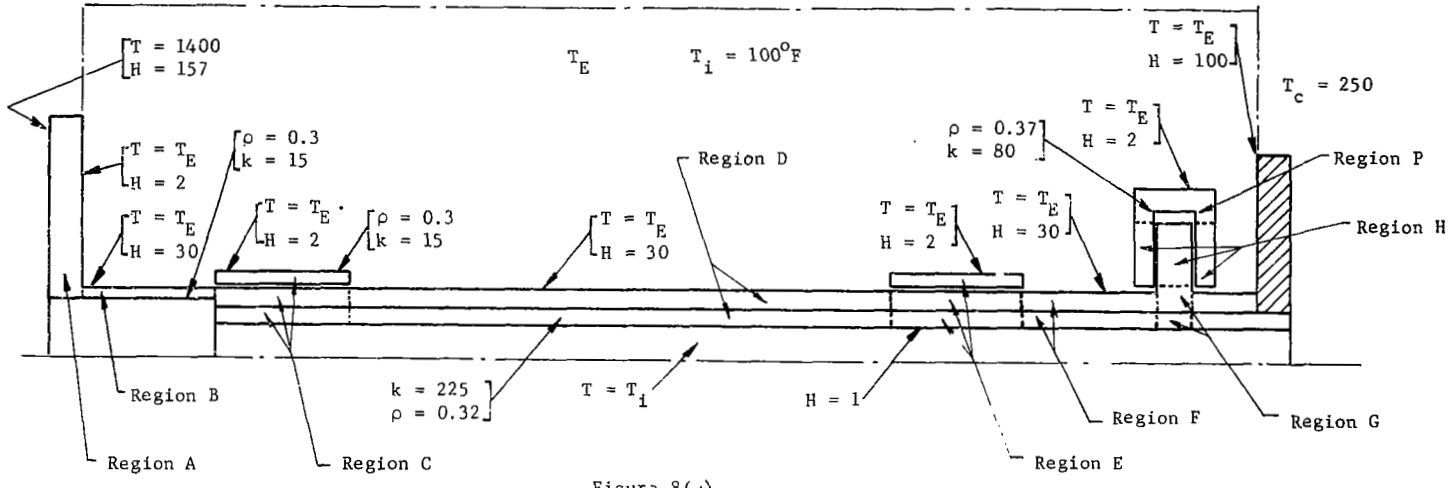

Figure 8(a)

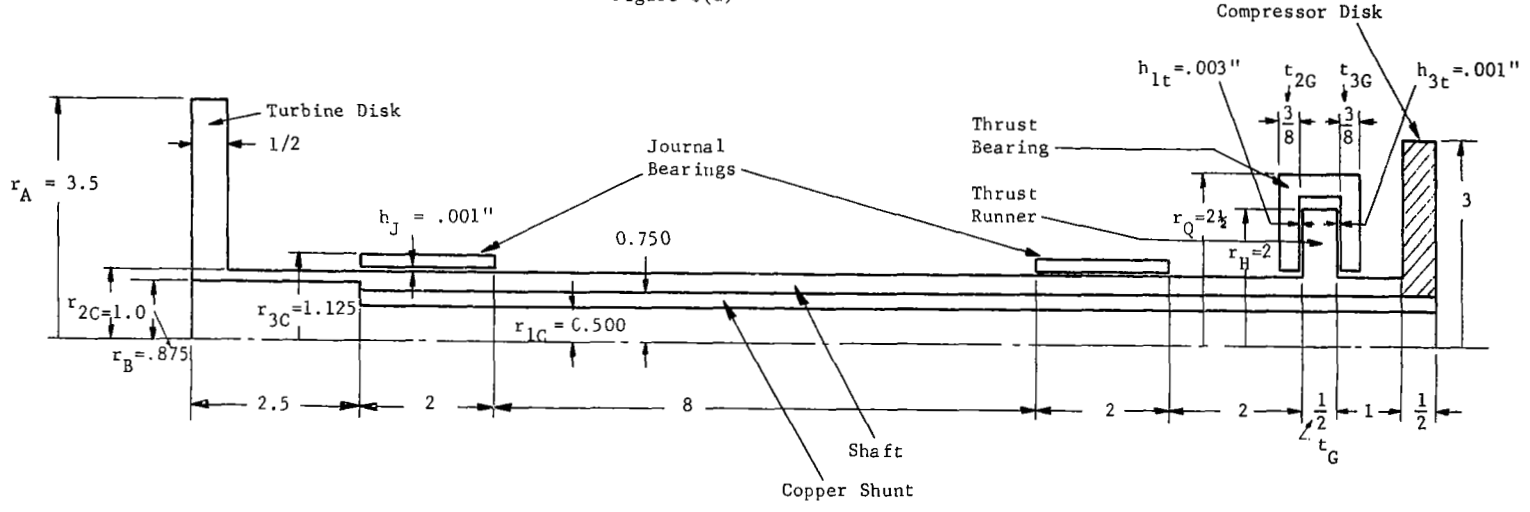

Fig. 8 (b) Dimensions and Thermal Boundary Conditions for Calculating the Transient Temperature of a Typical Turbo-Compressor Model

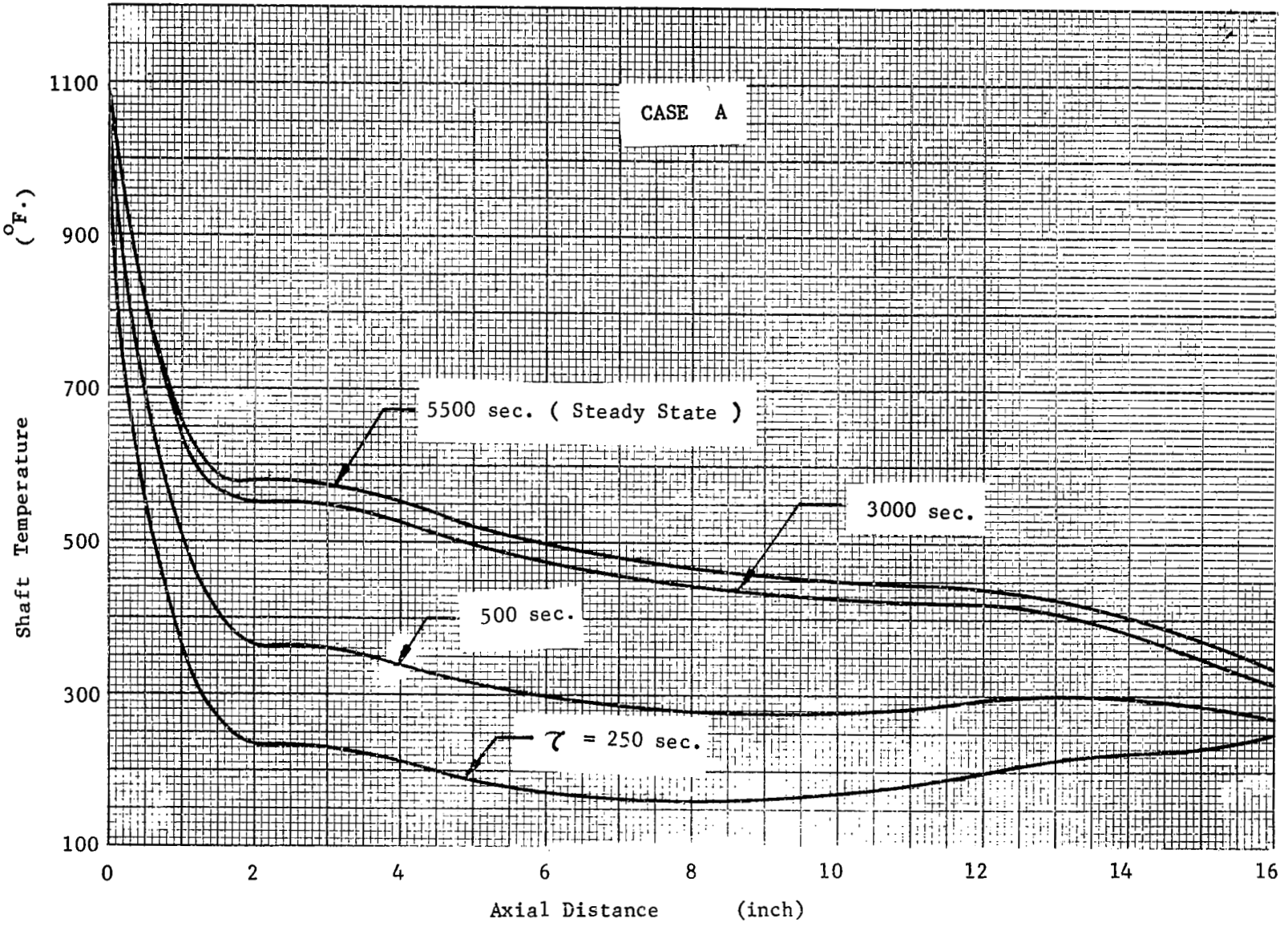

Fig. 9 Transient Temperature Distributions of the Shaft

CASE A

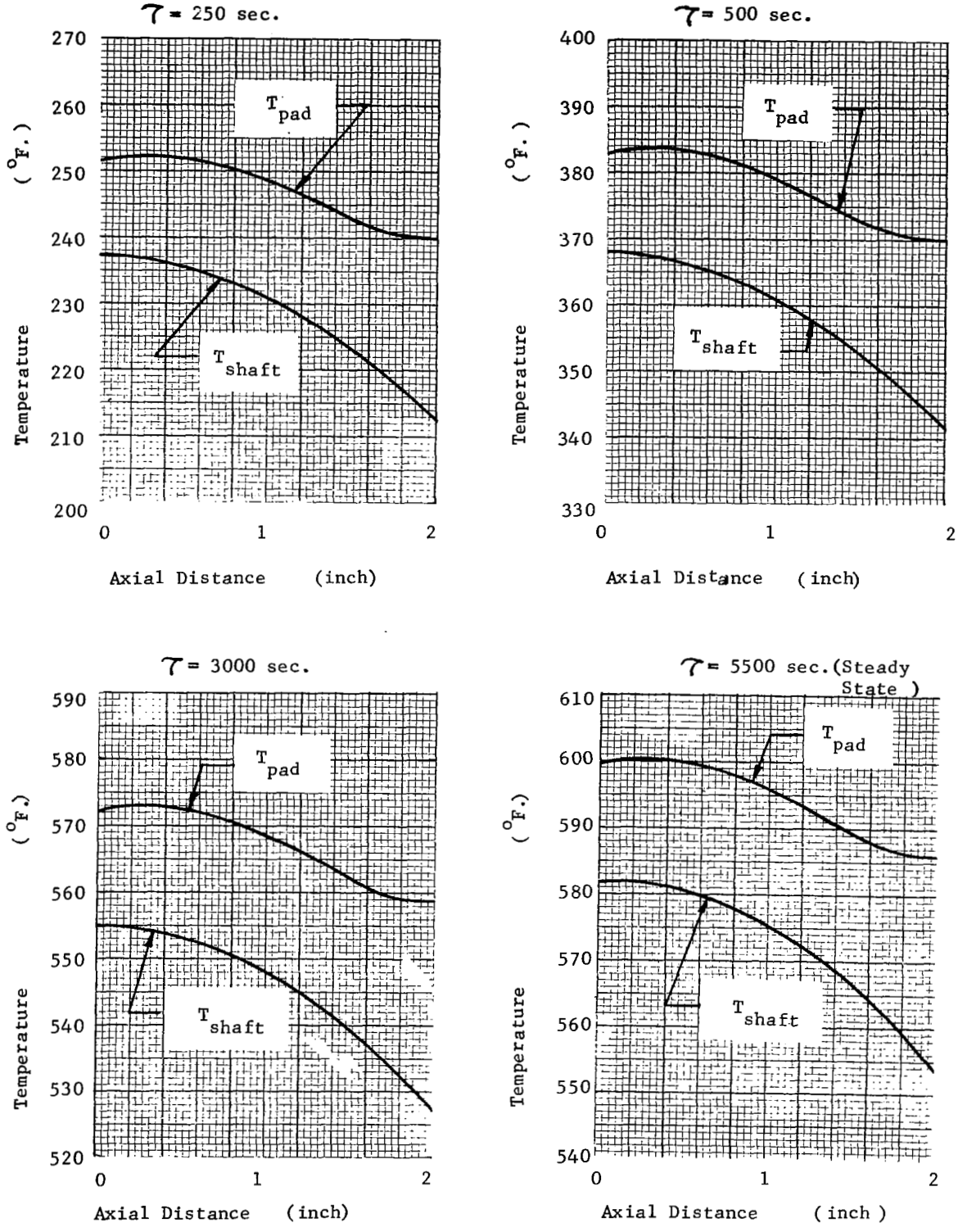

Fig. 10 Axial Temperature Distributions of the Shaft and the Pad, Turbine End

CASE A

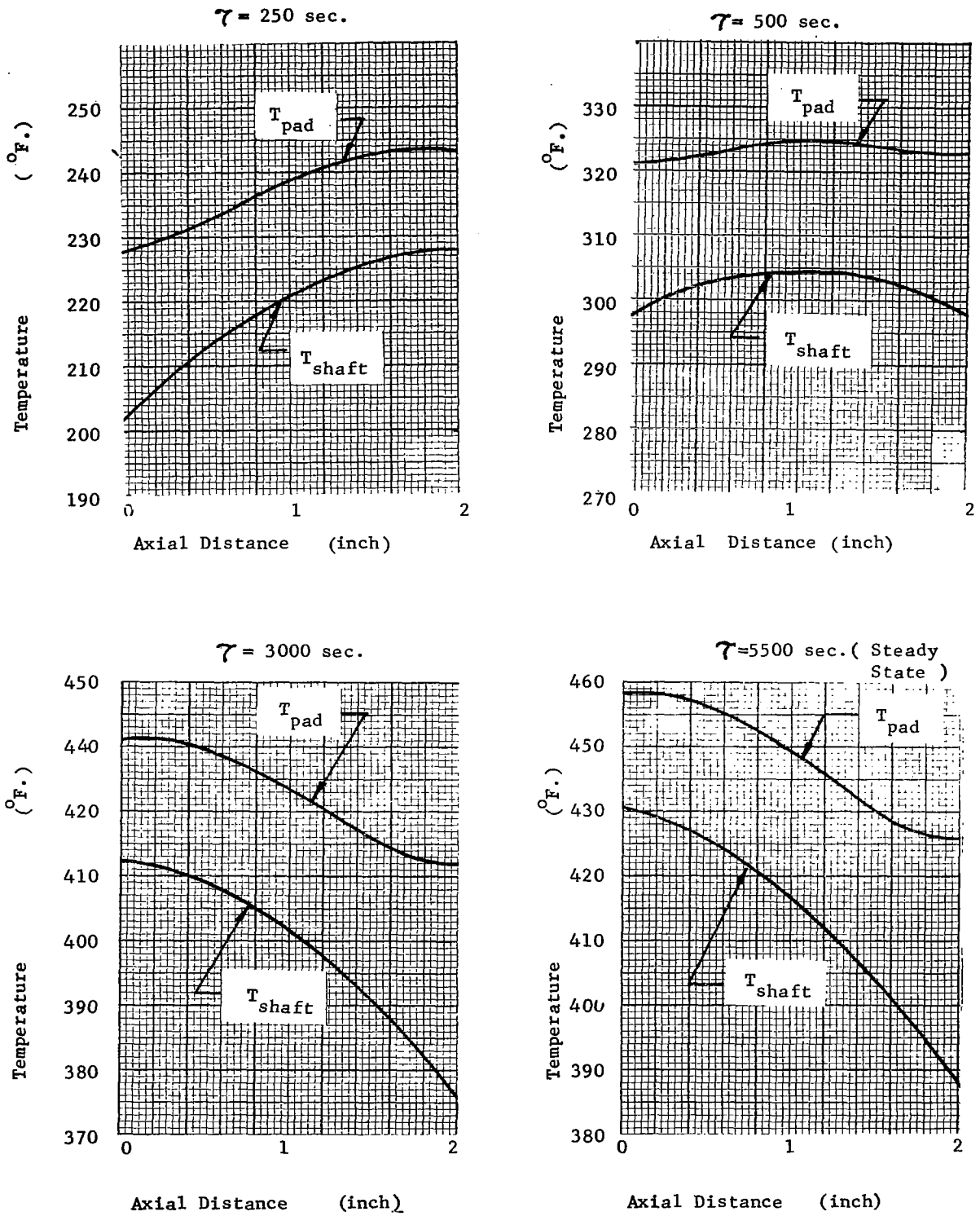

Fig. 11 Axial Temperature Distributions of the Shaft and the Pad, Compressor End

CASE A

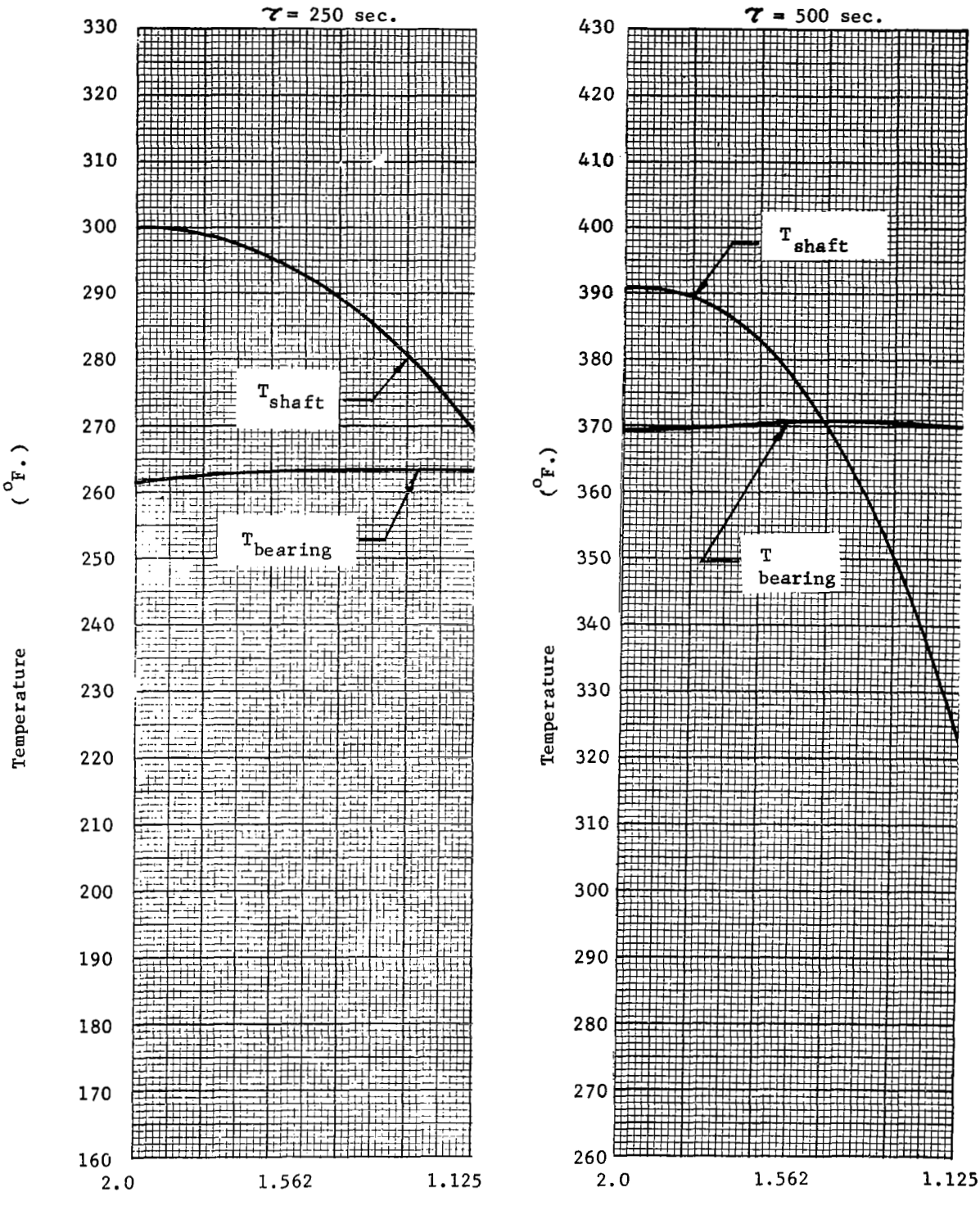

Fig.12 Radial Temperature Distribution of the Shaft and the Thrust Bearing

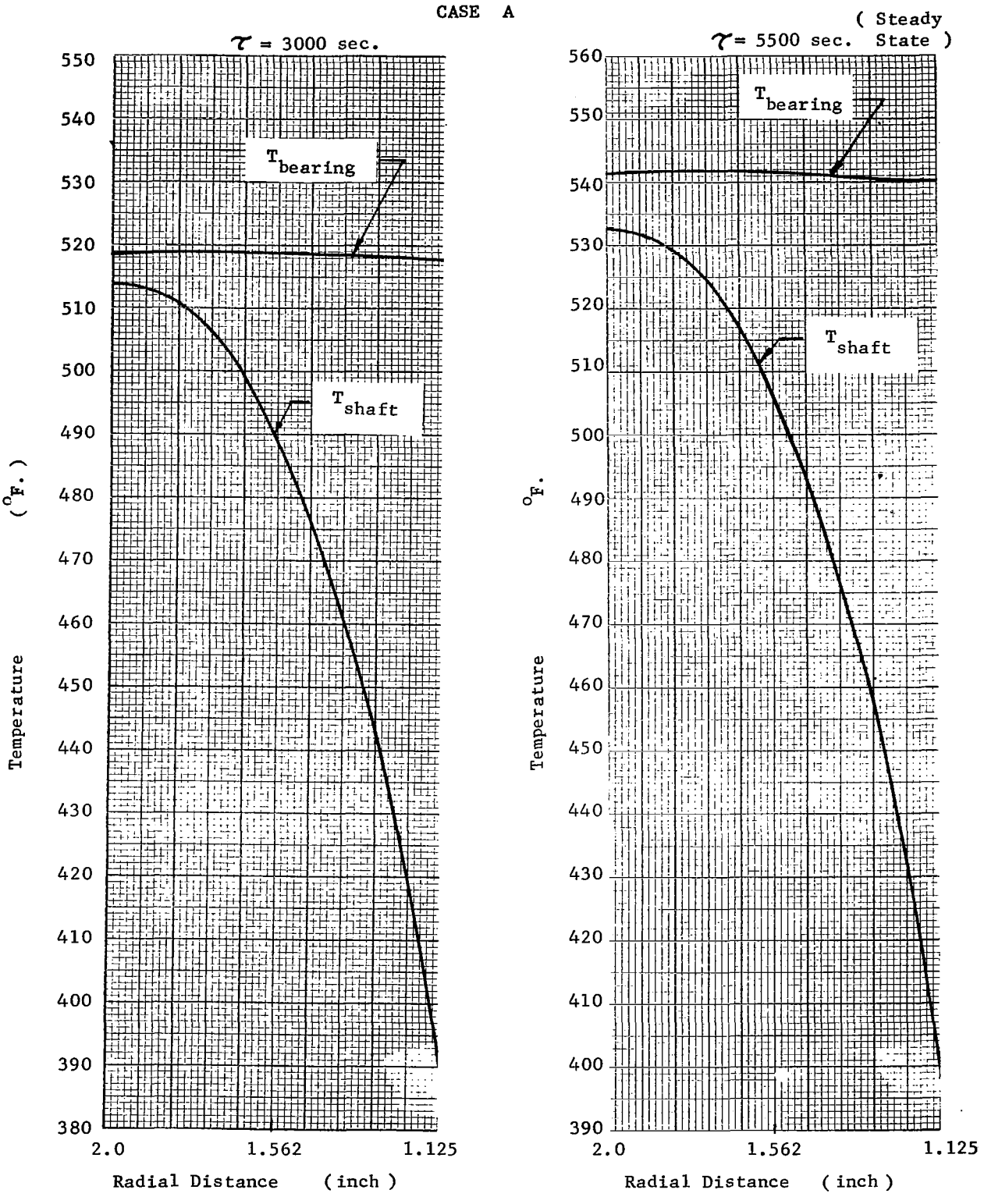

Fig.13 Radial Temperature Distributions of the Shaft and the Thrust Bearing

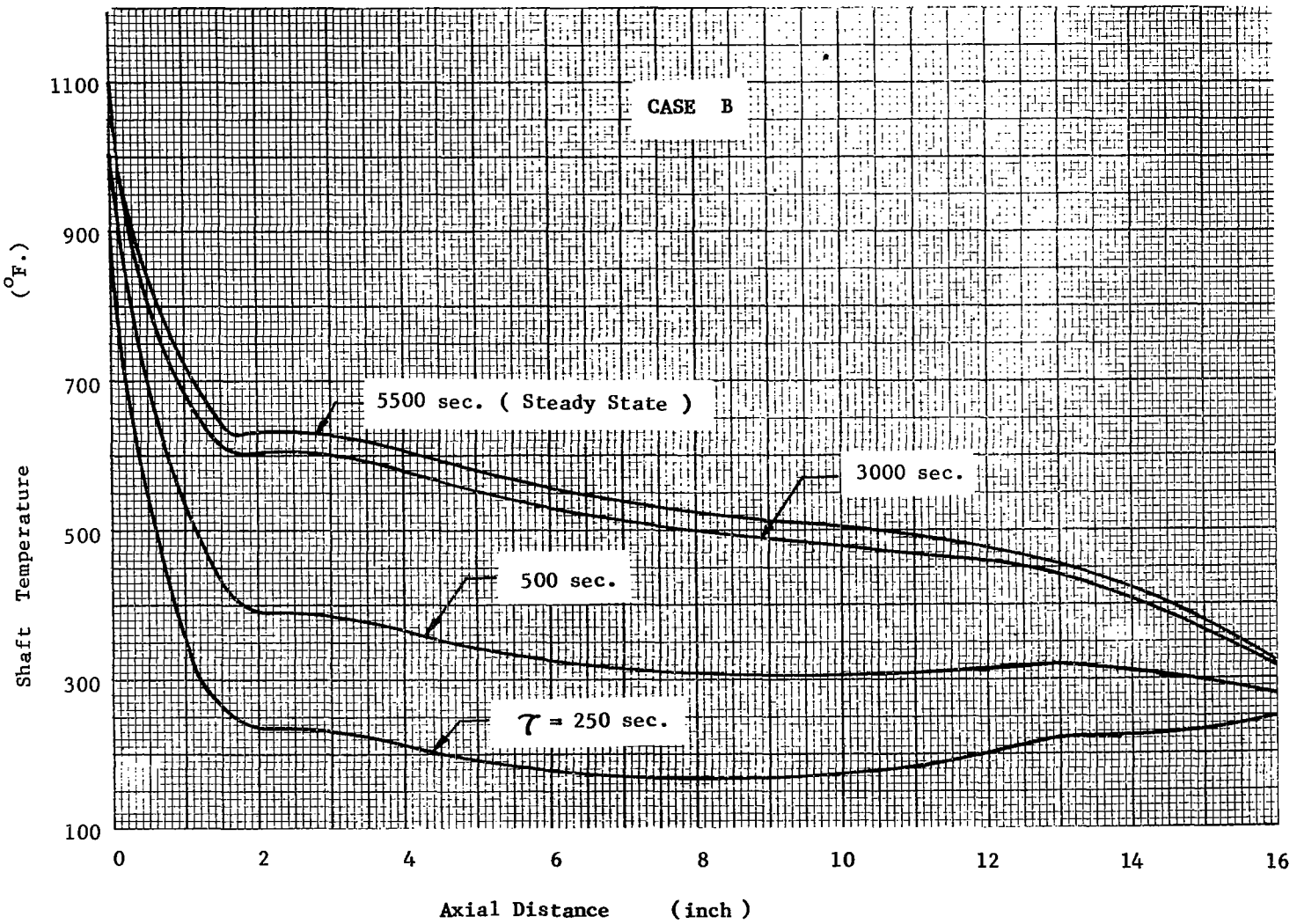

Fig.14 Transient Temperature Distributions of the Shaft

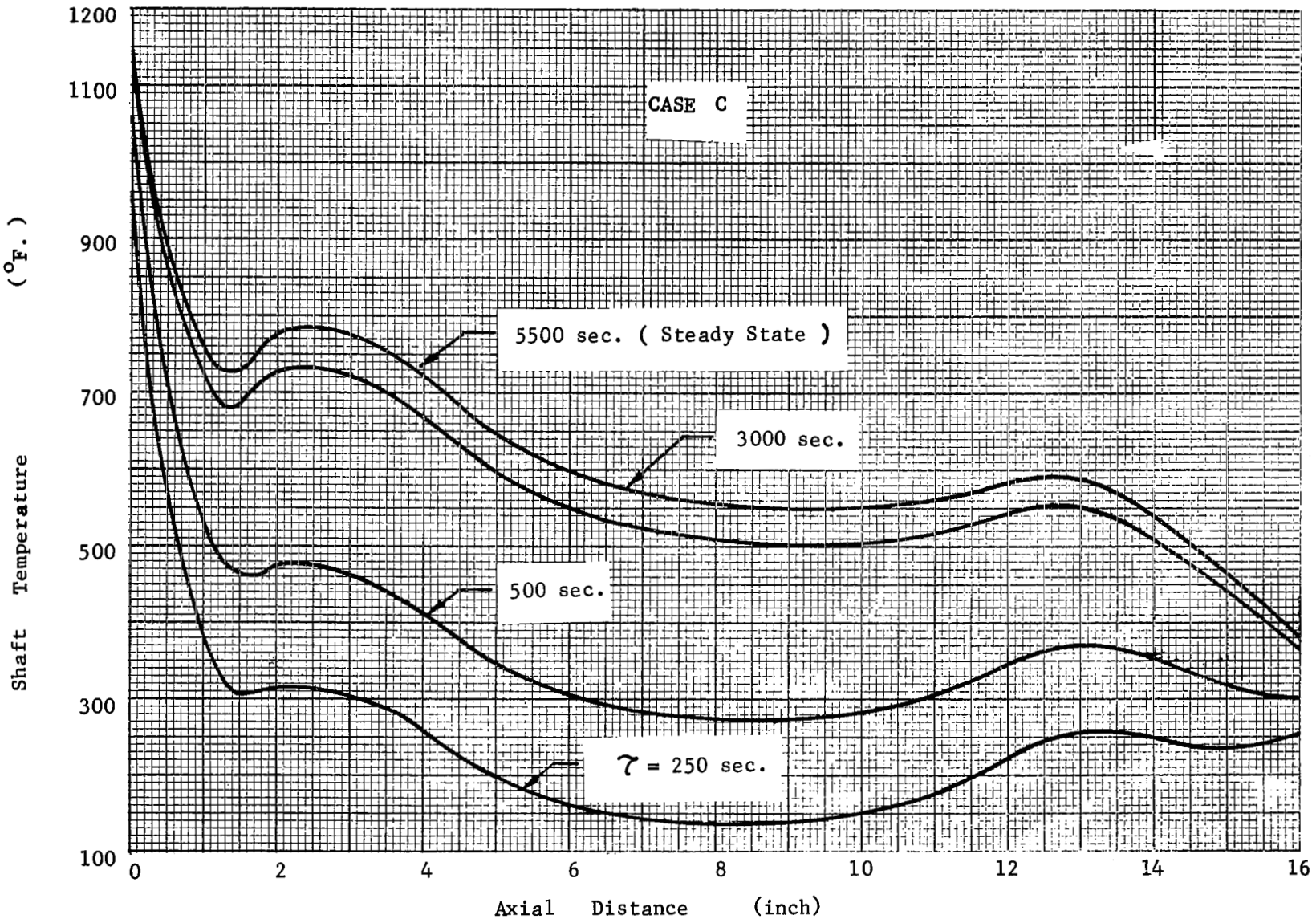

Fig. 15 Transient Temperature Distributions of the Shaft

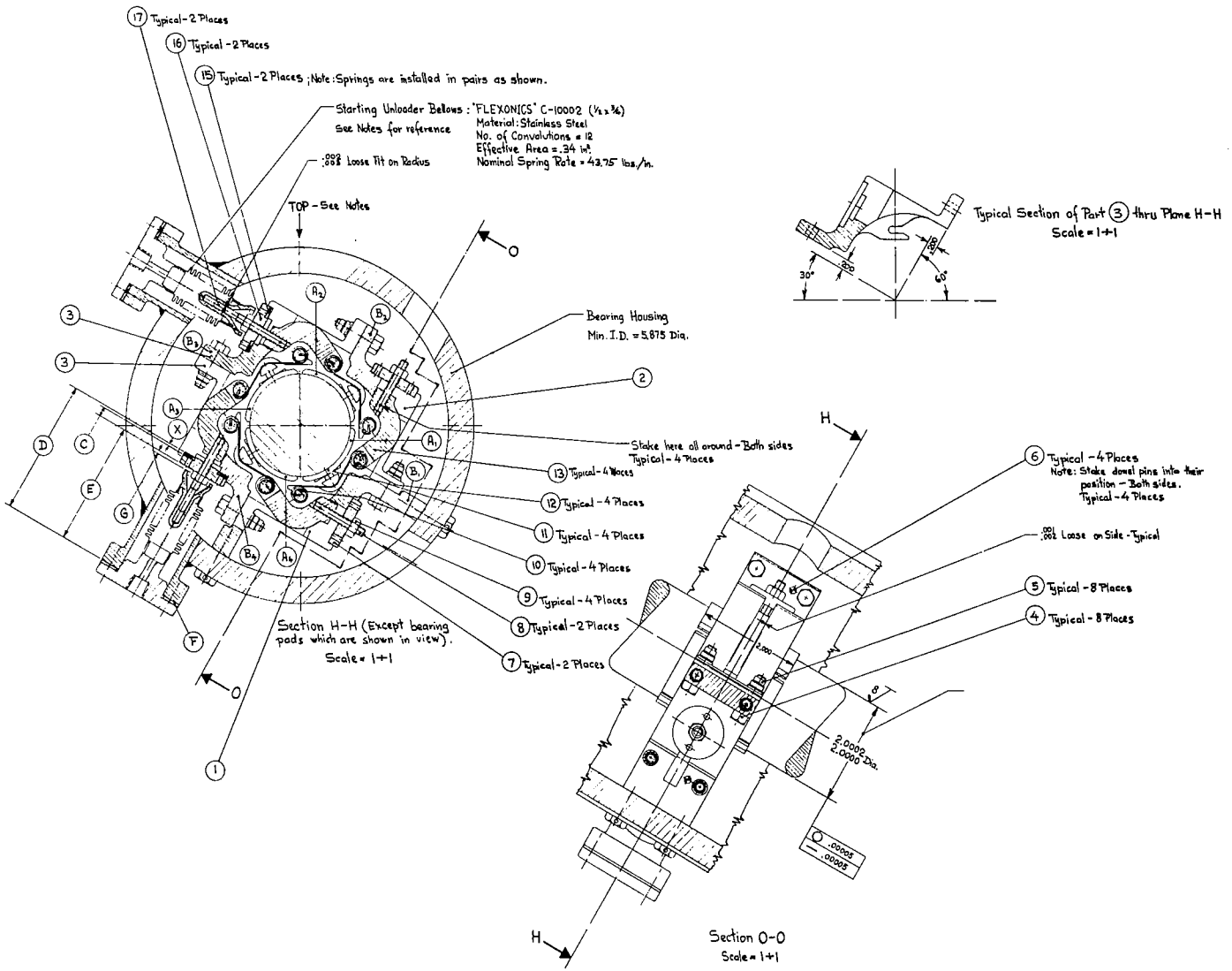

Fig. 16 Detailed Design of the Foil-Supported, Tilting-Pad Journal Bearing

TILTING PADS - CASE A

Load = 20 lb.

Preload = 12 lb.

$\frac{C}{R} = 2.5 \times 10^{-3}$ in. (at 0 RPM)

$p_a = 15$ psia

$\mu = 6.0 \times 10^{-9}$ lb-sec/$_{in}^2$

$\frac{L}{D} = 1.0$

$\frac{t}{D} = 0.05$

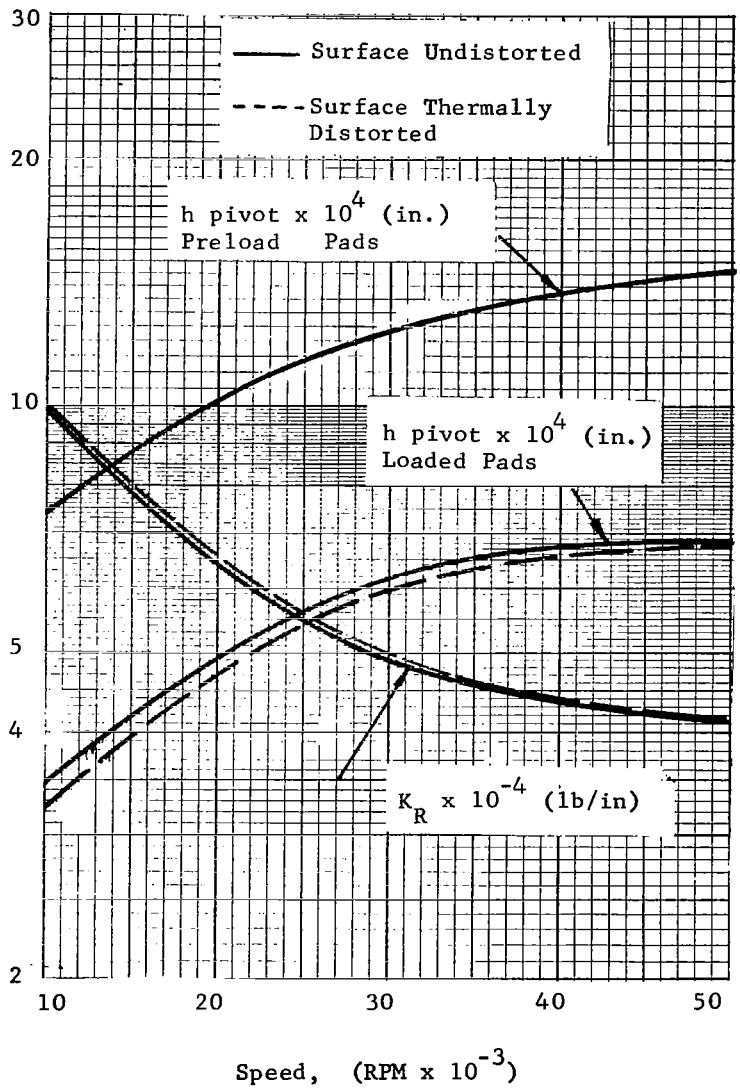

Fig. 17 Performance of Tilting Pad Journal Bearing, Case A

TILTING PADS - CASE A

Load = 20 lb.

Preload = 12 lb.

$\frac{C}{R} = 2.5 \times 10^{-3}$ in. (at 0 RPM)

$p_a = 15$ psia

$\mu = 6.0 \times 10^{-9}$ lb-sec/$_{in}^2$

$\frac{L}{D} = 1.0$

$\frac{t}{D} = 0.05$

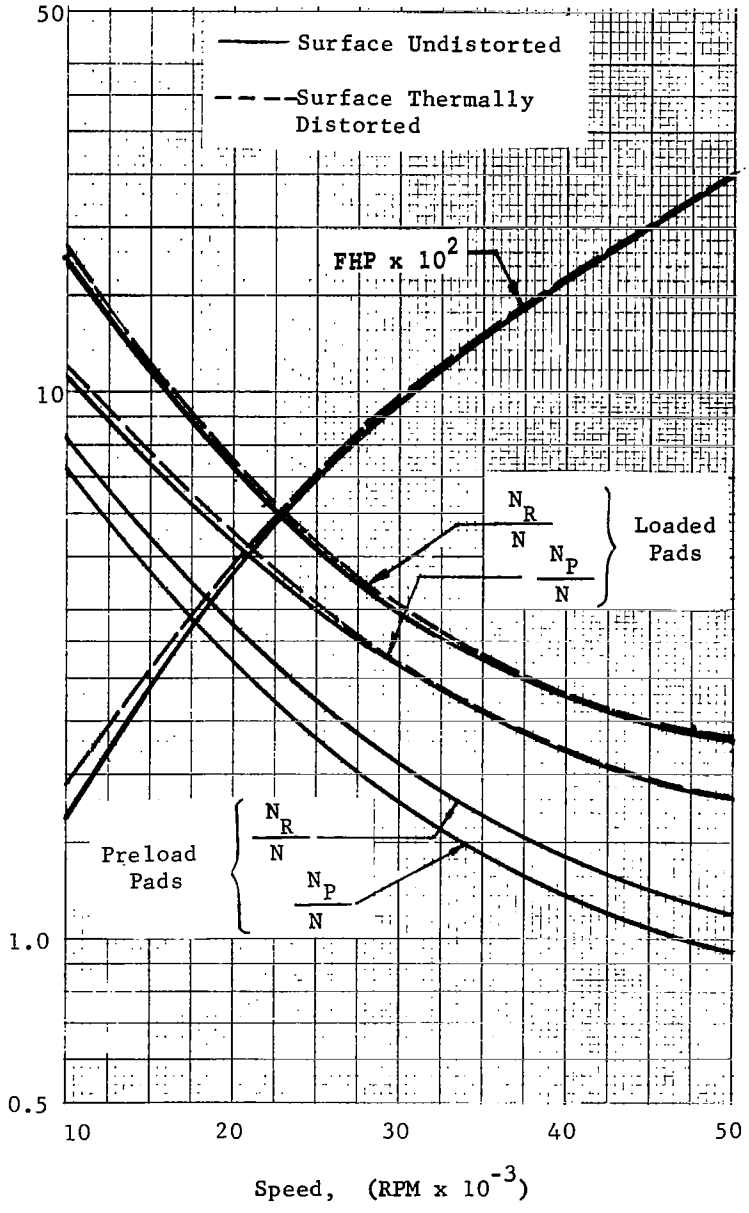

Fig. 18 Performance of Tilting Pad Journal Bearing, Case A

TILTING PADS - CASE C

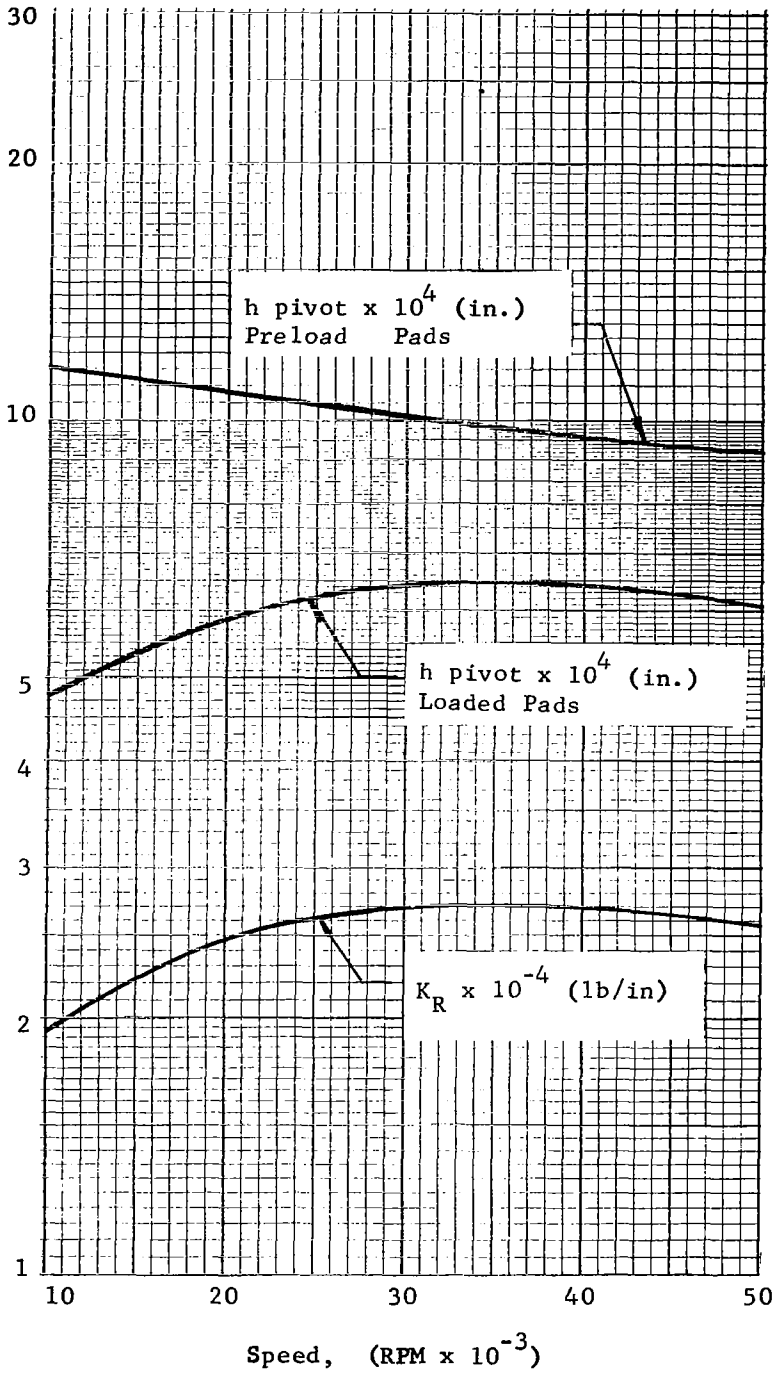

Load = 20 lb.

Preload = 12 lb.

$\frac{C}{R}$ = 2.5 x 10^{-3} in. (at 0 RPM)

p_a = 5 psia

μ = 6.0 x 10^{-9} lb-sec/$_{in^2}$

$\frac{L}{D}$ = 1.0

$\frac{t}{D}$ = 0.05

Fig. 21 Performance of Tilting Pad Journal Bearing, Case C

TILTING PADS - CASE B

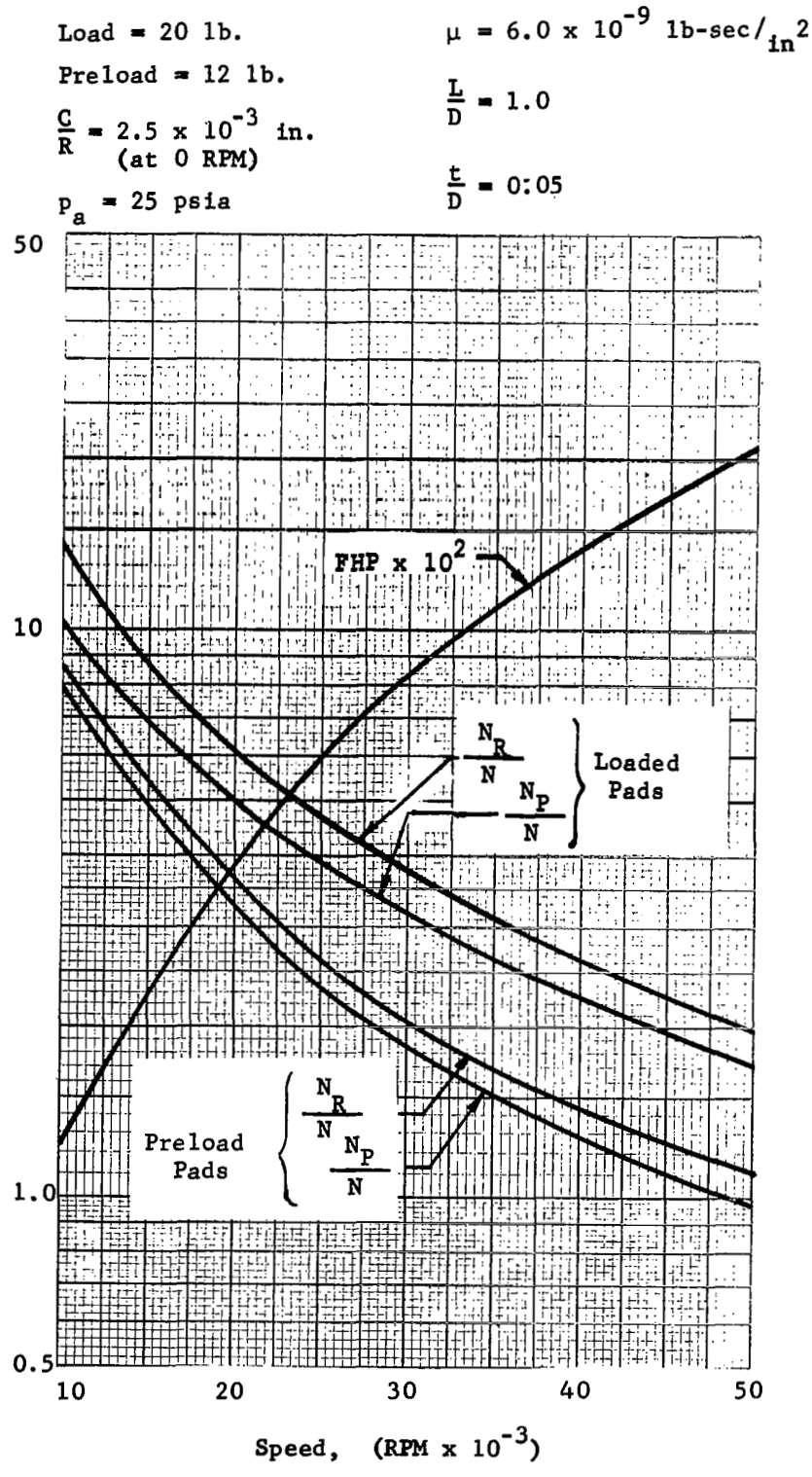

Fig. 20 Performance of Tilting Pad Journal Bearing, Case B

TILTING PADS - CASE C

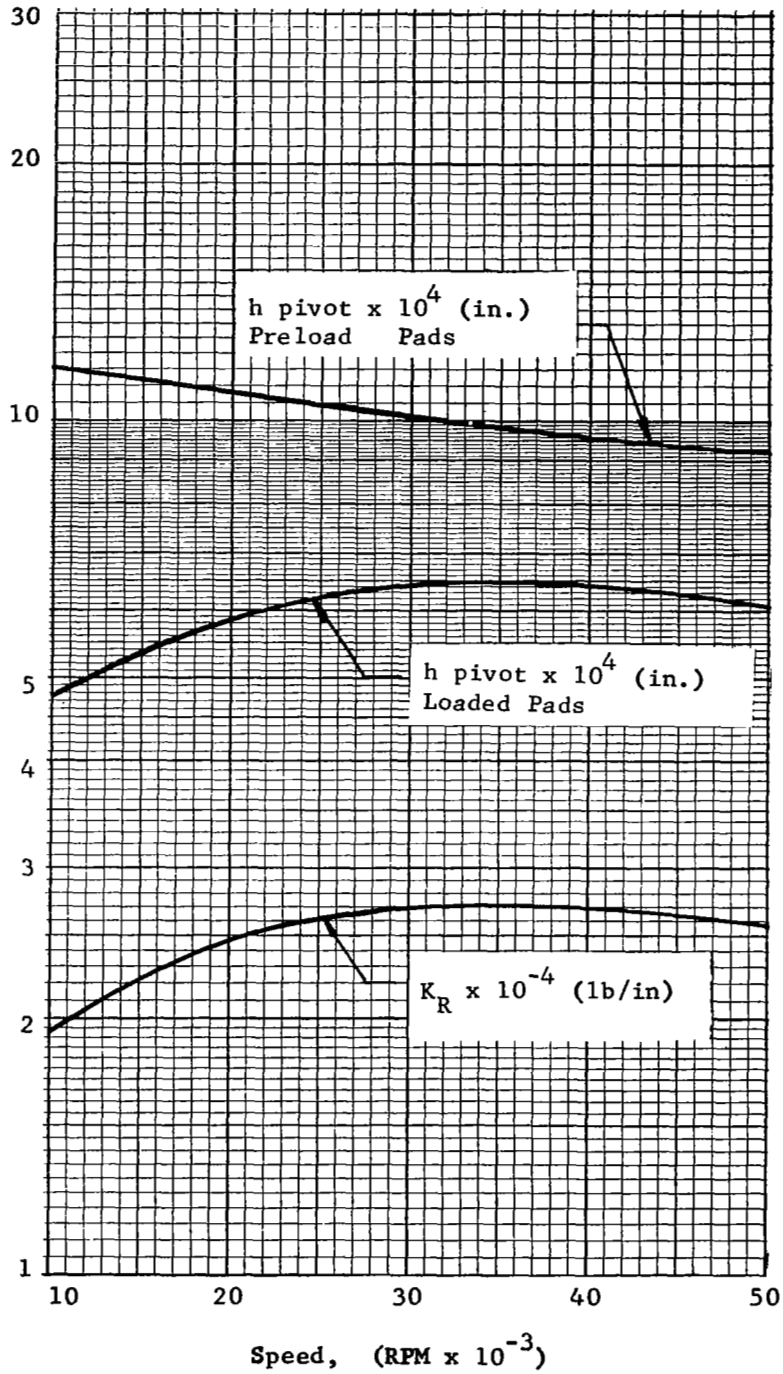

Load = 20 lb.

Preload = 12 lb.

$\frac{C}{R}$ = 2.5 x 10^{-3} in. (at 0 RPM)

p_a = 5 psia

μ = 6.0 x 10^{-9} lb-sec/$_{in}^2$

$\frac{L}{D}$ = 1.0

$\frac{t}{D}$ = 0.05

Fig. 21 Performance of Tilting Pad Journal Bearing, Case C

TILTING PADS - CASE C

Load = 20 lb.

Preload = 12 lb.

$\frac{C}{R} = 2.5 \times 10^{-3}$ in. (at 0 RPM)

$p_a = 5$ psia

$\mu = 6.0 \times 10^{-9}$ lb.-sec/$_{in}^2$

$\frac{L}{D} = 1.0$

$\frac{t}{D} = 0.05$

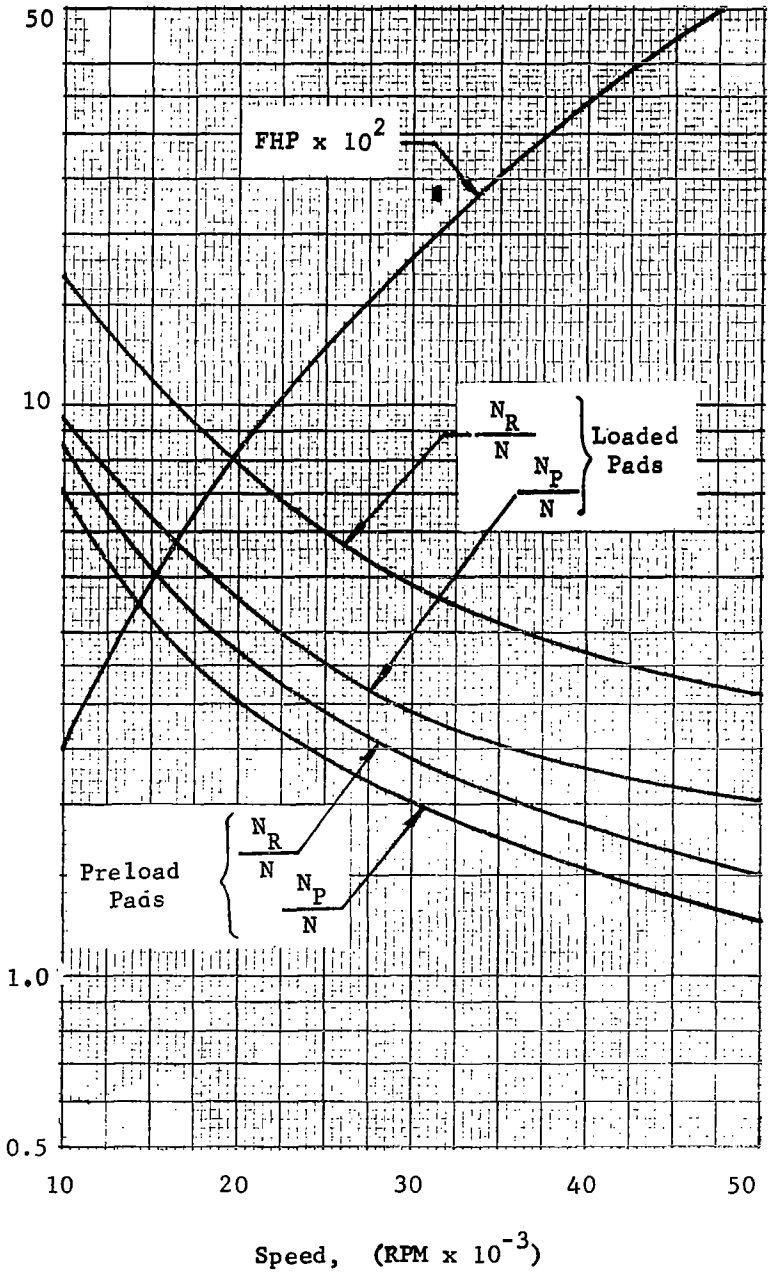

Fig. 22 Performance of Tilting Pad Journal Bearing, Case C

TILTING PADS - CASE D

Load = 10 lb.

Preload = 12 lb.

$\frac{C}{R}$ = 2.5×10^{-3} in. (at 0 RPM)

p_a = 15 psia

$\mu = 6.0 \times 10^{-9}$ lb-sec/in^2

$\frac{L}{D} = 1.0$

$\frac{t}{D} = 0.05$

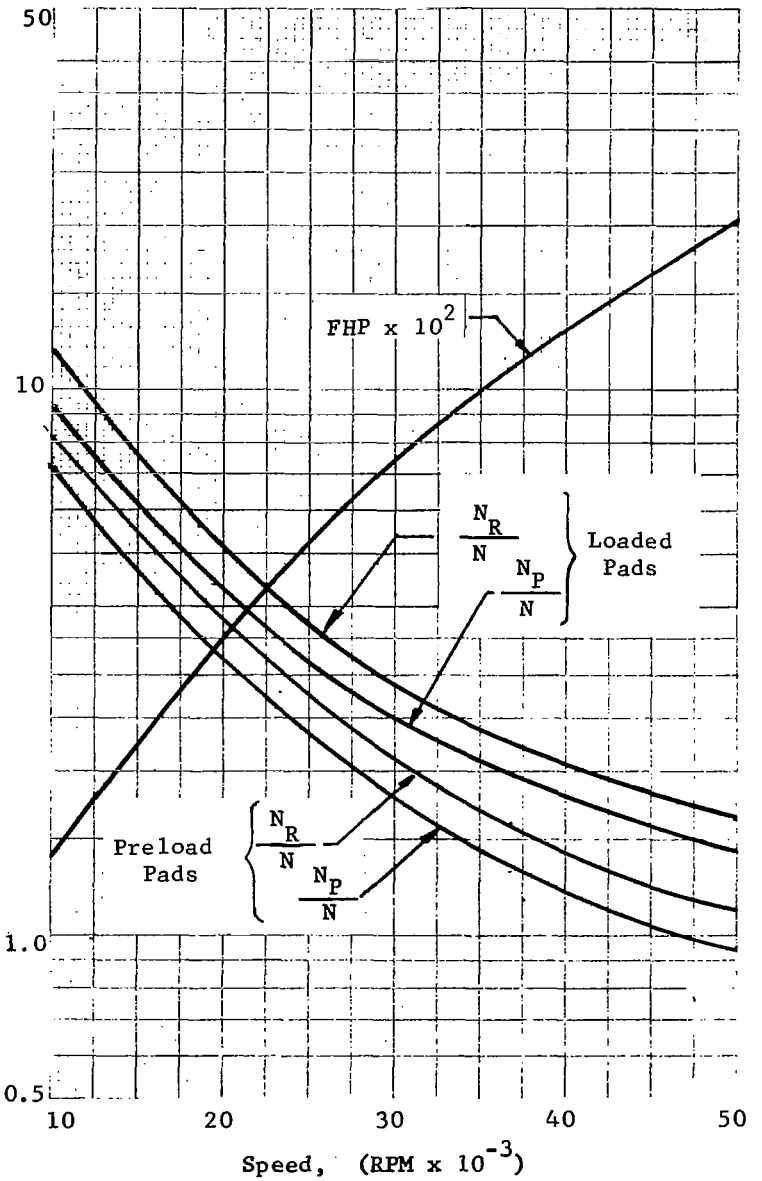

Fig. 23 Performance of Tilting Pad Journal Bearing, Case D

TILTING PADS - CASE D

Load = 10 lb.

Preload = 12 lb.

$\frac{C}{R} = 2.5 \times 10^{-3}$ in.
(at 0 RPM)

$p_a = 15$ psia

$\mu = 6.0 \times 10^{-9}$ lb-sec/$_{in}^2$

$\frac{L}{D} = 1.0$

$\frac{t}{D} = 0.05$

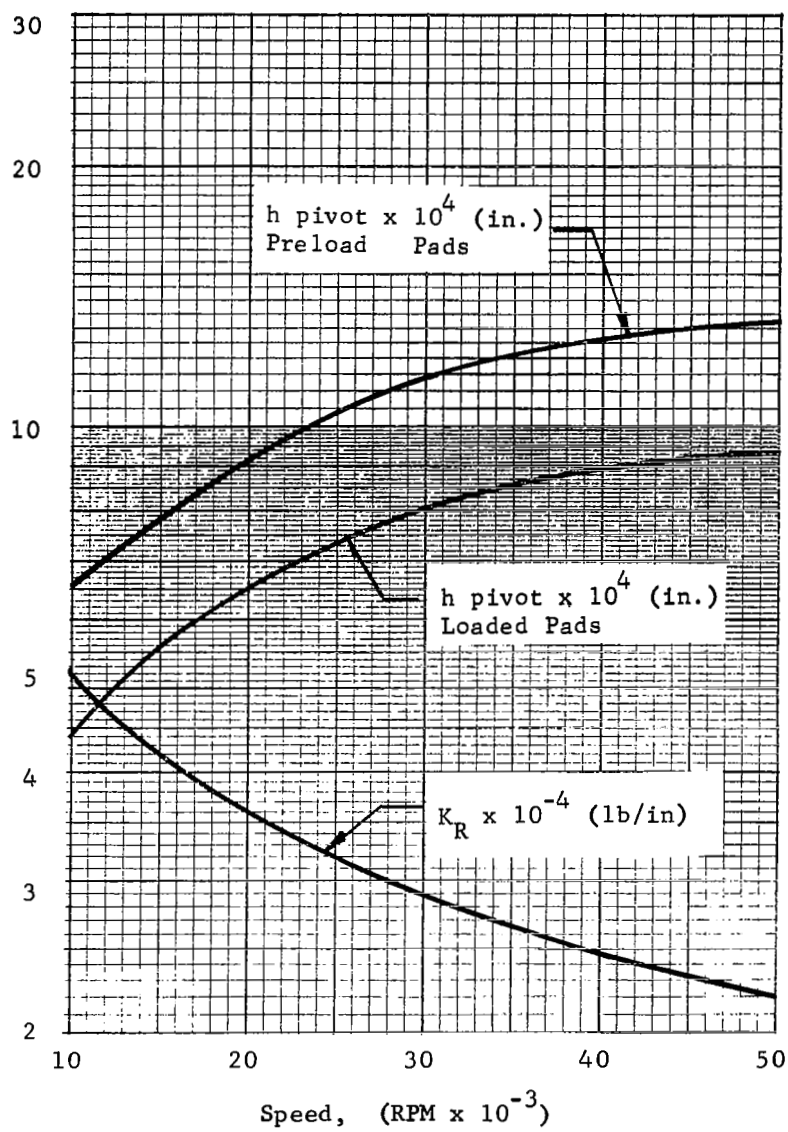

Fig. 24 Performance of Tilting Pad Journal Bearing, Case D

TILTING PADS - CASE E

Load = 10 lb.

Preload = 12 lb.

$\frac{C}{R} = 2.5 \times 10^{-3}$ in. (at 0 RPM)

$p_a = 25$ psia

$\mu = 6.0 \times 10^{-9}$ lb-sec/$_{in}^2$

$\frac{L}{D} = 1.0$

$\frac{t}{D} = 0.05$

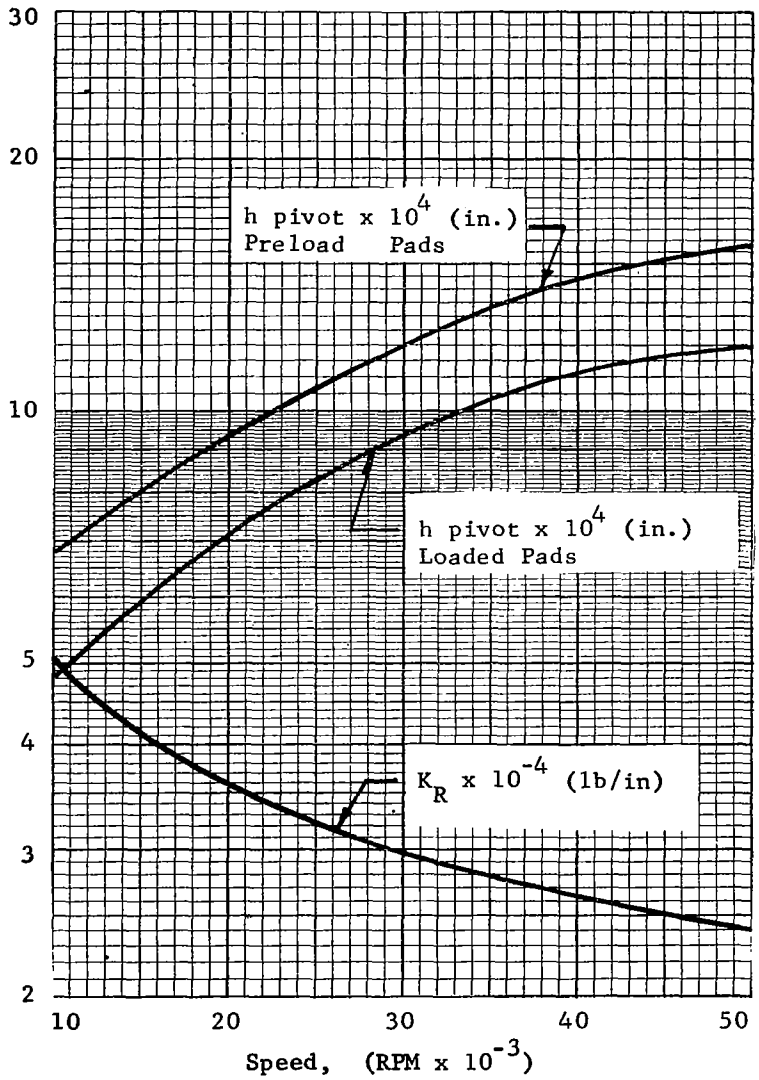

Fig. 25 Performance of Tilting Pad Journal Bearing, Case E

TILTING PADS - CASE E

Load = 10 lb.

Preload = 12 lb.

$\frac{C}{R} = 2.5 \times 10^{-3}$ in. (at 0 RPM)

p_a = 25 psia

$\mu = 6.0 \times 10^{-9}$ lb-sec/in^2

$\frac{L}{D} = 1.0$

$\frac{t}{D} = 0.05$

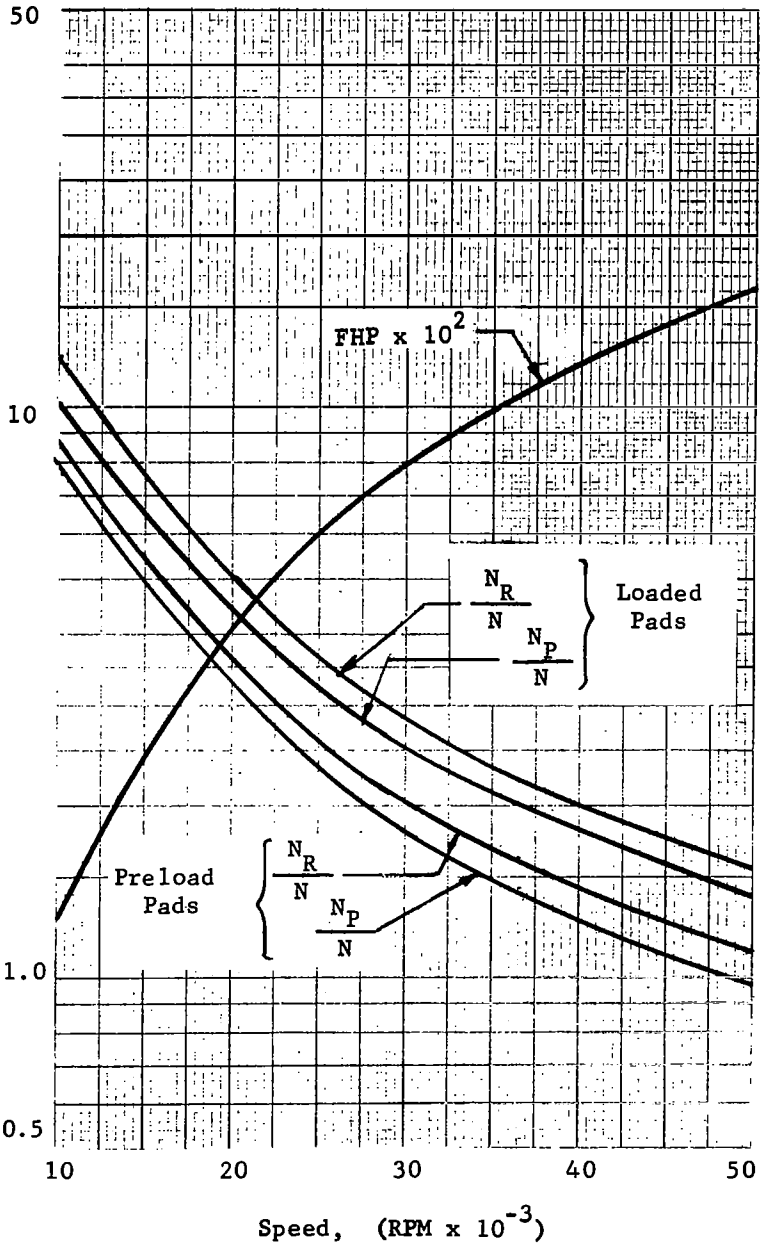

Fig. 26 Performance of Tilting Pad Journal Bearing, Case E

TILTING PADS - CASE F

Load = 10 lb.

Preload = 0 lb.

$\frac{C}{R}$ = 2.5×10^{-3} in. (at 0 rpm)

P_a = 15 psia

μ = 6.0×10^{-9} lb-sec/in^2

$\frac{L}{D}$ = 1.0

$\frac{t}{D}$ = 0.05

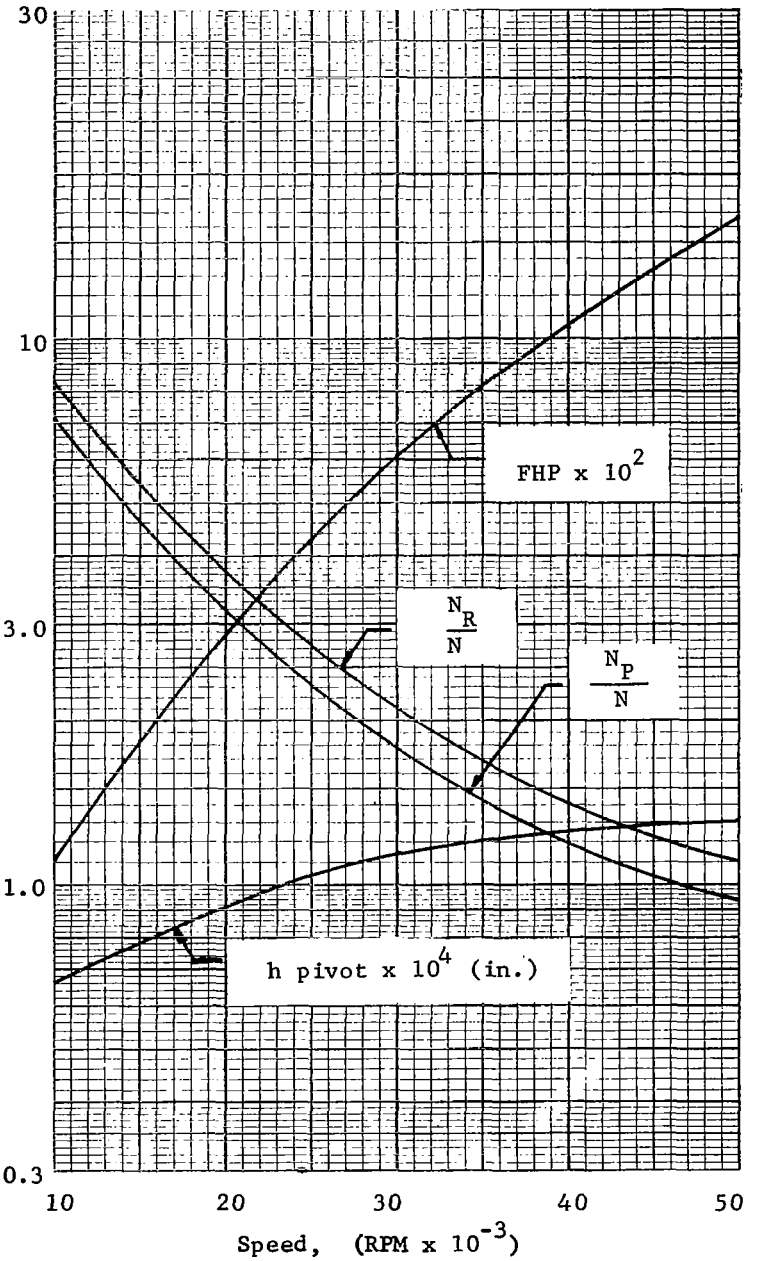

Fig. 27 Performance of Tilting Pad Journal Bearing, Case F

TILTING PADS - CASE H

Load = 20 lb.

Preload = 12 lb.

$\frac{C}{R} = 1.5 \times 10^{-3}$ in. (at 0 RPM)

$p_a = 15$ psia

$\mu = 6.0 \times 10^{-9}$ lb-sec/$_{in}^2$

$\frac{L}{D} = 1.0$

$\frac{t}{D} = 0.05$

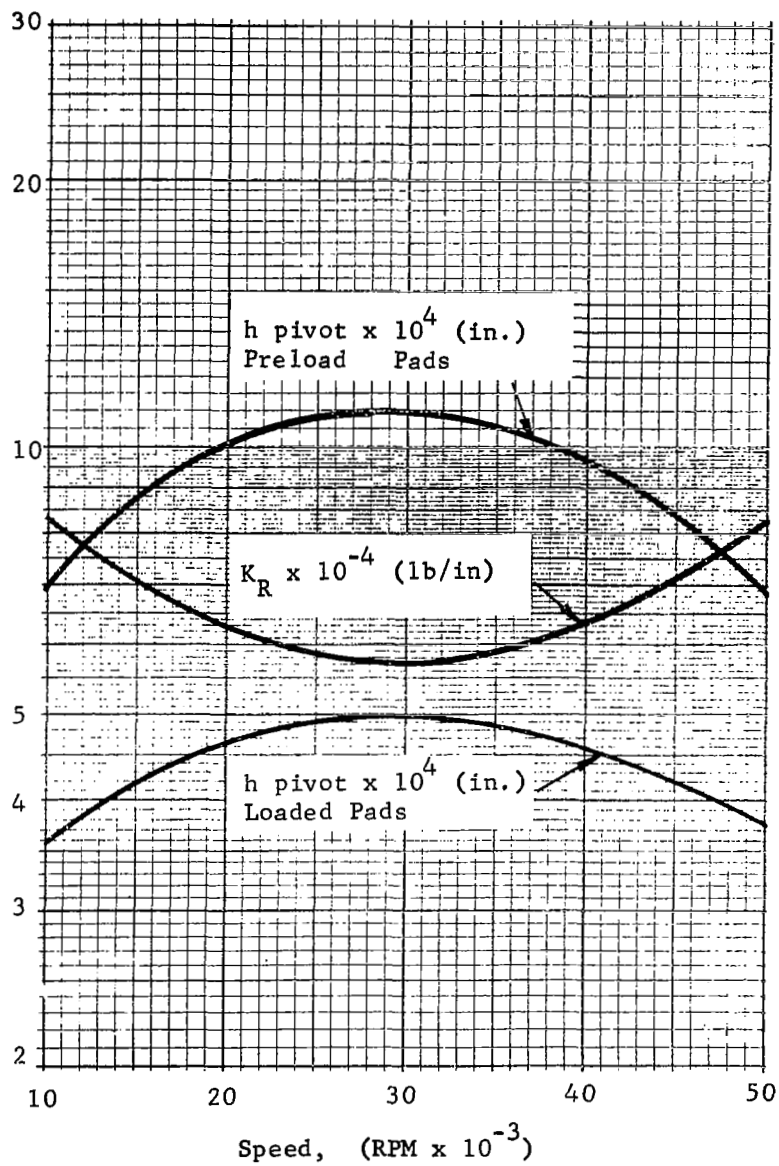

Fig. 30 Performance of Tilting Pad Journal Bearing, Case H

TILTING PADS - CASE H

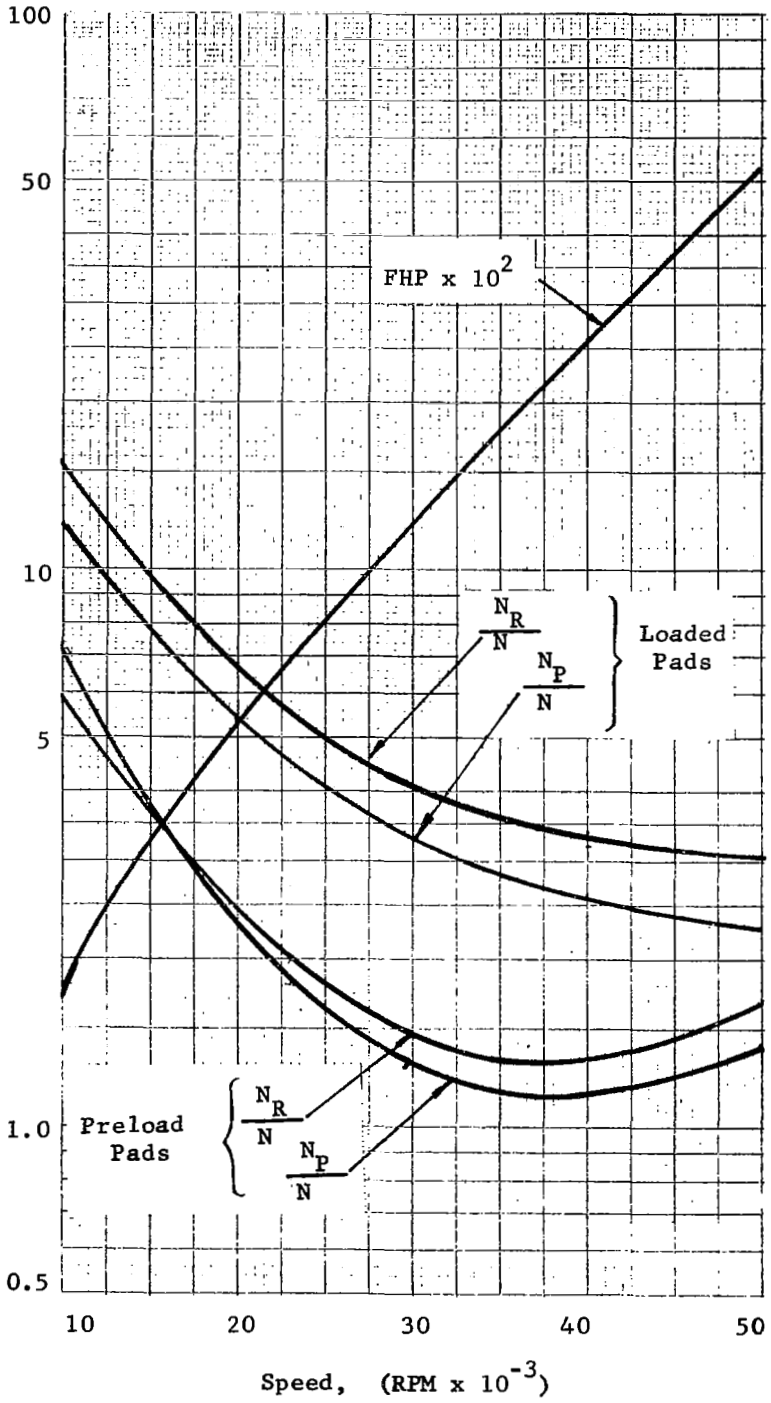

Load = 20 lb.

Preload = 12 lb.

$\frac{C}{R}$ = 1.5 x 10^{-3} in.
(at 0 RPM)

p_a = 15 psia

μ = 6.0 x 10^{-9} lb-sec/$_{in}^2$

$\frac{L}{D}$ = 1.0

$\frac{t}{D}$ = 0.05

Fig. 31 Performance of Tilting Pad Journal Bearing, Case H

TILTING PADS - CASE I

Load = 20 lb.

Preload = 20 lb.

$\frac{C}{R}$ = 3.5×10^{-3} in. (at 0 RPM)

P_a = 15 psia

μ = 6.0×10^{-9} lb-sec/in^2

$\frac{L}{D}$ = 1.0

$\frac{t}{D}$ = 0.05

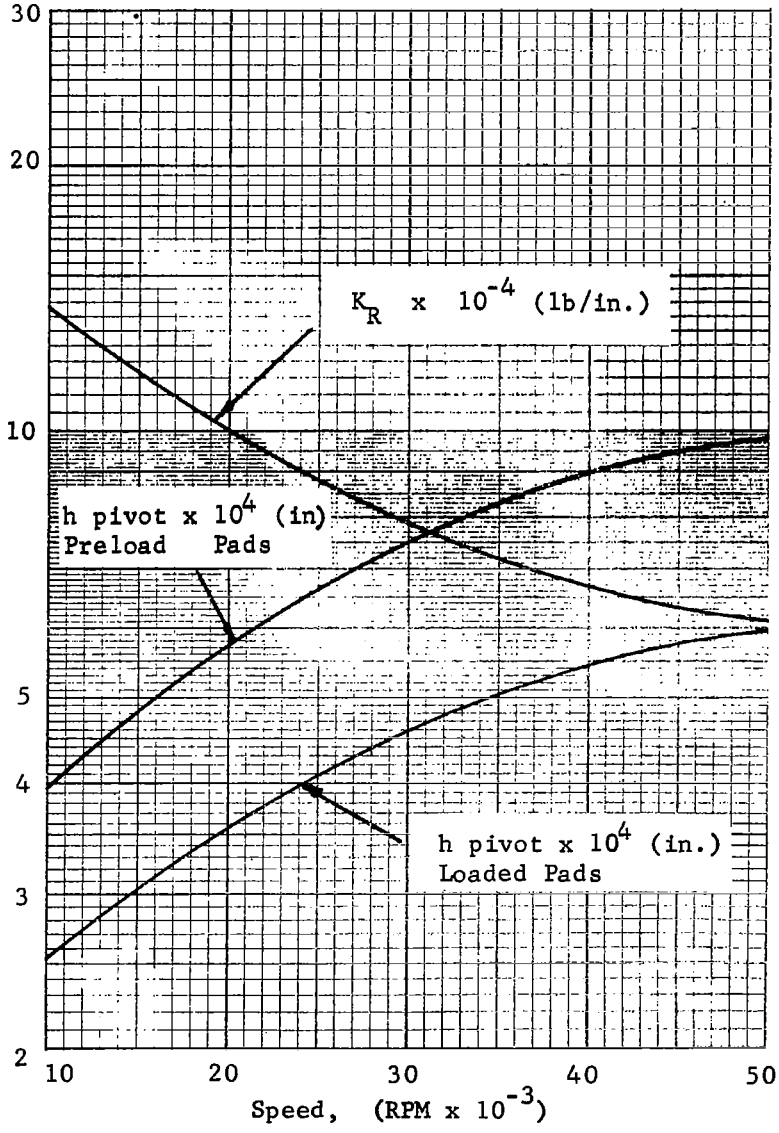

Fig. 32 Performance of Tilting Pad Journal Bearing, Case I

TILTING PADS - CASE I

Load = 20 lb. $\mu = 6.0 \times 10^{-9}$ lb-sec/in^2

Preload = 20 lb. $\frac{L}{D} = 1.0$

$\frac{C}{R} = 3.5 \times 10^{-3}$ in. (at 0 RPM) $\frac{t}{D} = 0.05$

$P_a = 15$ psia

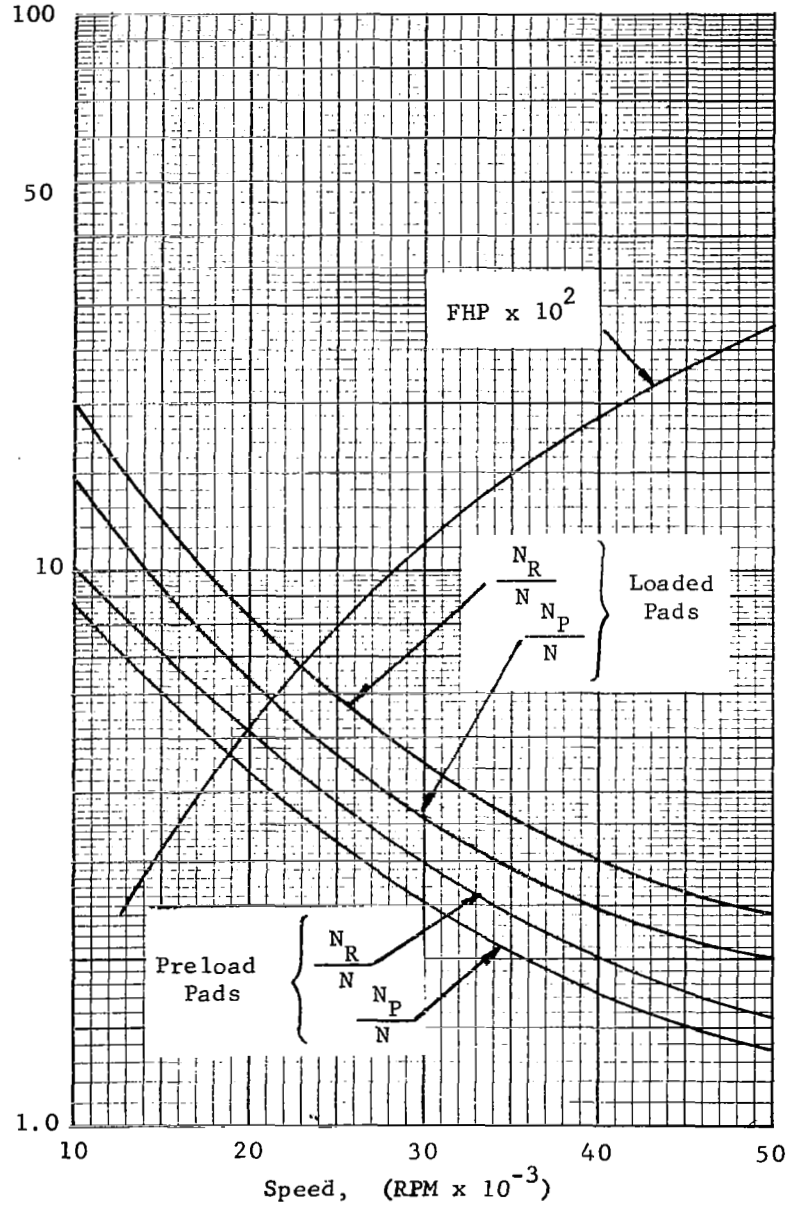

Fig. 33 Performance of Tilting Pad Journal Bearing, Case I

TILTING PADS - CASE J

Load = 20 lb. $\mu = 6.0 \times 10^{-9}$ lb-sec/in

Preload = 20 lb. $\frac{L}{D} = 1.0$

$\frac{C}{R} = 2.5 \times 10^{-3}$ in. (at 0 RPM) $\frac{t}{D} = 0.05$

$P_a = 15$ psia

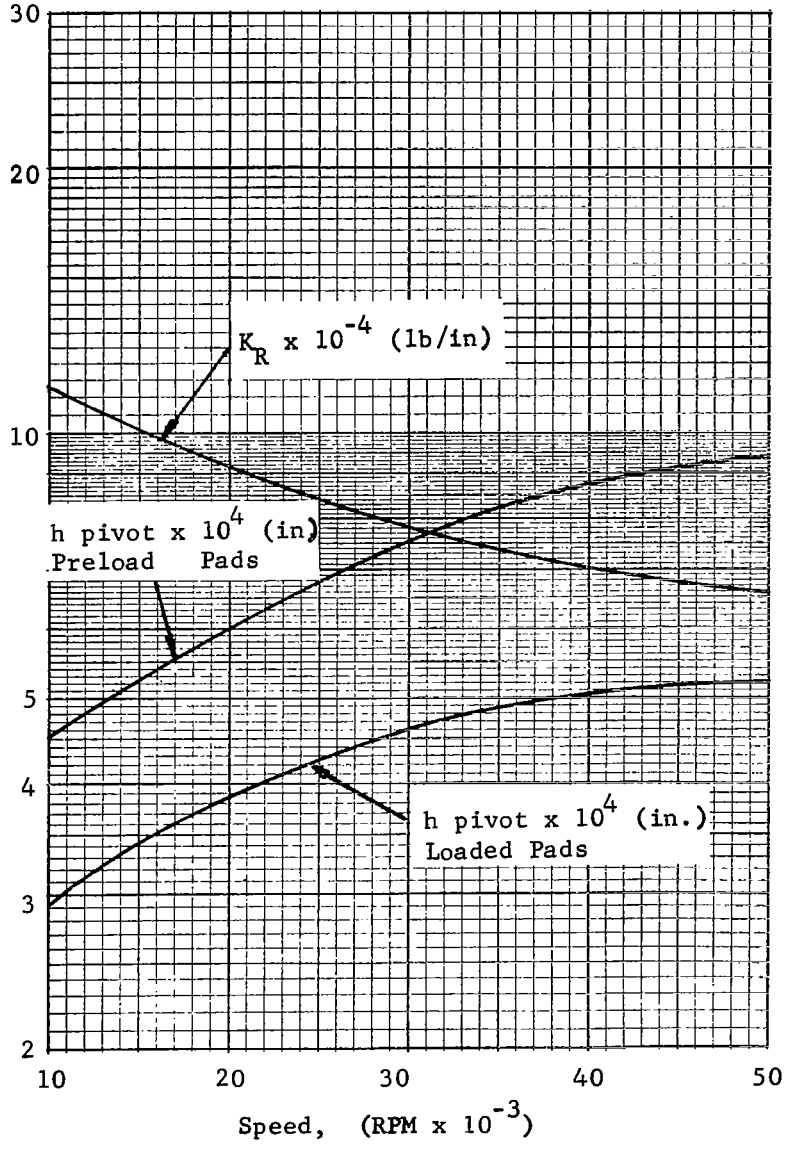

Fig. 34 Performance of Tilting Pad Journal Bearing, Case J

TILTING PADS - CASE J

Load = 20 lb.

Preload = 20 lb.

$\frac{C}{R}$ = 2.5×10^{-3} in. (at 0 RPM)

P_a = 15 psia

μ = 6.0×10^{-9} lb-sec/in^2

$\frac{L}{D}$ = 1.0

$\frac{t}{D}$ = 0.05

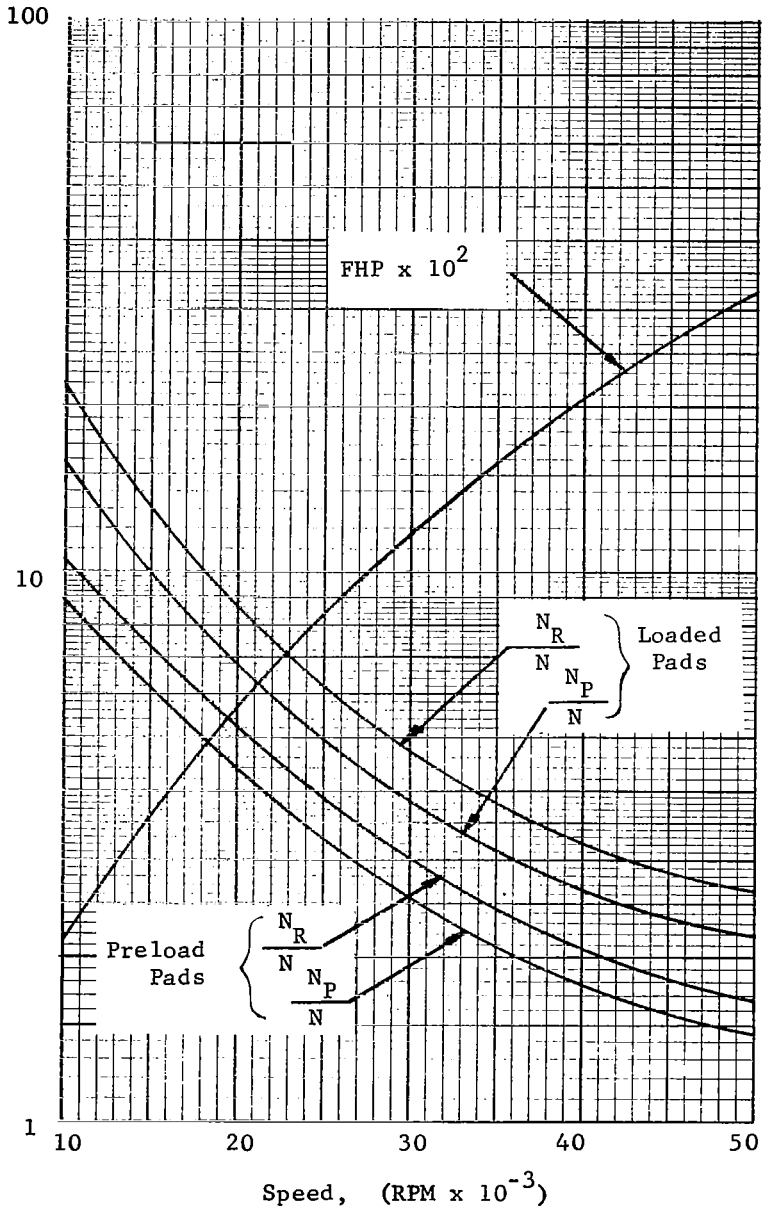

Fig. 35 Performance of Tilting Journal Bearing, Case J

TILTING PADS - CASE K

Load = 20 lb.

Preload = 0.

$\frac{C}{R}$ = 2.5×10^{-3} in. (at 0 RPM)

P_a = 15 psia

μ = 6.0×10^{-4} lb-sec/in^2

$\frac{L}{D}$ = 1.0

$\frac{t}{D}$ = 0.05

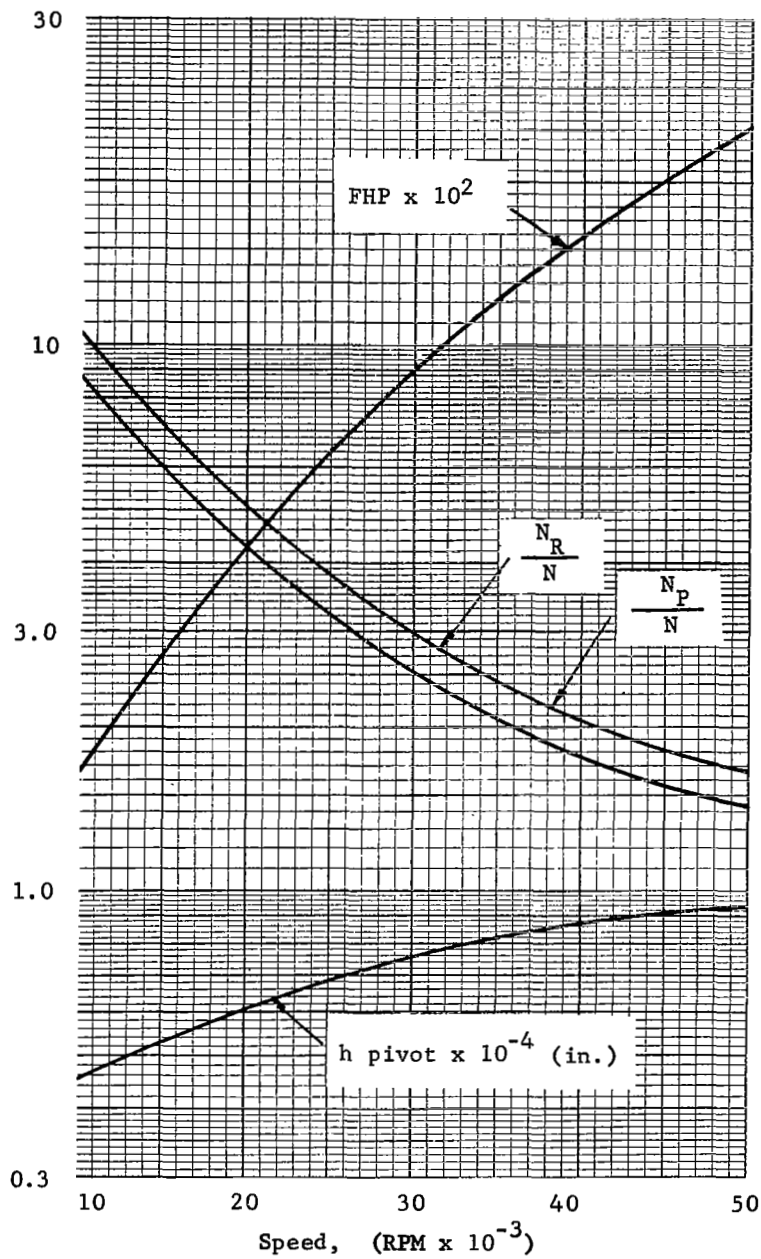

Fig. 36 Performance of Tilting Pad Journal Bearing, Case K

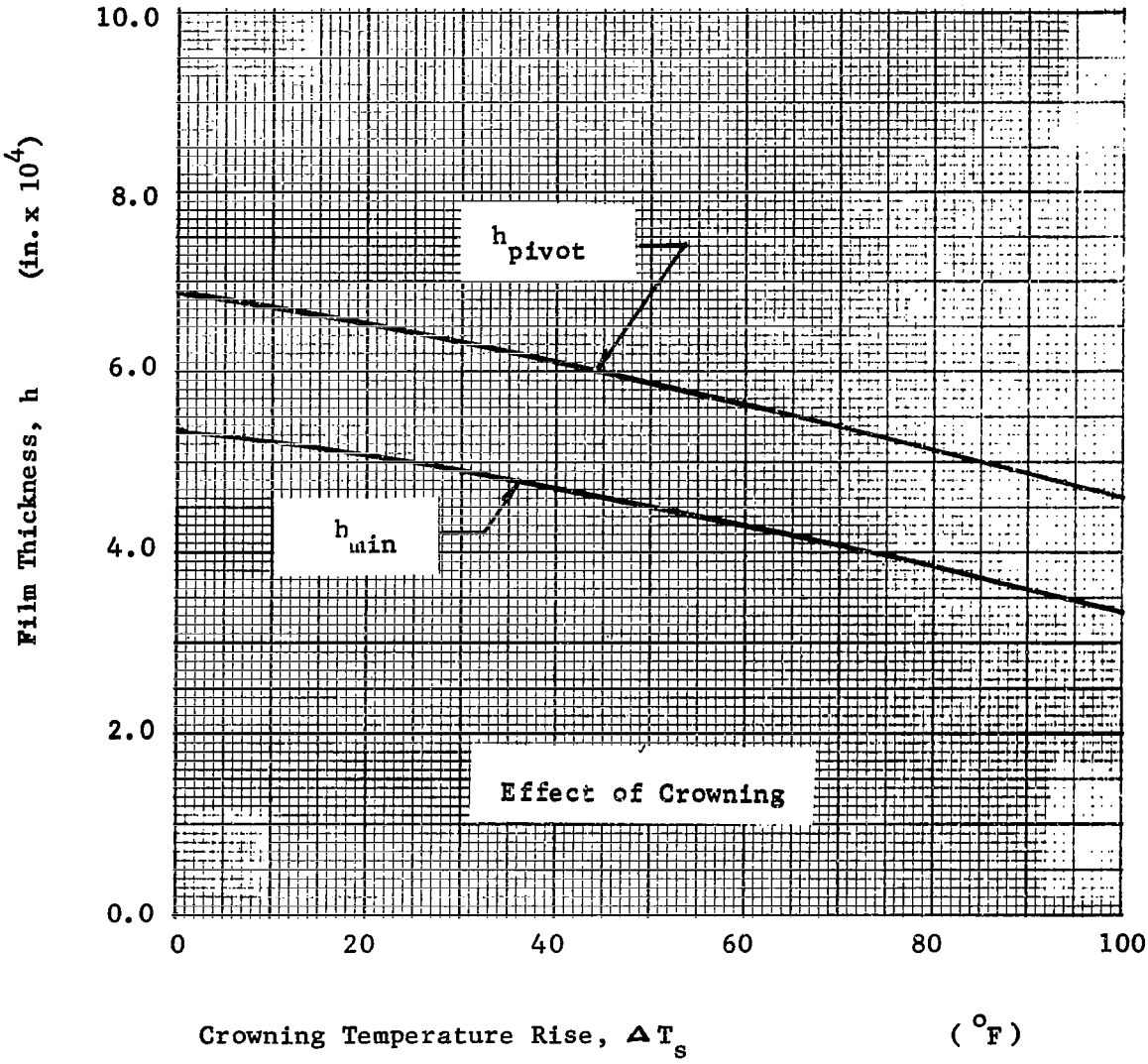

Fig. 38 Reduction of Pivot and Minimum Film Thicknesses Due to Crowning of the Shaft

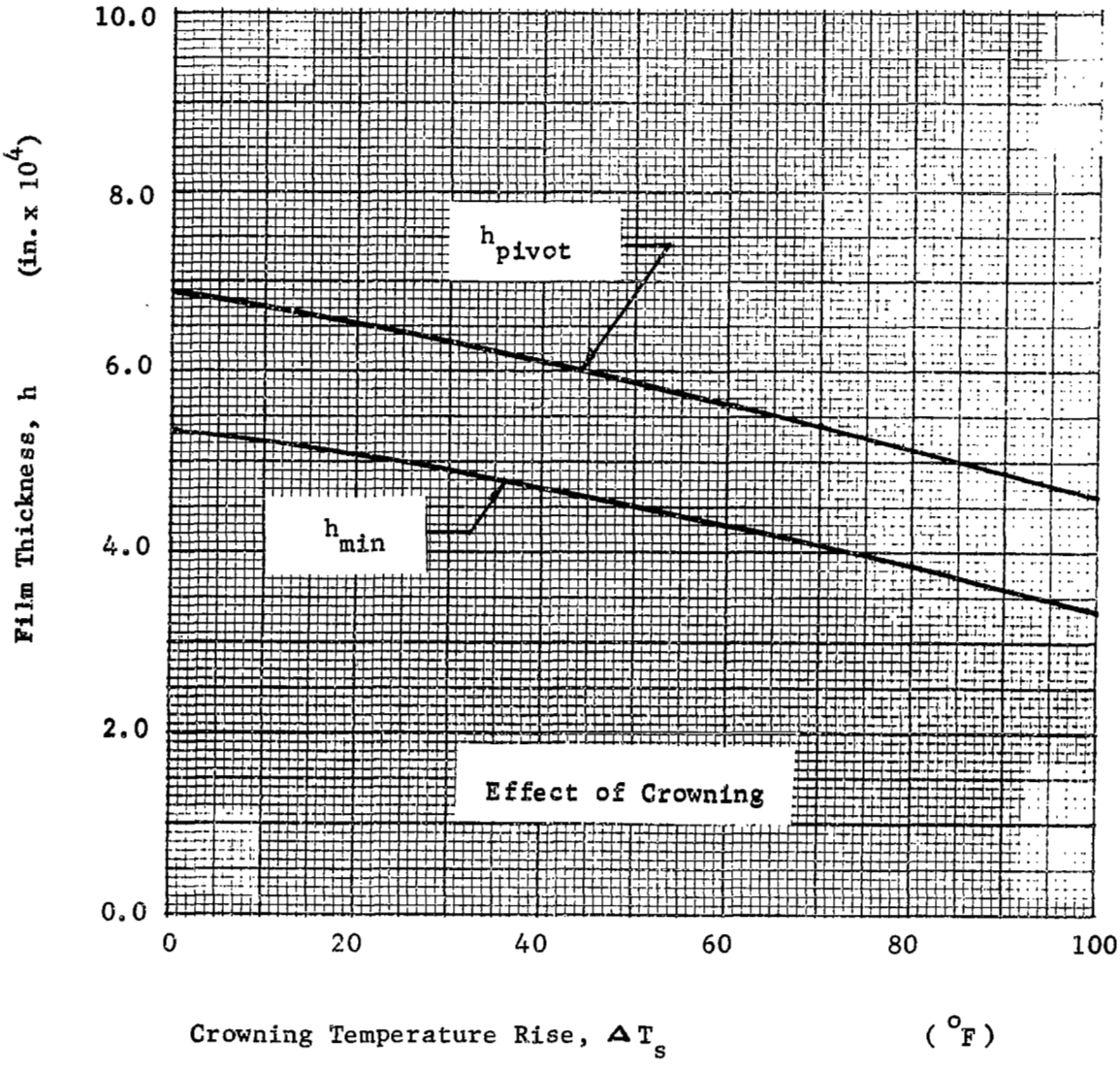

Fig. 38 Reduction of Pivot and Minimum Film Thicknesses Due to Crowning of the Shaft

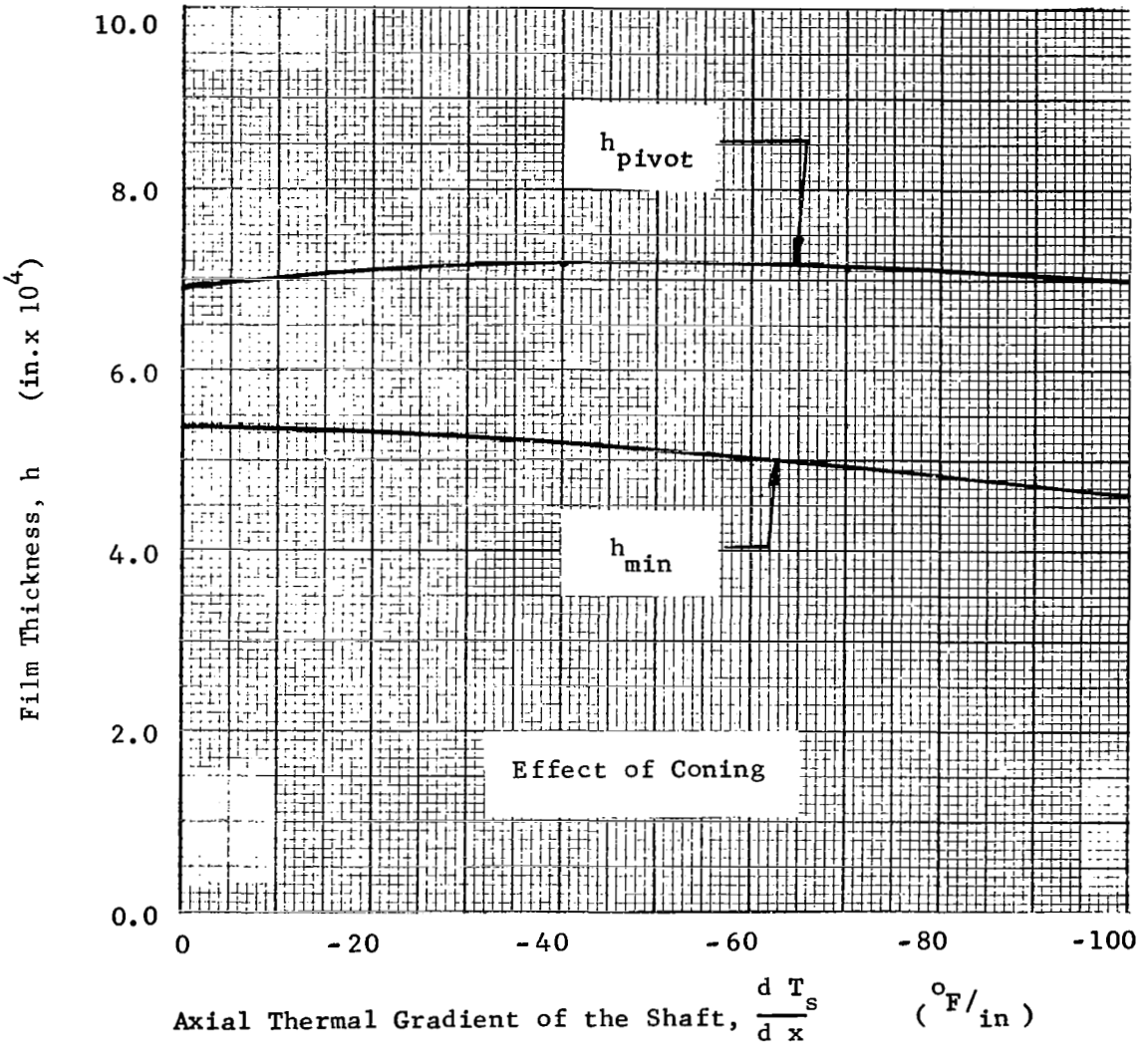

Fig. 39 Reduction of Pivot and Minimum Film Thicknesses Due to Coning of the Shaft

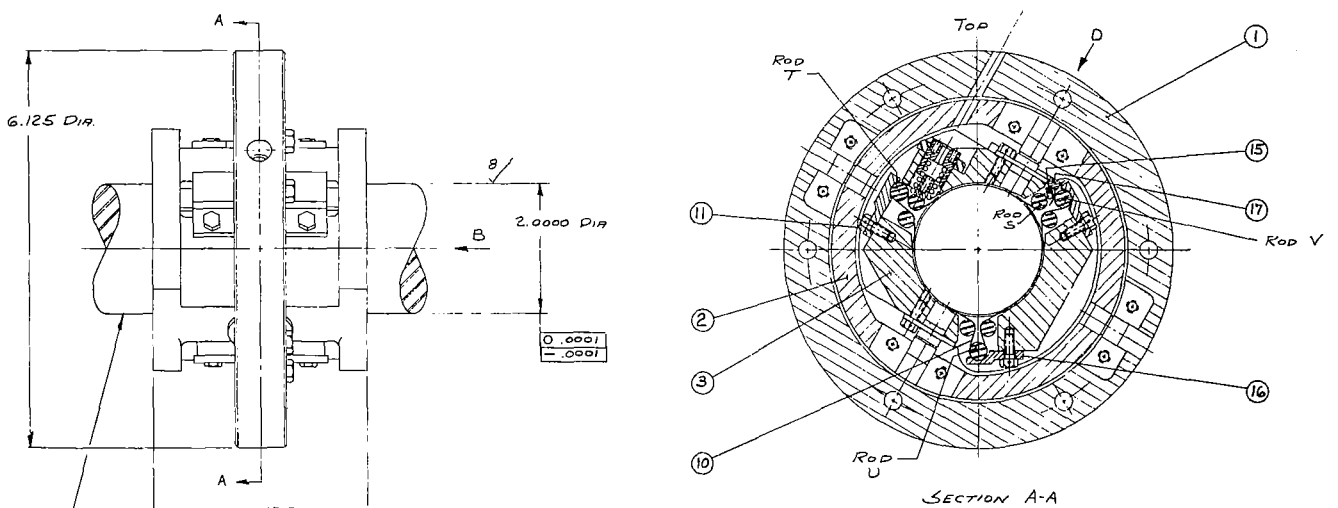

Fig. 40 Detailed Design of the Foil Journal Bearing

FOIL JOURNAL BEARING - CASE A

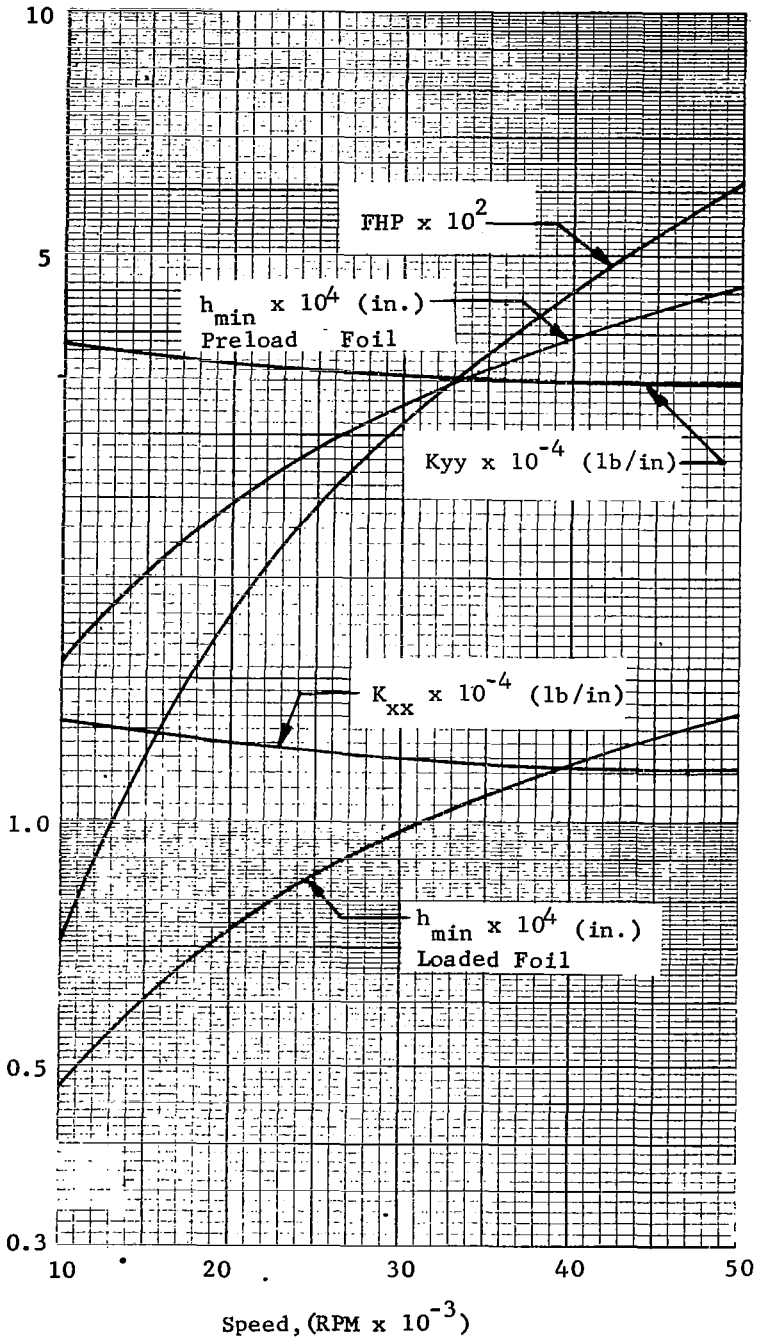

Load = 20 lb.

Preload = 8 lb.

P_a = 5 psia

$\mu = 6.0 \times 10^{-9} \frac{\text{lb-sec}}{\text{in}^2}$

$\frac{L}{D}$ = 1.0

Foil thickness = 0.001 in.

(T housing - T shaft) = 200 F.

Fig.41 Performance of Foil Journal Bearing, Case A

FOIL JOURNAL BEARING - CASE B

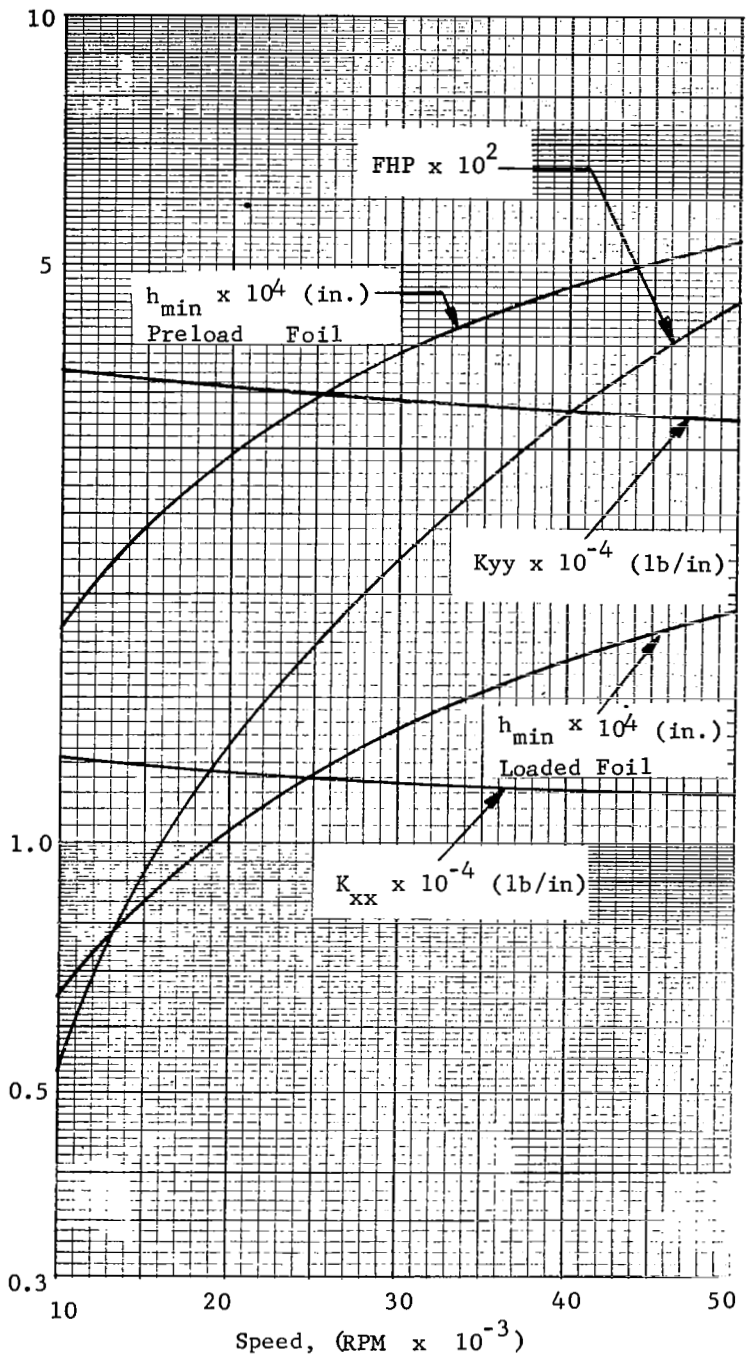

Load = 20 lb.

Preload = 8 lb.

P_a = 15 psia

μ = 6.0×10^{-9} $\frac{\text{lb-sec}}{\text{in}^2}$

$\frac{L}{D}$ = 1.0

Foil thickness = 0.001 in.
(T housing - T shaft) = 200 F.

Fig. 42 Performance of Foil Journal Bearing, Case B

FOIL JOURNAL BEARING - CASE C

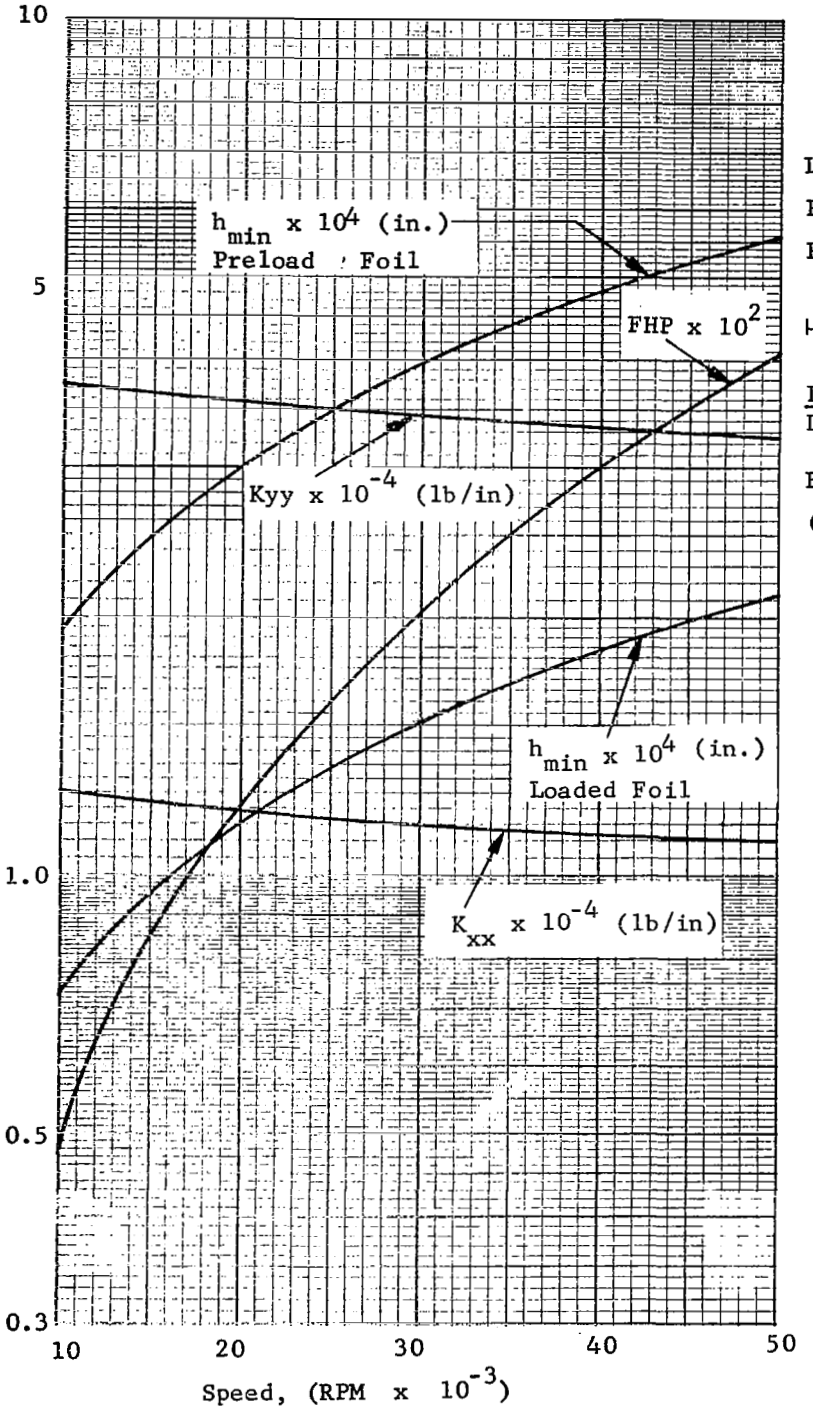

Load = 20 lb.

Preload = 8 lb.

P_a = 25 psia

$\mu = 6.0 \times 10^{-9} \frac{\text{lb-sec}}{\text{in}^2}$

$\frac{L}{D} = 1.0$

Foil thickness = 0.001 in.

(T housing - T shaft) = 200 F.

Fig. 43 Performance of Foil Journal Bearing, Case C

FOIL JOURNAL BEARING CASE - D

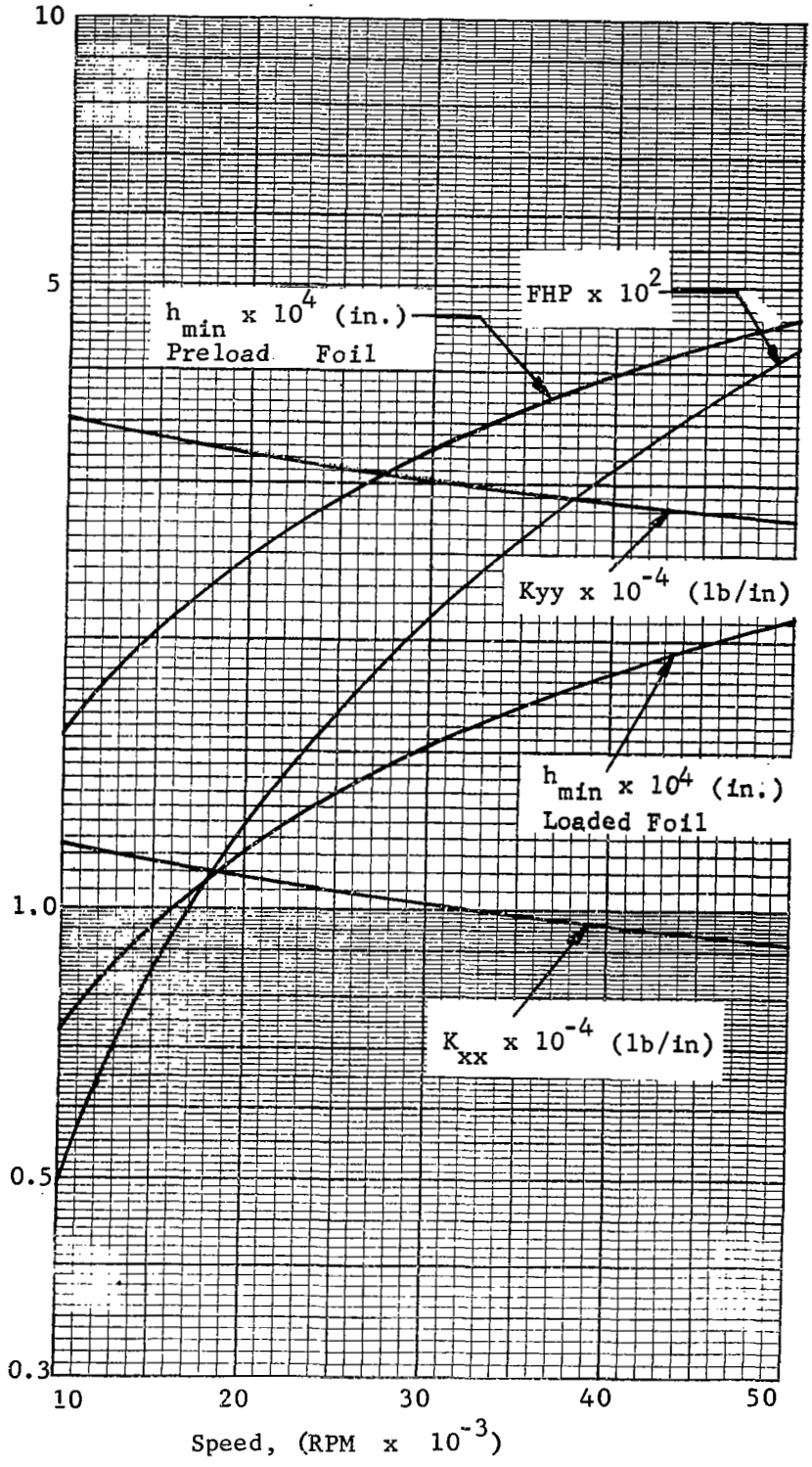

Load = 10 lb.

Preload = 8 lb.

P_a = 5 psia

$\mu = 6.0 \times 10^{-9} \frac{\text{lb-sec}}{\text{in}^2}$

$\frac{L}{D} = 1.0$

Foil thickness = 0.001 in.

(T housing - T shaft) = 200 F.

Fig. 44 Performance of Foil Journal Bearings, Case D

FOIL JOURNAL BEARING - CASE E

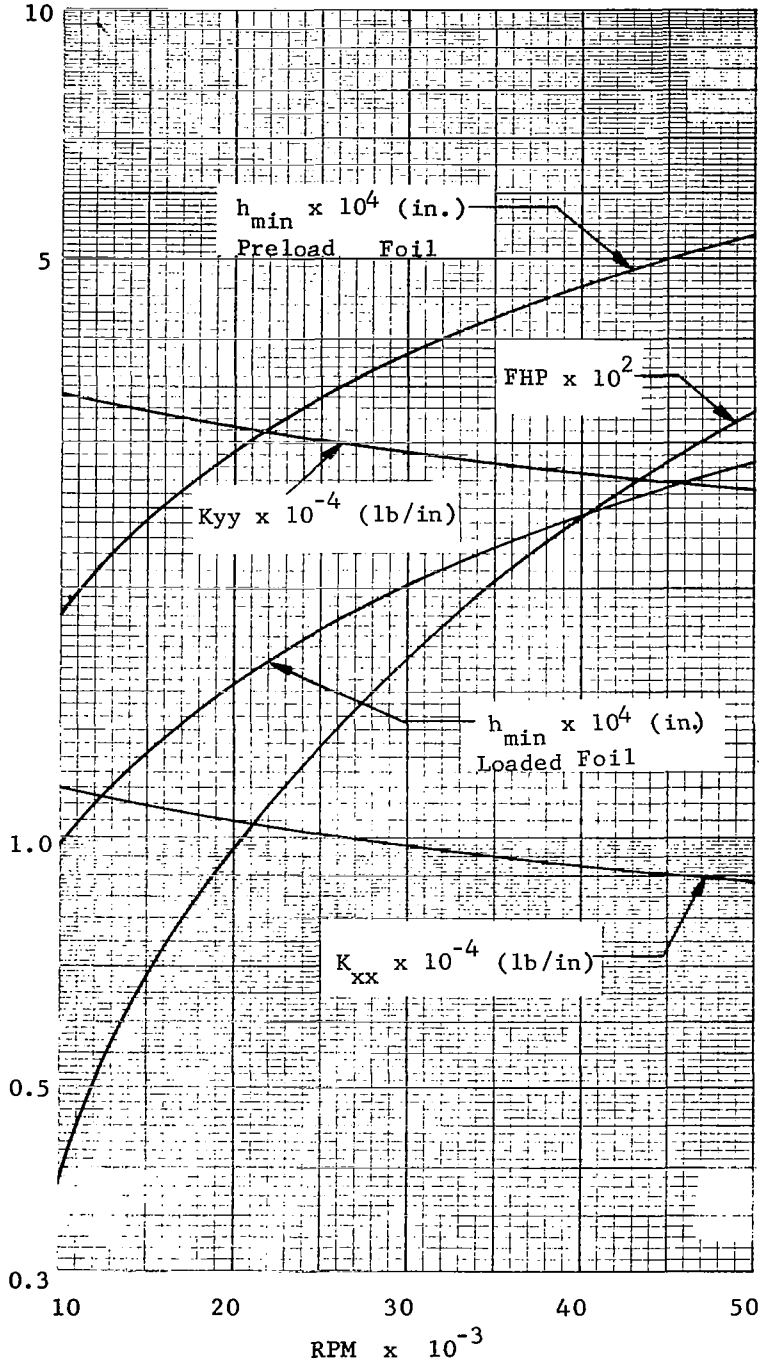

Load = 10 lb.

Preload = 8 lb.

P_a = 15 psia

$\mu = 6.0 \times 10^{-9} \frac{\text{lb-sec}}{\text{in}^2}$

$\frac{L}{D} = 1.0$

Foil thickness = 0.001 in.

(T housing - T shaft) = 200 F.

Fig. 45 Performance of Foil Journal Bearing, Case E

FOIL JOURNAL BEARING - CASE F

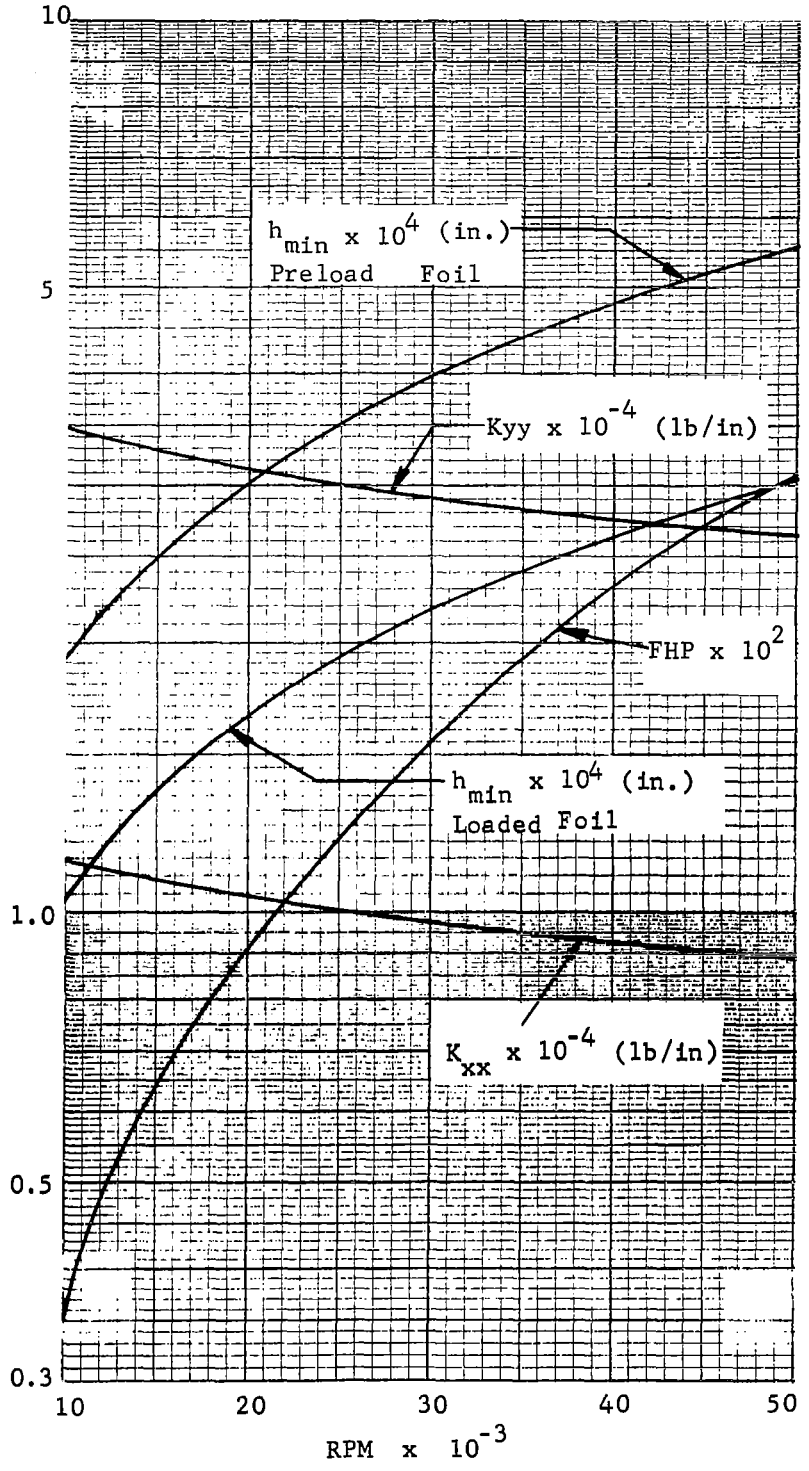

Load = 10 lb.

Preload = 8 lb.

P_a = 25 psia

μ = 6.0×10^{-9} $\frac{\text{lb-sec}}{\text{in}^2}$

$\frac{L}{D}$ = 1.0

Foil thickness = 0.001 in.

(T housing - T shaft) = 200 F.

Fig. 46 Performance of Foil Journal Bearing, Case F

FOIL JOURNAL BEARING - CASE G

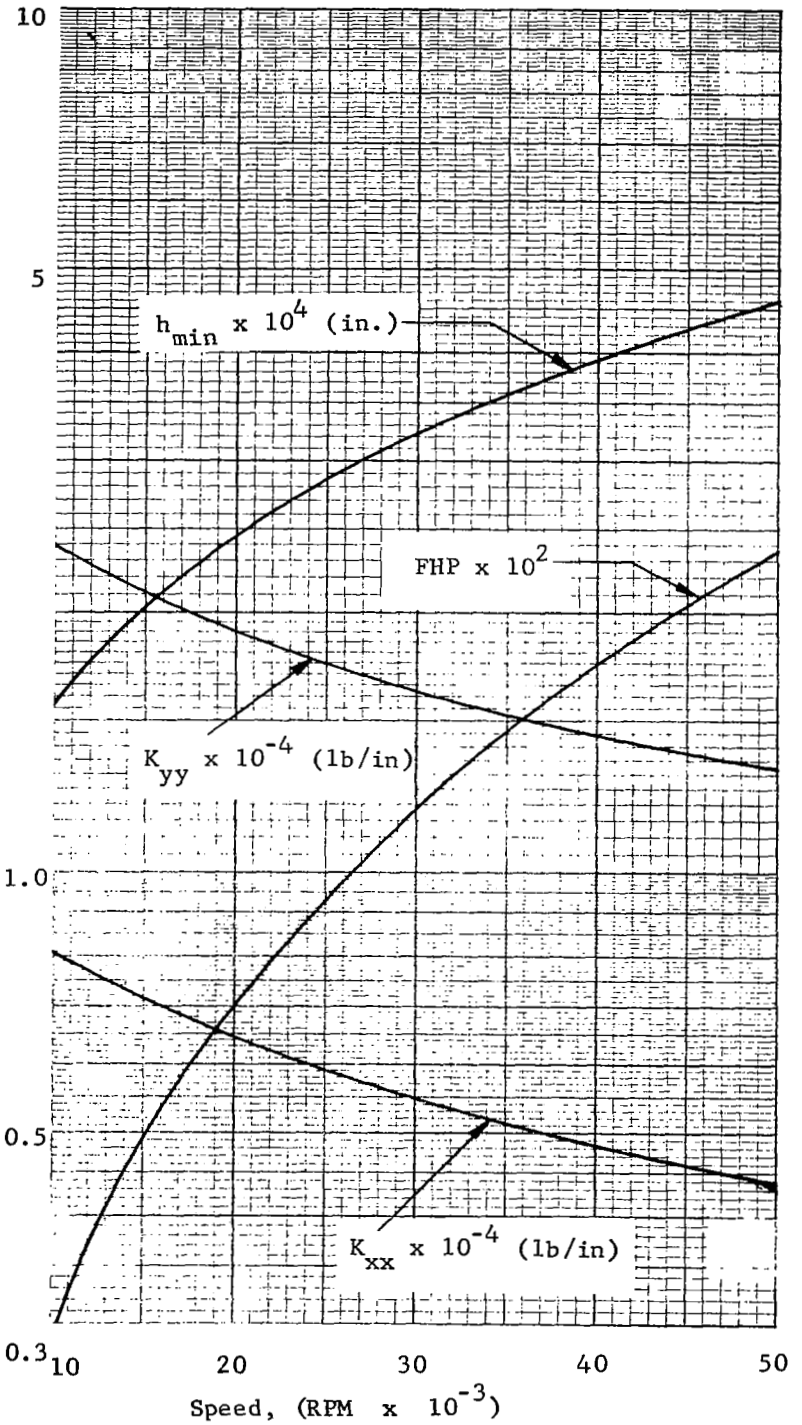

Load = 0 lb.

Preload = 8 lb.

P_a = 25 psia

μ = 6.0 x 10^{-9} $\frac{\text{lb-sec}}{\text{in}^2}$

$\frac{L}{D}$ = 1.0

Foil thickness = 0.001 in.

(T housing - T shaft) = 200 F.

Fig.47 Performance of Foil Journal Bearing, Case G

FOIL JOURNAL BEARING - CASE H

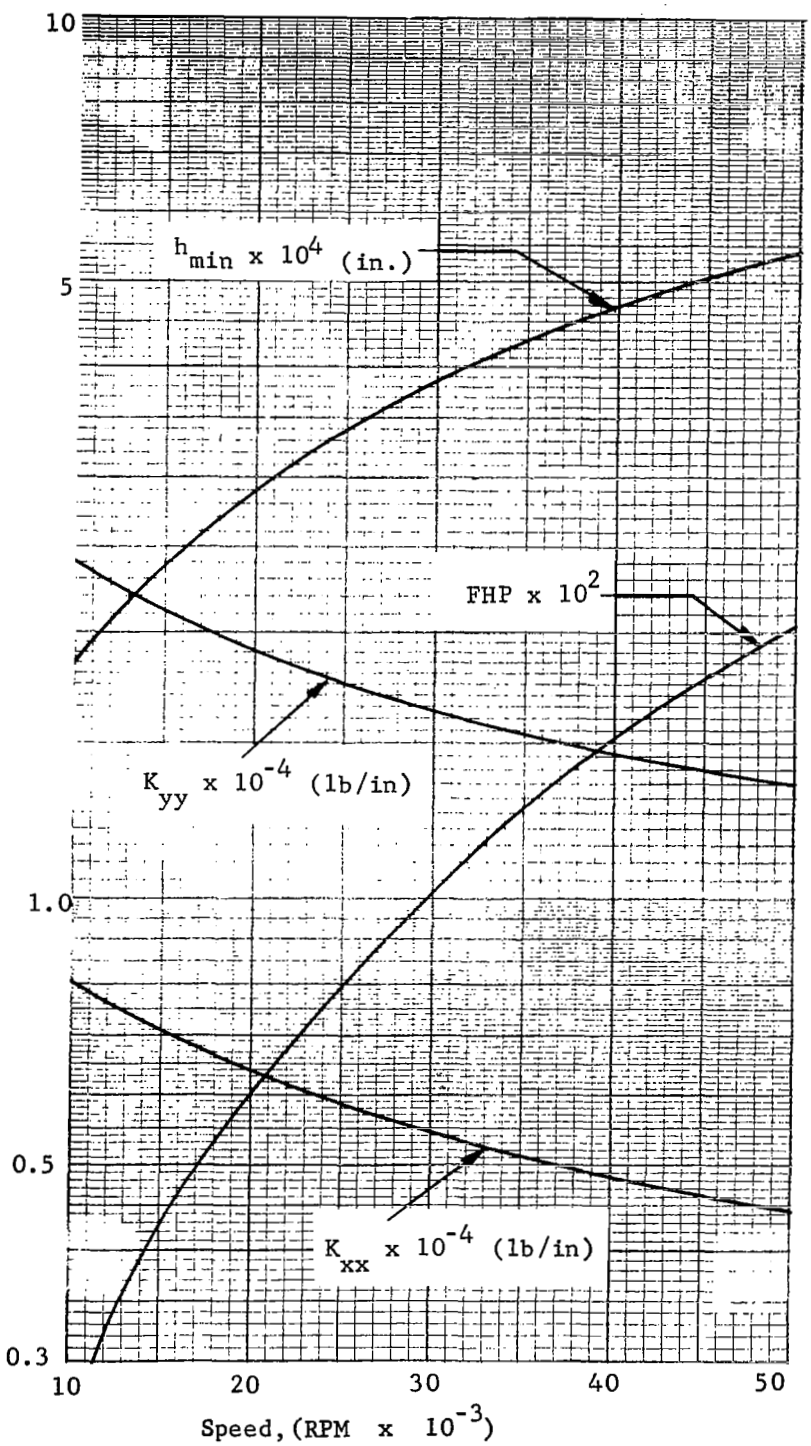

Load = 0 lb.

Preload = 8 lb.

P_a = 15 psia

$\mu = 8.0 \times 10^{-9} \frac{\text{lb-sec}}{\text{in}^2}$

$\frac{L}{D} = 1.0$

Foil thickness = 0.001 in.

(T housing - T shaft) = 200 F.

Fig. 48 Performance of Foil Journal Bearing, Case H

FOIL JOURNAL BEARING - CASE I

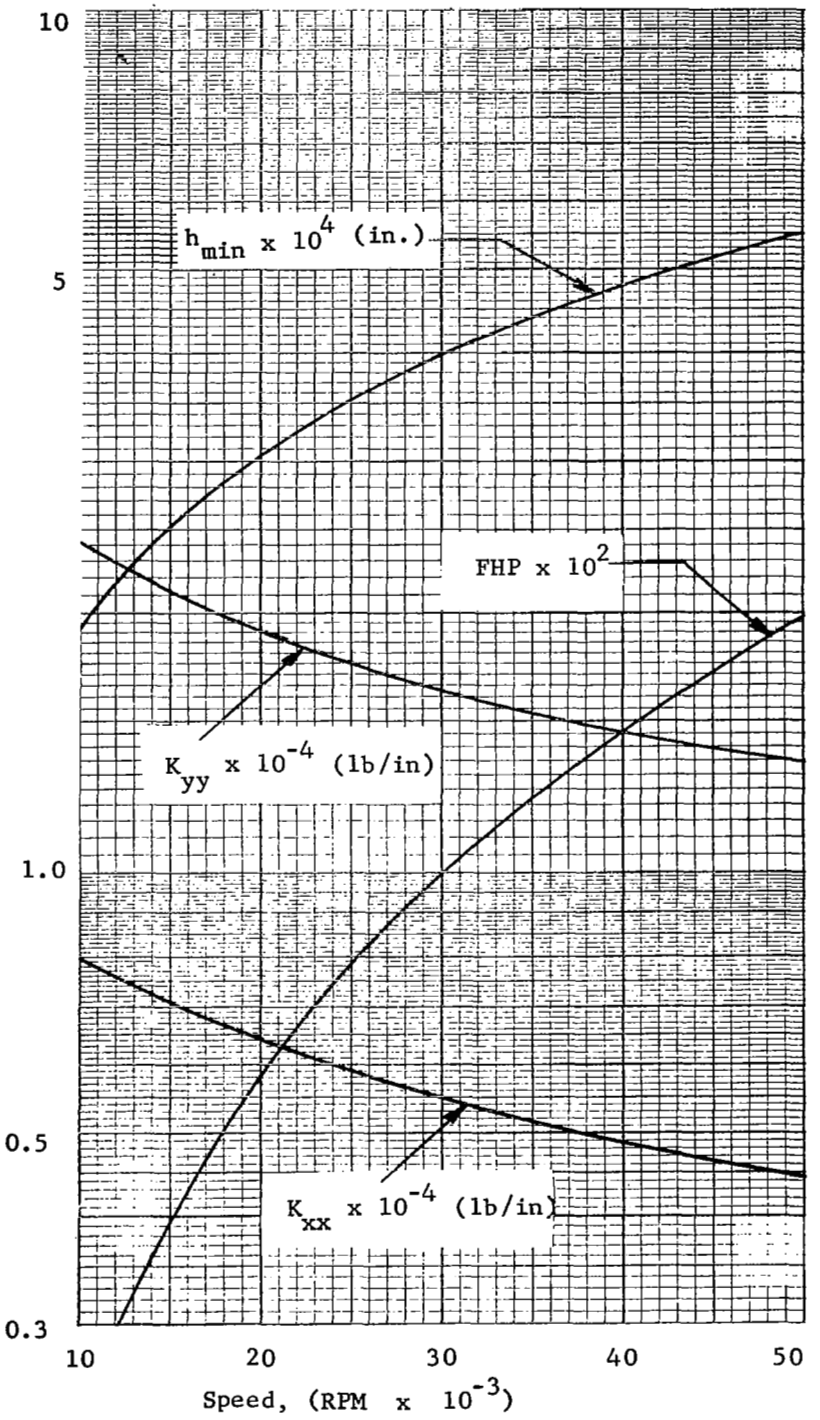

Load = 0 lb.

Preload = 8 lb.

P_a = 5 psia

$\mu = 6.0 \times 10^{-9} \frac{\text{lb-sec}}{\text{in}^2}$

$\frac{L}{D} = 1.0$

Foil thickness = 0.001 in.

(T housing - T shaft) = 200 F.

Fig. 49 Performance of Foil Journal Bearing, Case I

FOIL JOURNAL BEARING - CASE J

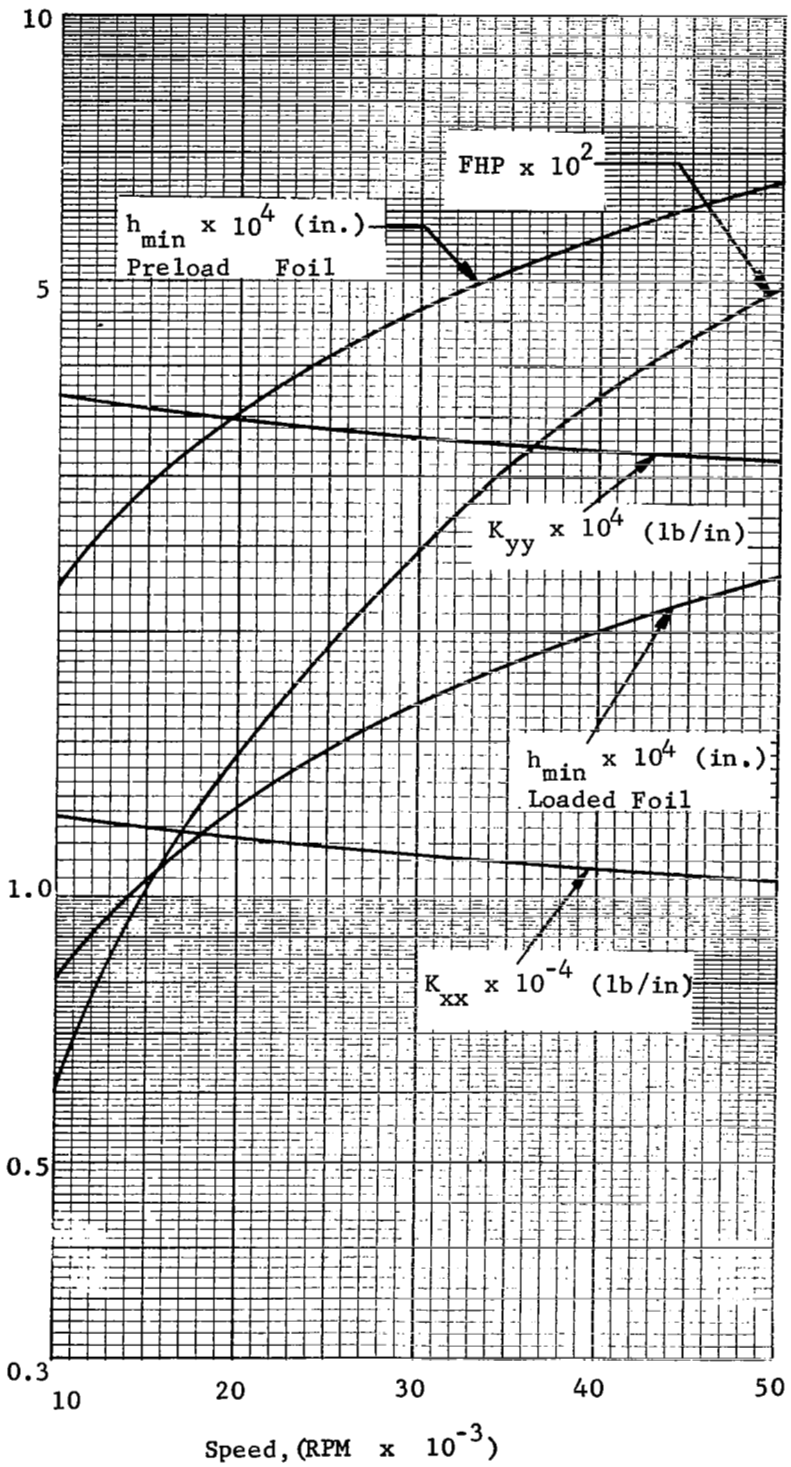

Load = 20 lb.

Preload = 8 lb.

P_a = 15 psia

$\mu = 8.0 \times 10^{-9} \frac{\text{lb-sec}}{\text{in}^2}$

$\frac{L}{D} = 1.0$

Foil thickness = 0.001 in.

(T housing - T shaft) = 200 F.

Fig.50 Performance of Foil Journal Bearing, Case J

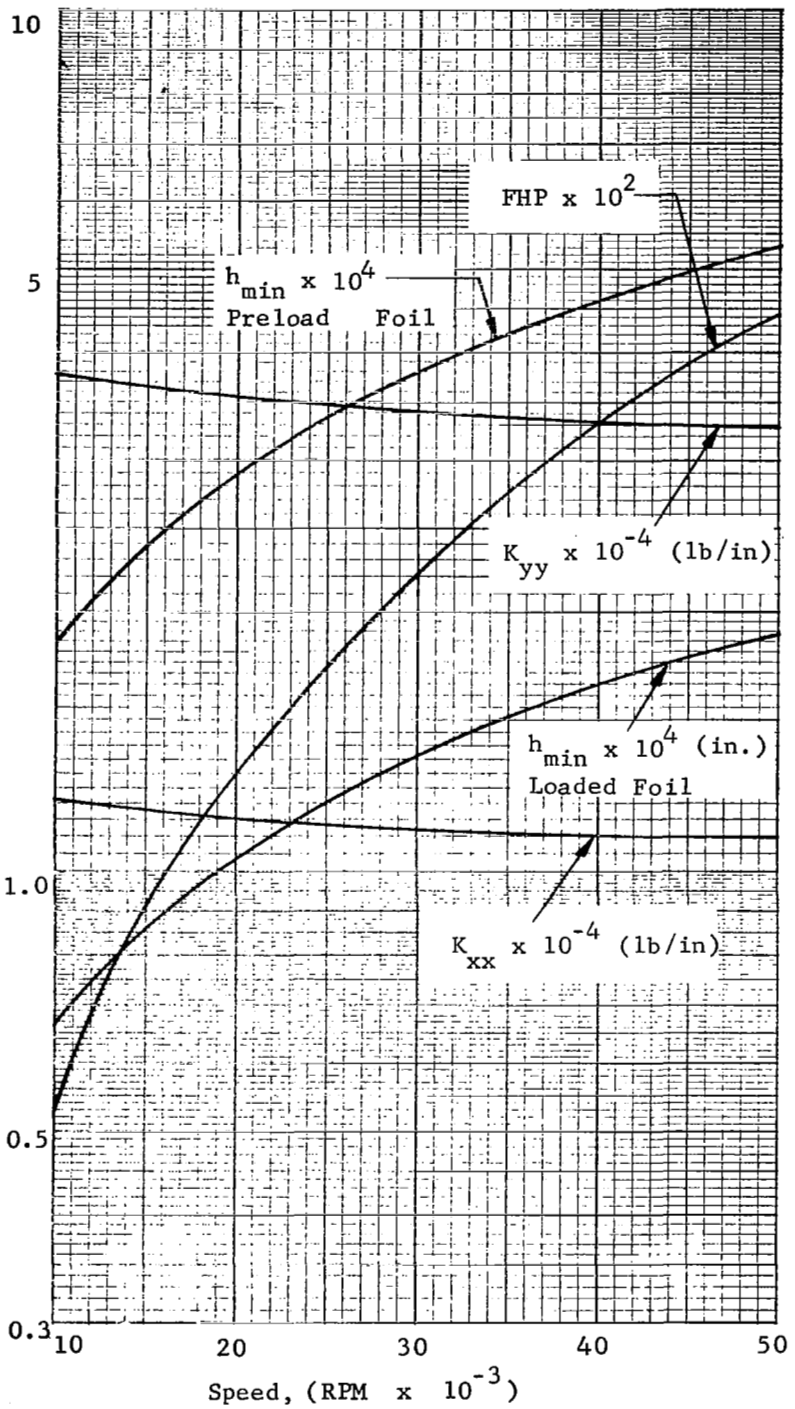

Fig. 51 Performance of Foil Journal Bearing, Case K

FOIL JOURNAL BEARING - CASE L

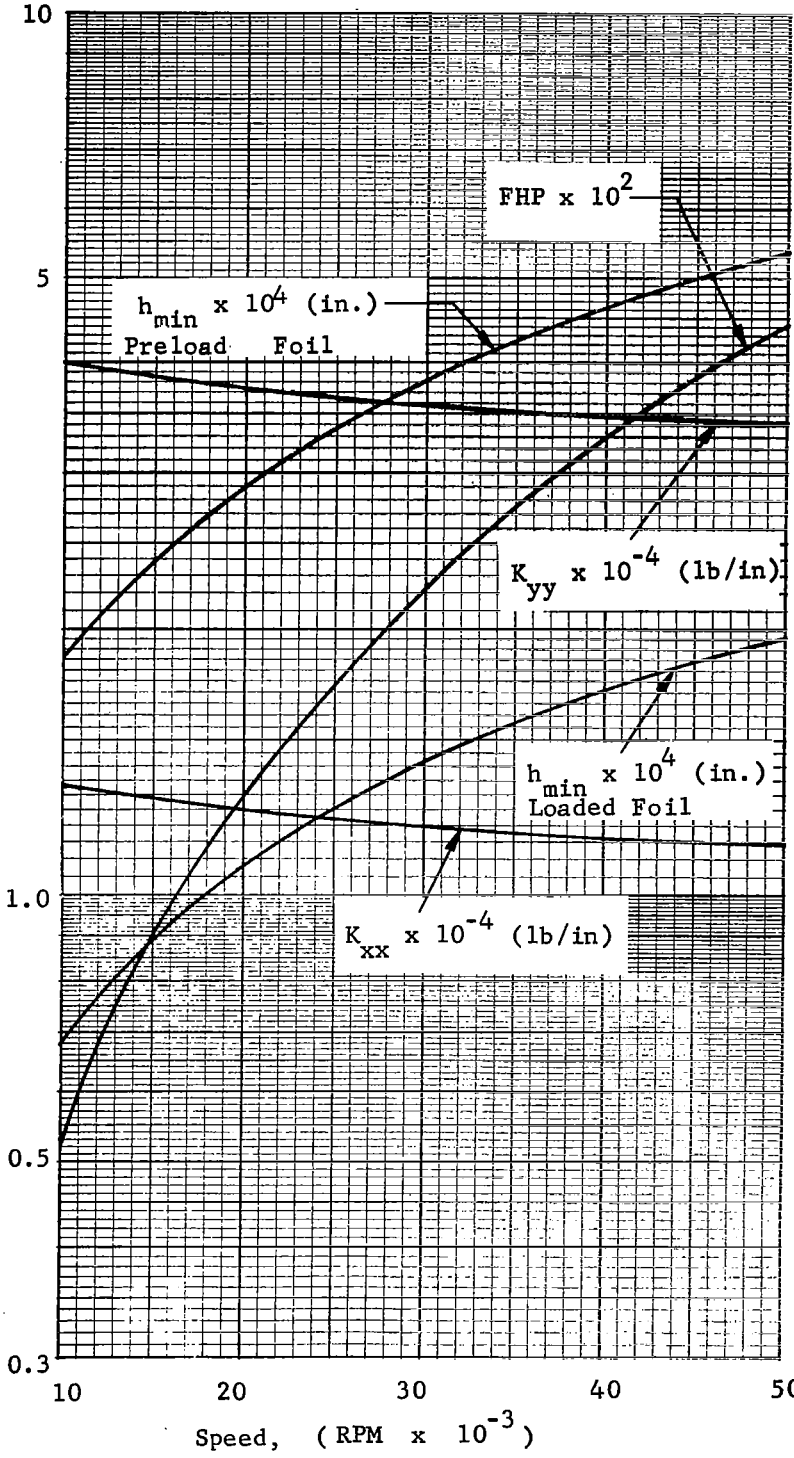

Load = 20 lb.

Preload = 8 lb.

P_a = 15 psia

μ = 6.0×10^{-9} $\frac{\text{lb-sec}}{\text{in}^2}$

$\frac{L}{D}$ = 1.0

Foil thickness = 0.001 in.

(T housing - T shaft) = 600 F.

Fig. 52 Performance of Foil Journal Bearing, Case L

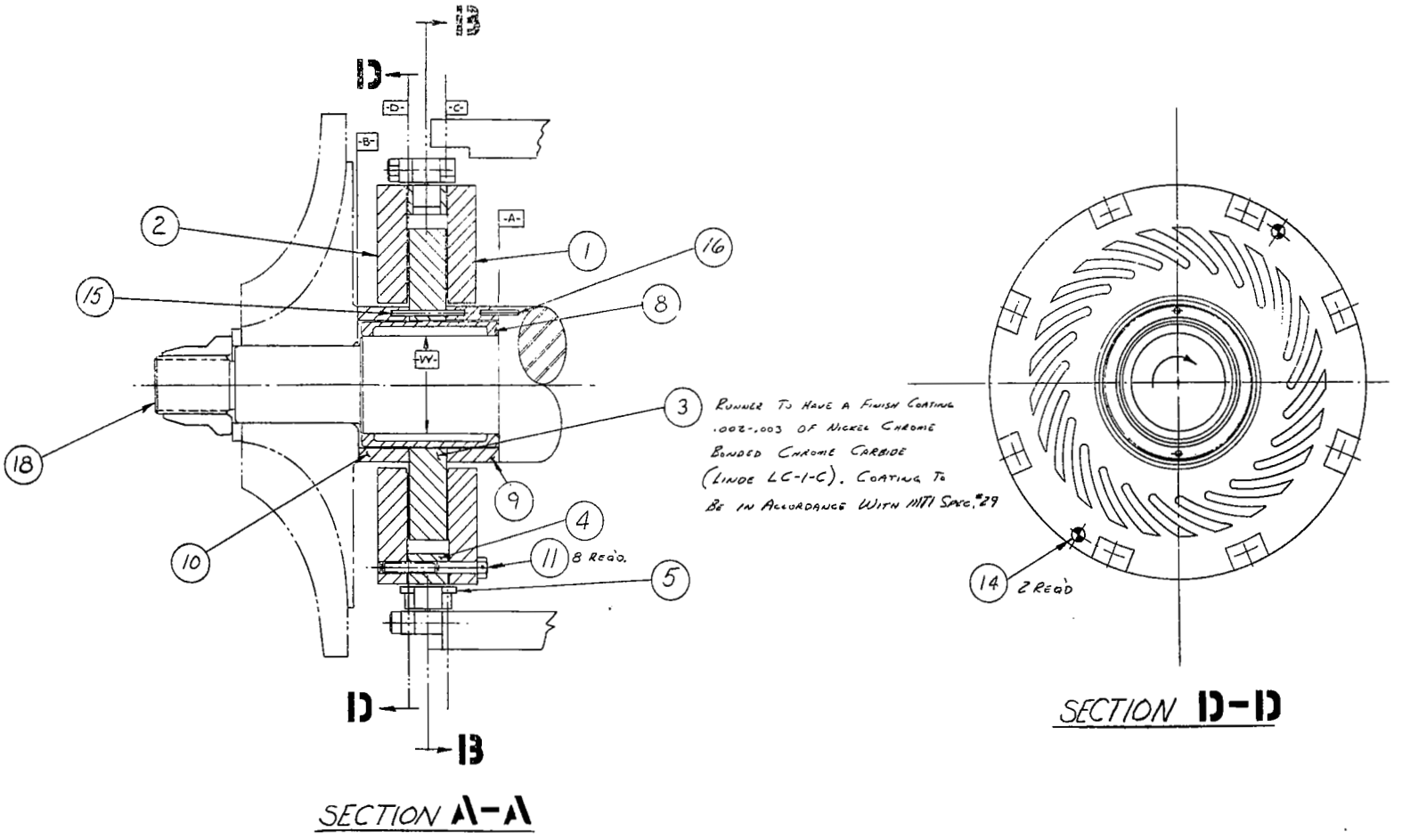

Fig. 53(a) Sectional View of the Flexibly-Mounted Thrust Bearing

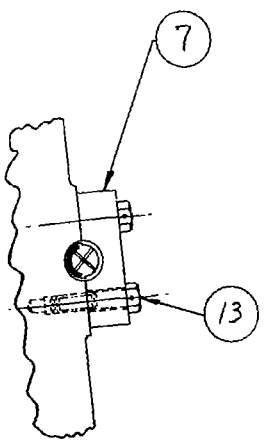

VIEW F-F
(TYP 2 PLACES)

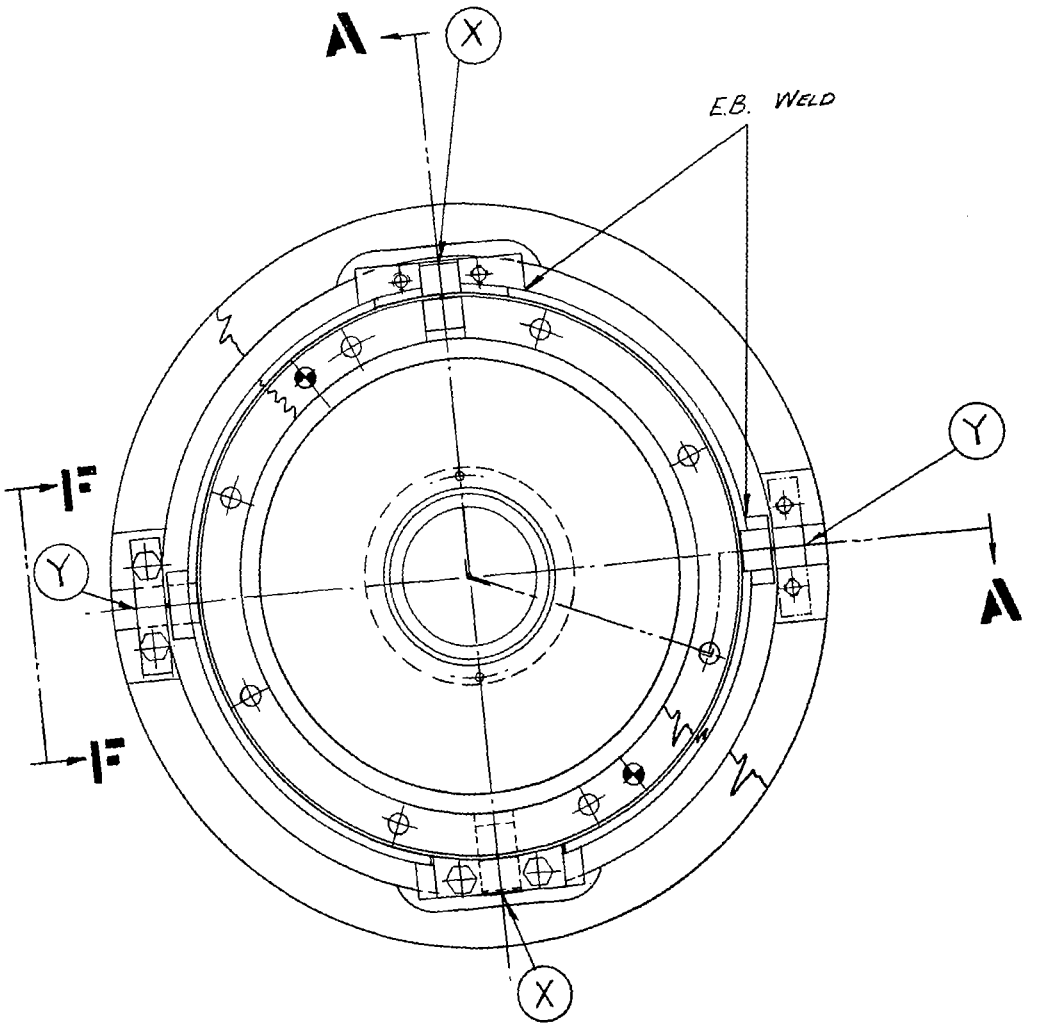

SECTION B-B

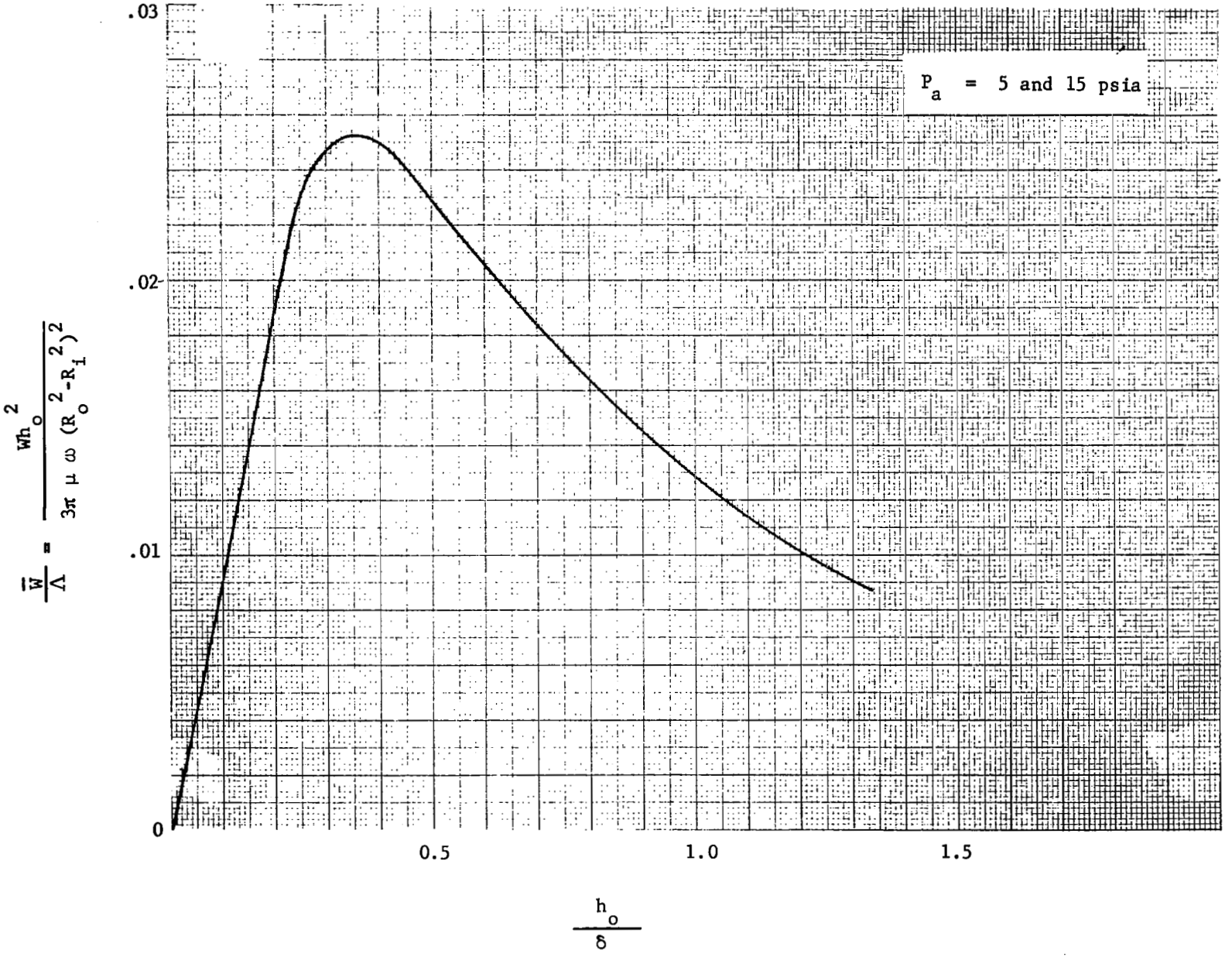

Fig. 54 Normalized Load Capacity of Thrust Plate

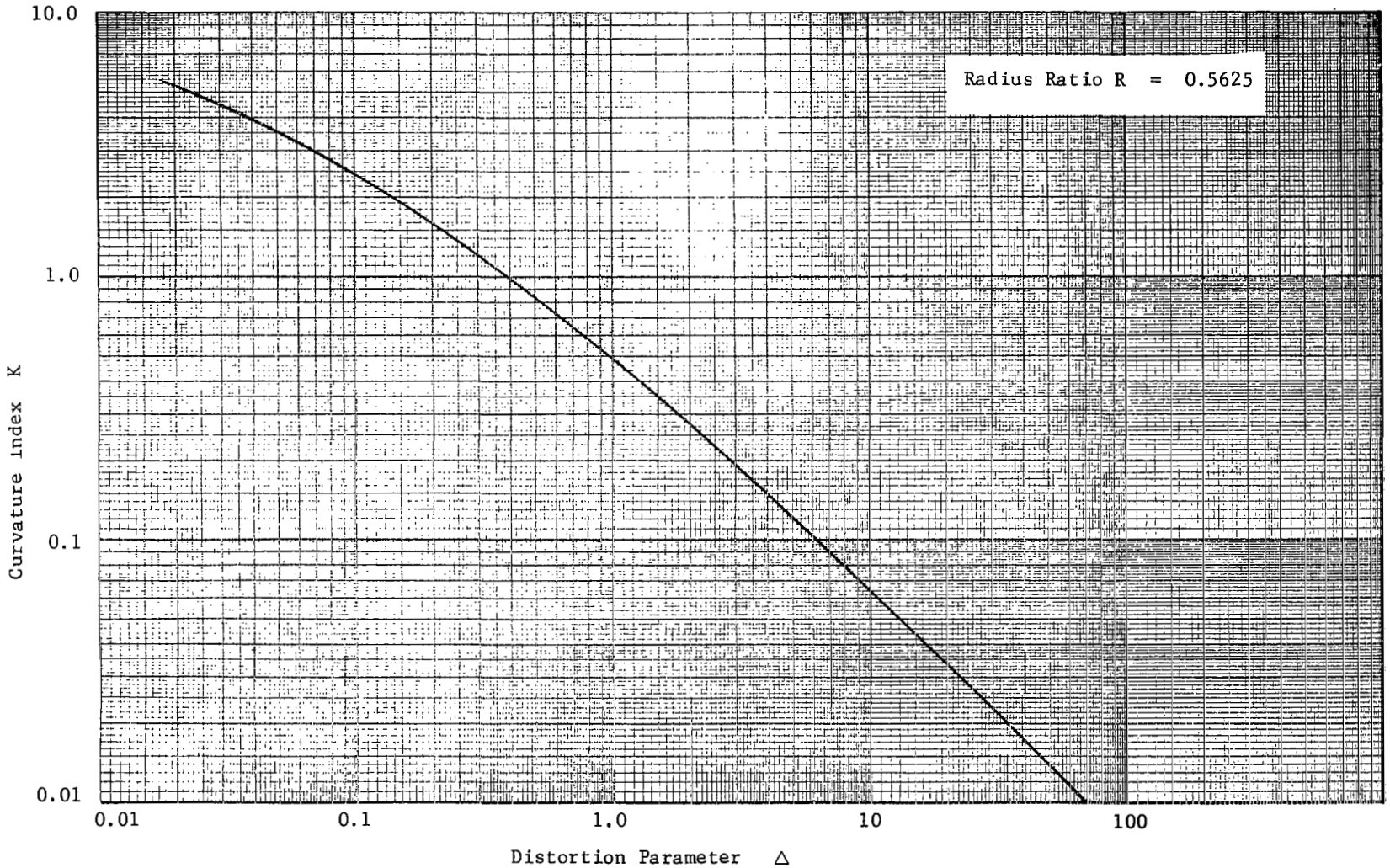

Fig. 55 Curvature Index Vs. Distortion Parameter

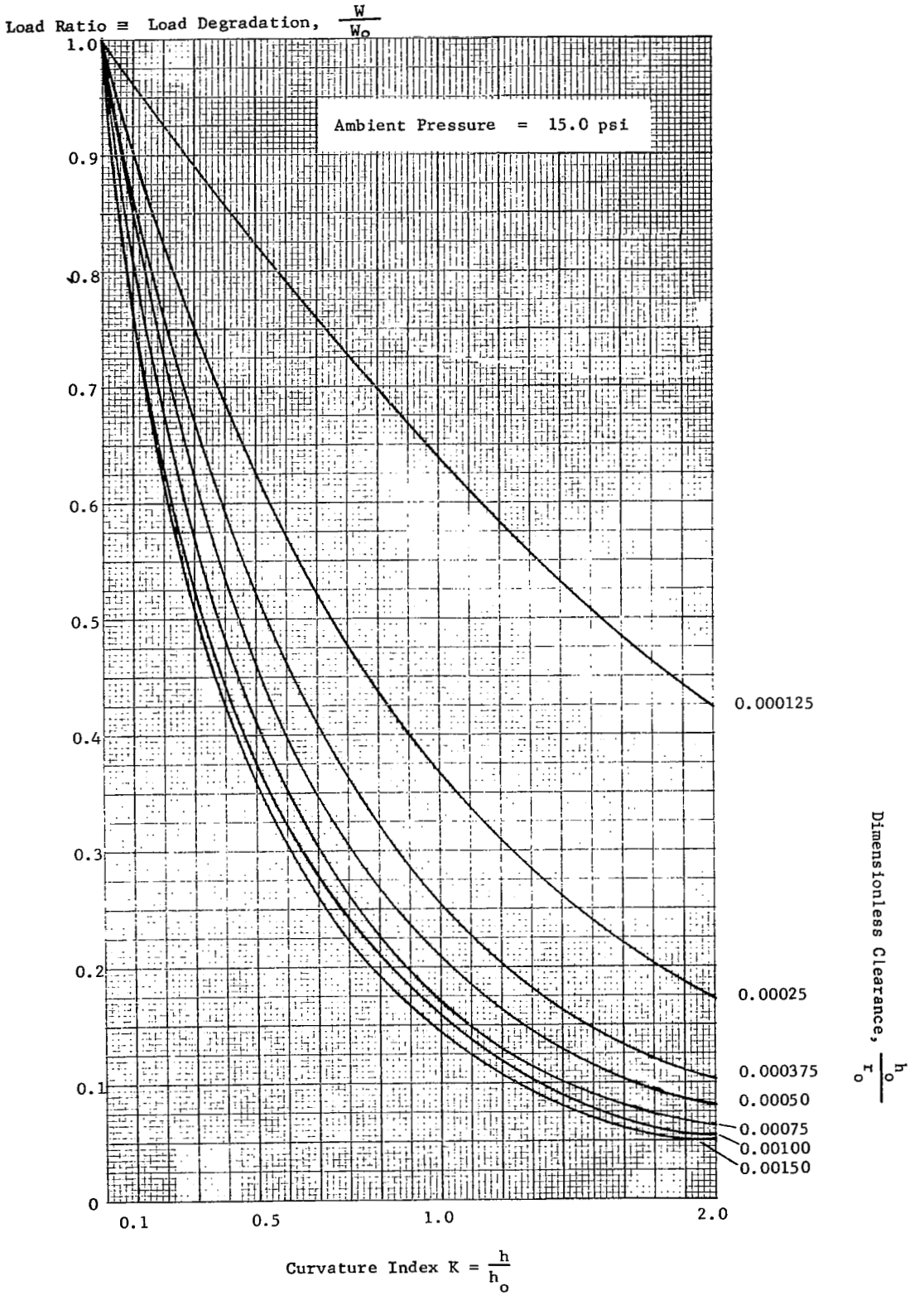

Fig. 56 Load Ratio vs. Curvature Index

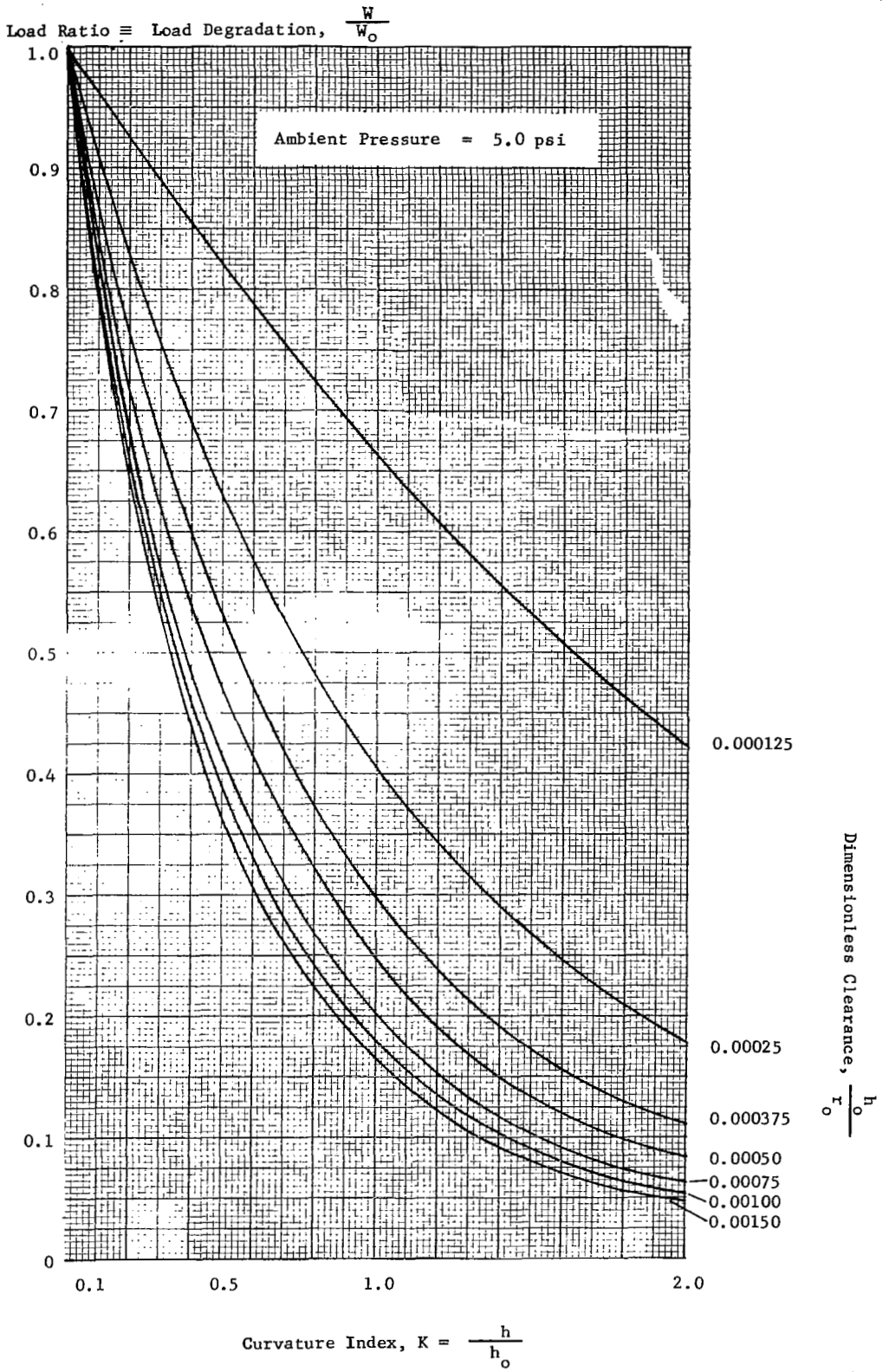

Fig. 57 Load Ratio vs. Curvature Index

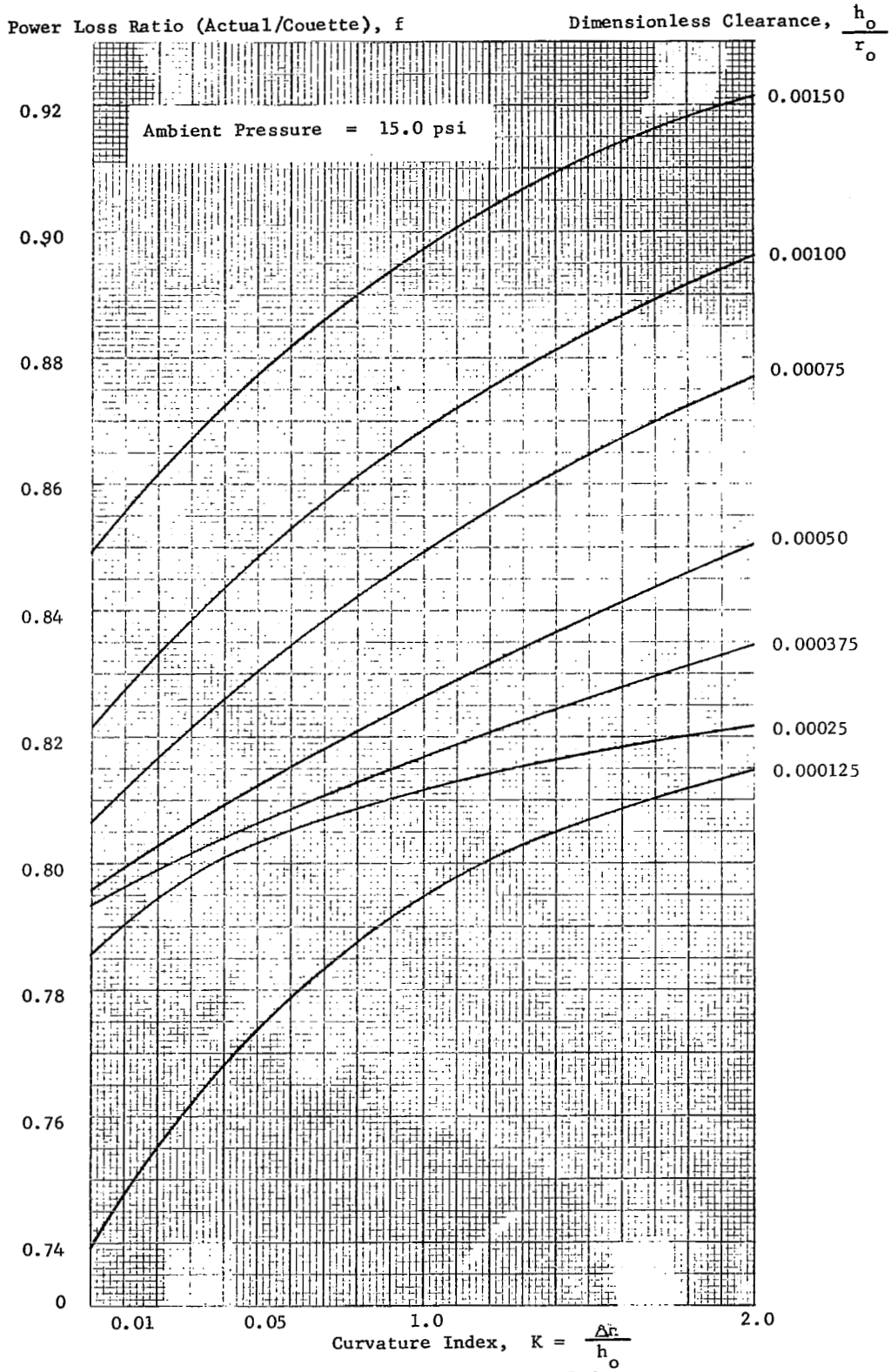

Fig. 58 Power Loss Ratio Vs. Curvature Index

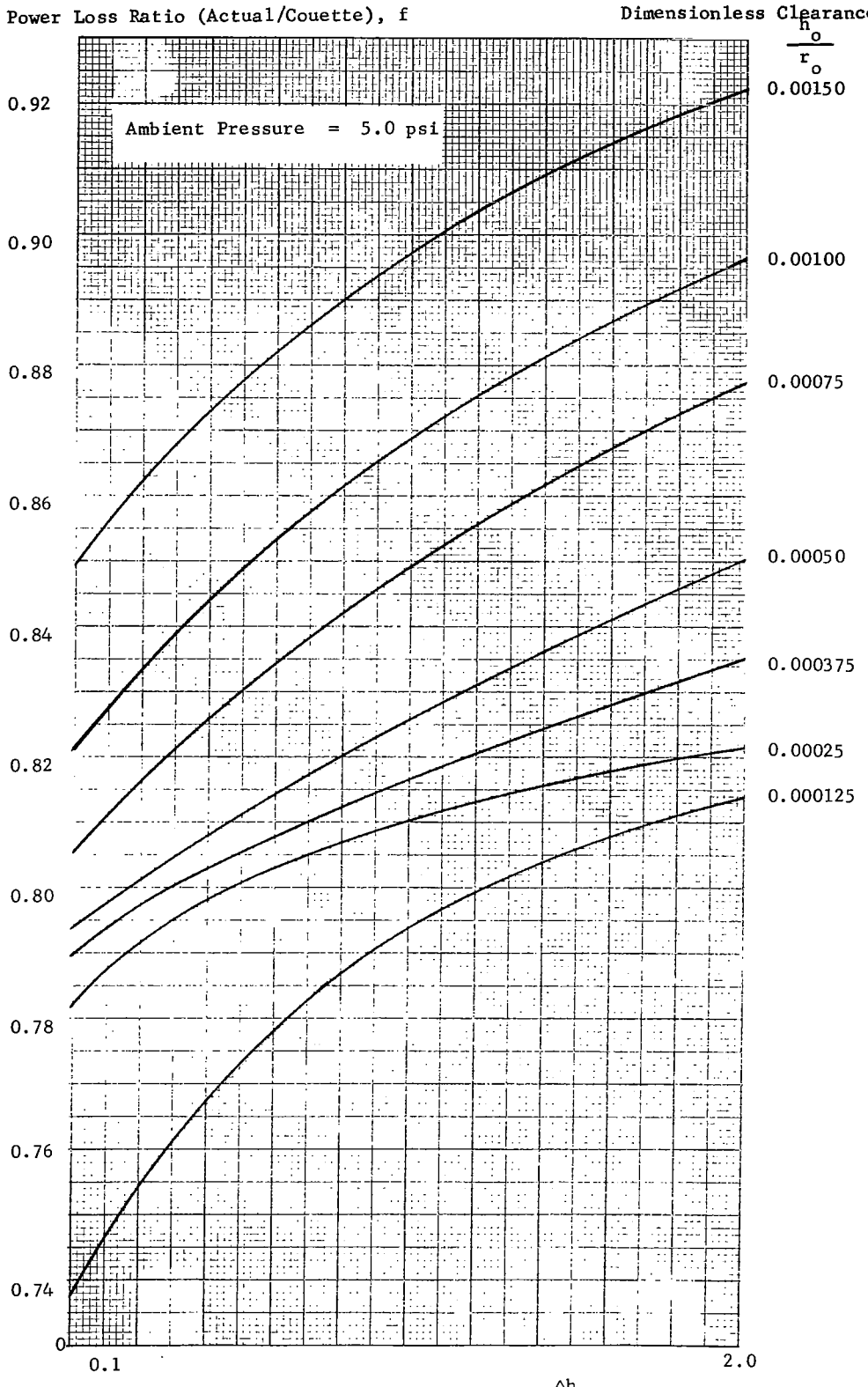

Fig. 59 Power Loss Ratio Vs. Curvature Index

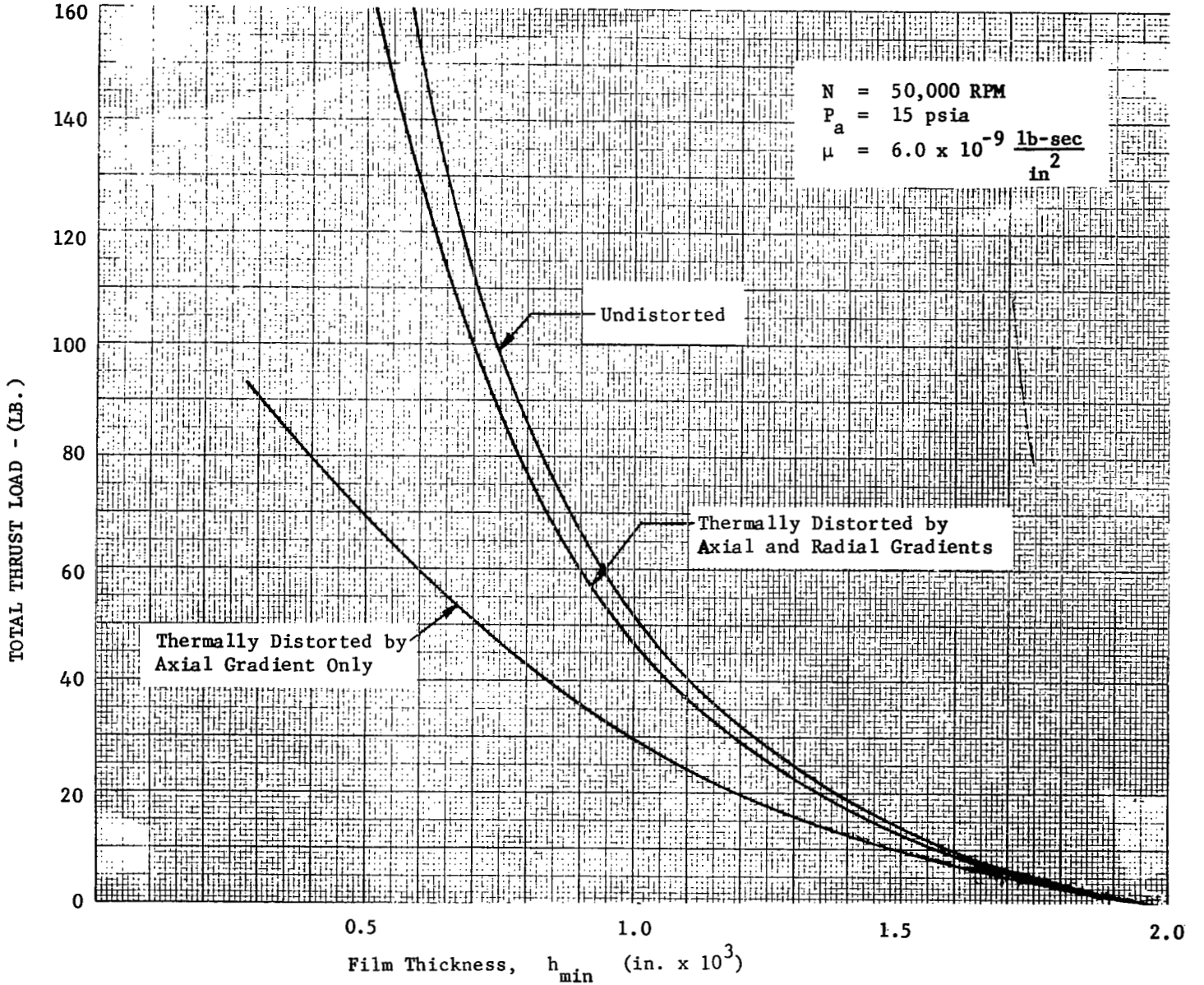

Fig. 60 Load Curves for Thrust Bearing, N = 50,000 RPM

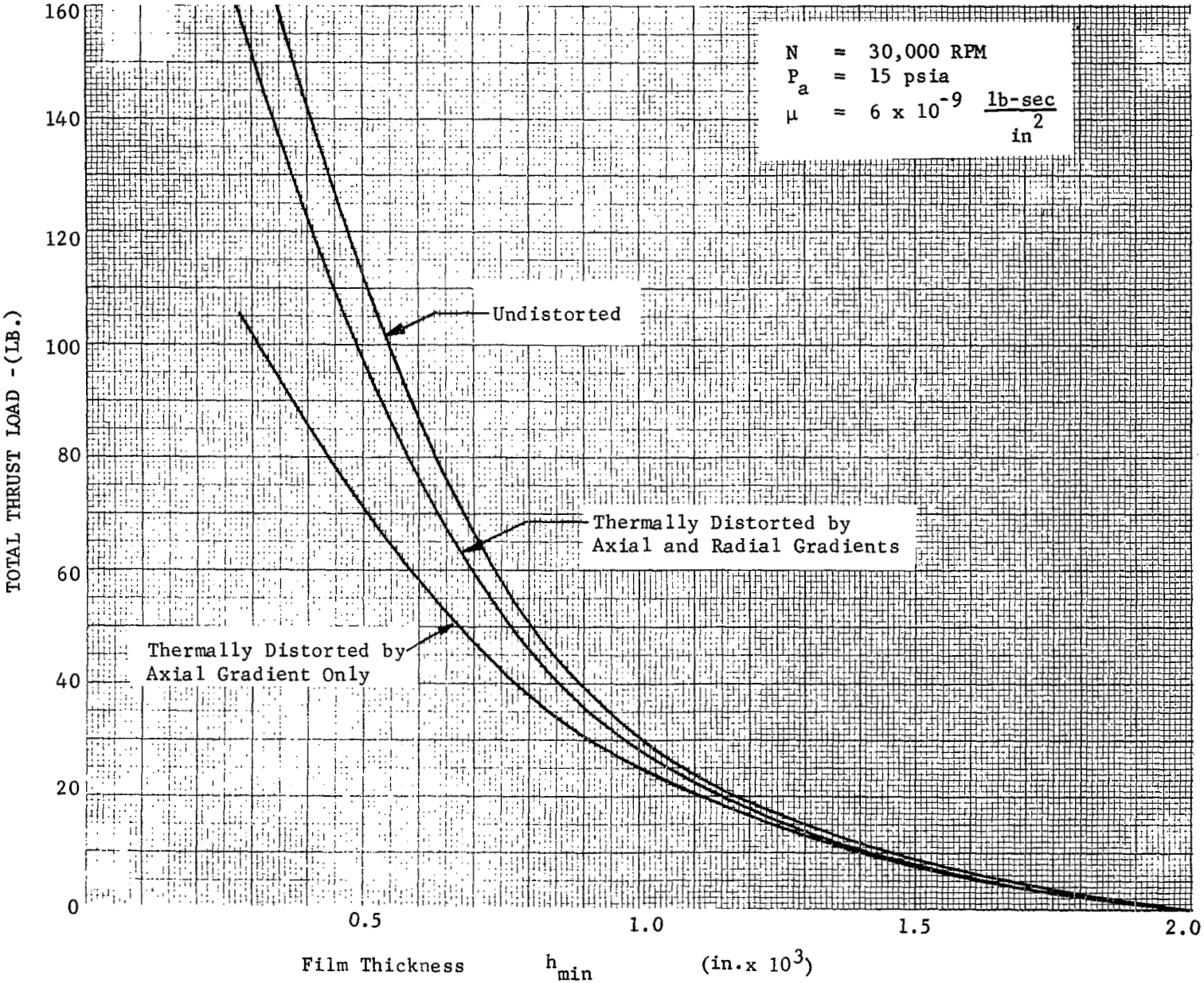

Fig. 61 Load Curves for Thrust Bearing, N = 30,000 RPM

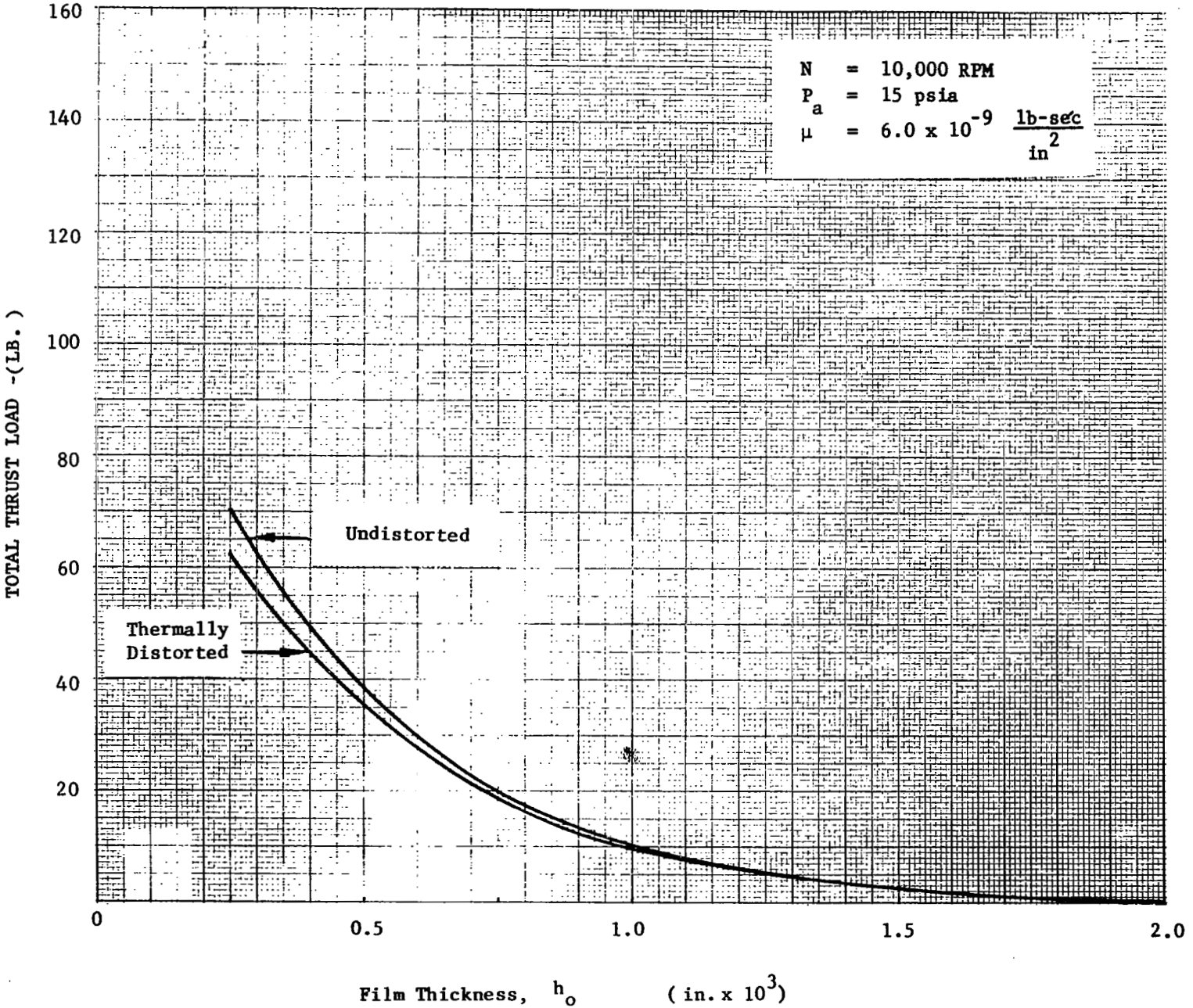

Fig. 62 Load Curves for Thrust Bearing, N = 10,000 RPM

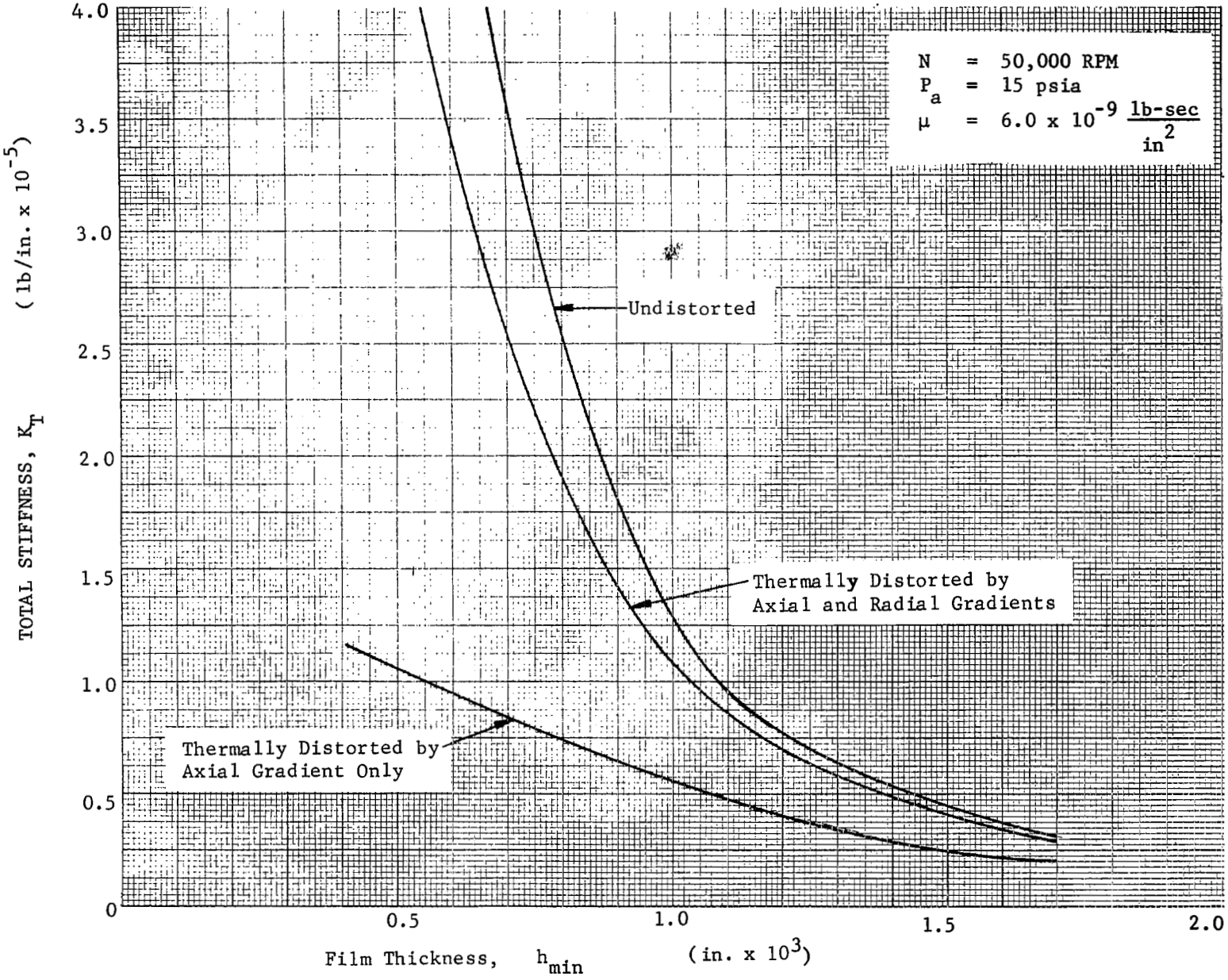

Fig. 63 Stiffness Curves for Thrust Bearing, N = 50,000 RPM

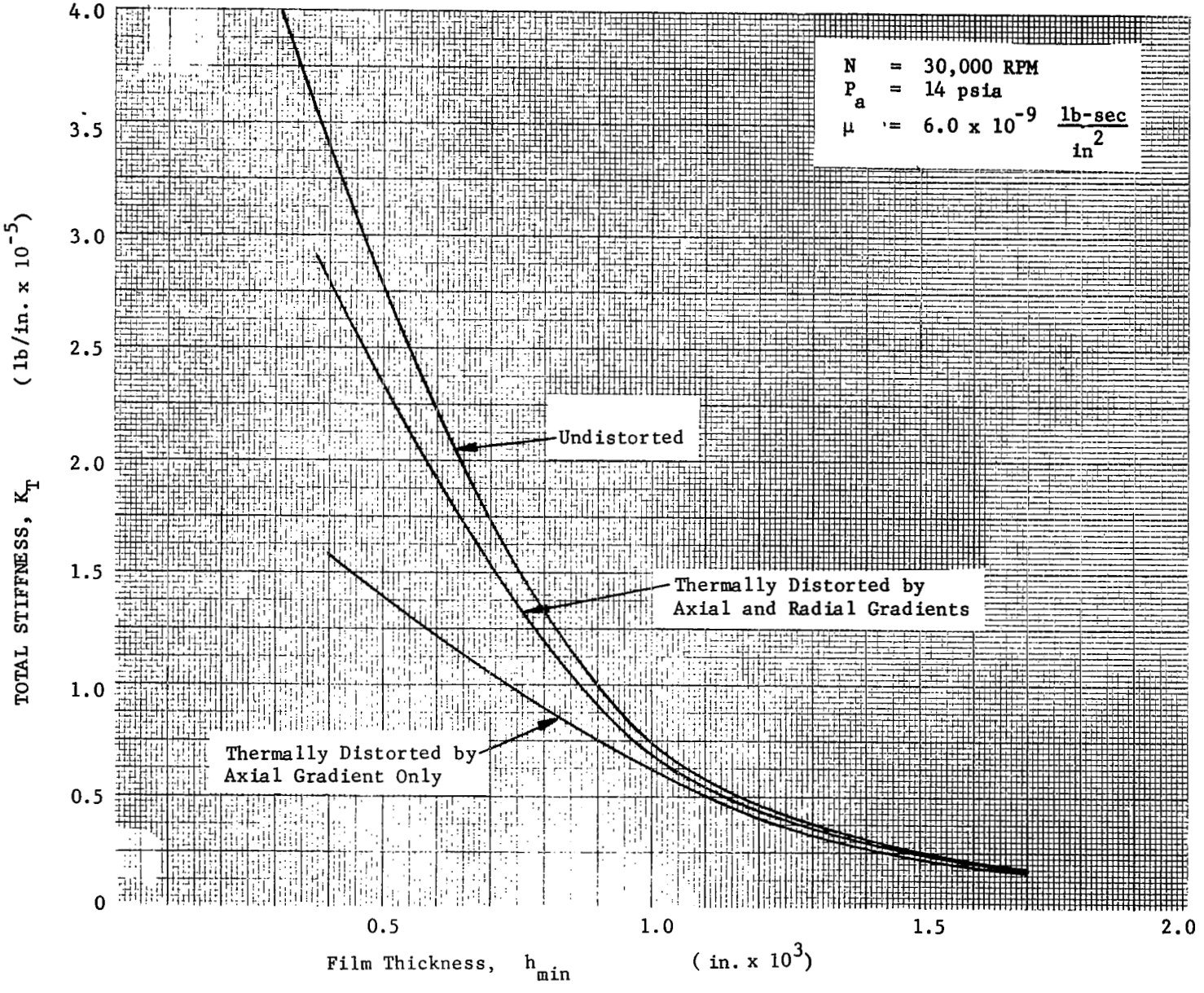

Fig. 64 Stiffness Curves for Thrust Bearing, N = 30,000 RPM

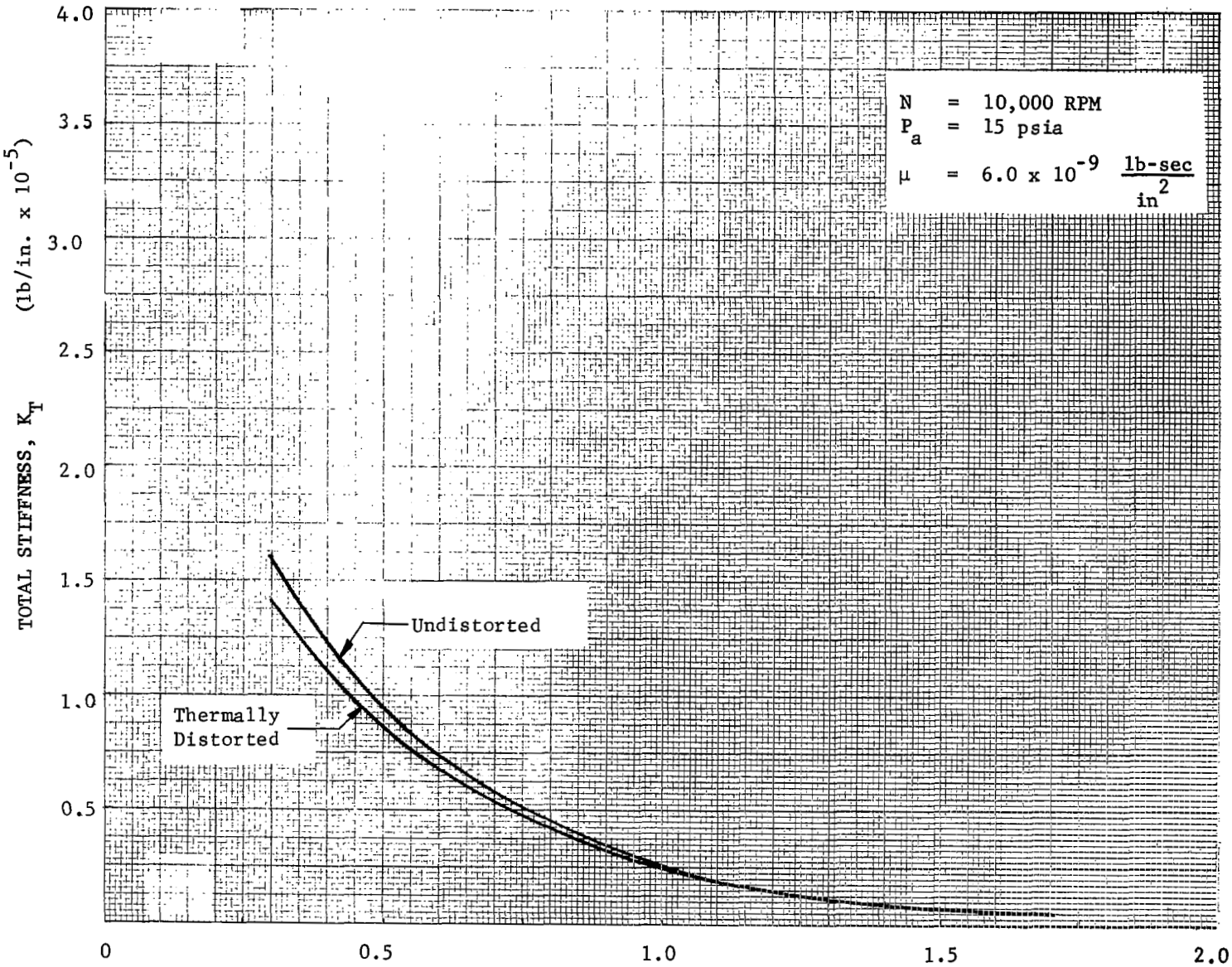

Fig. 65 Stiffness Curves for Thrust Bearing, N = 10,000 RPM

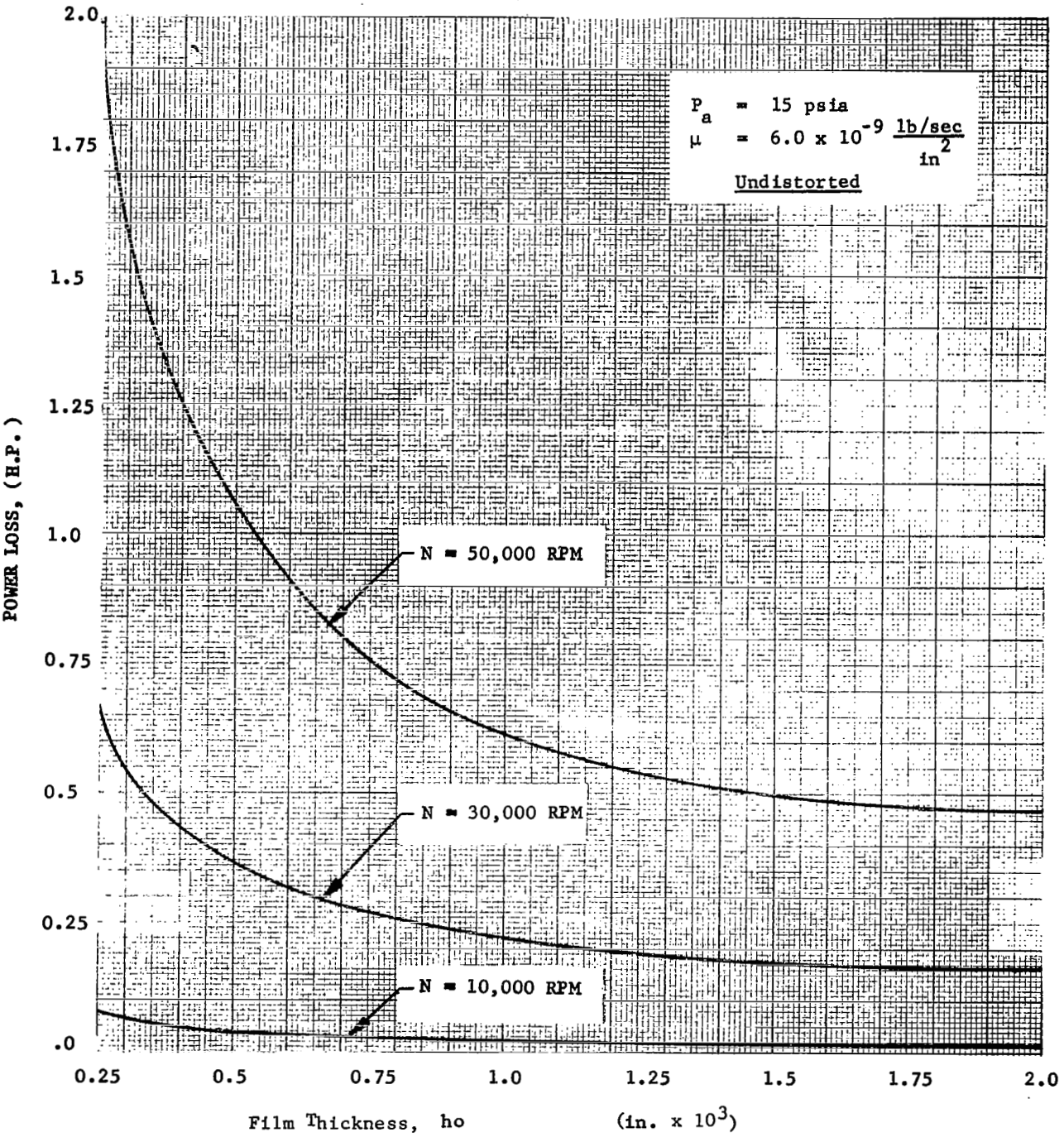

Fig. 66 Power Loss Curves for Thrust Bearing

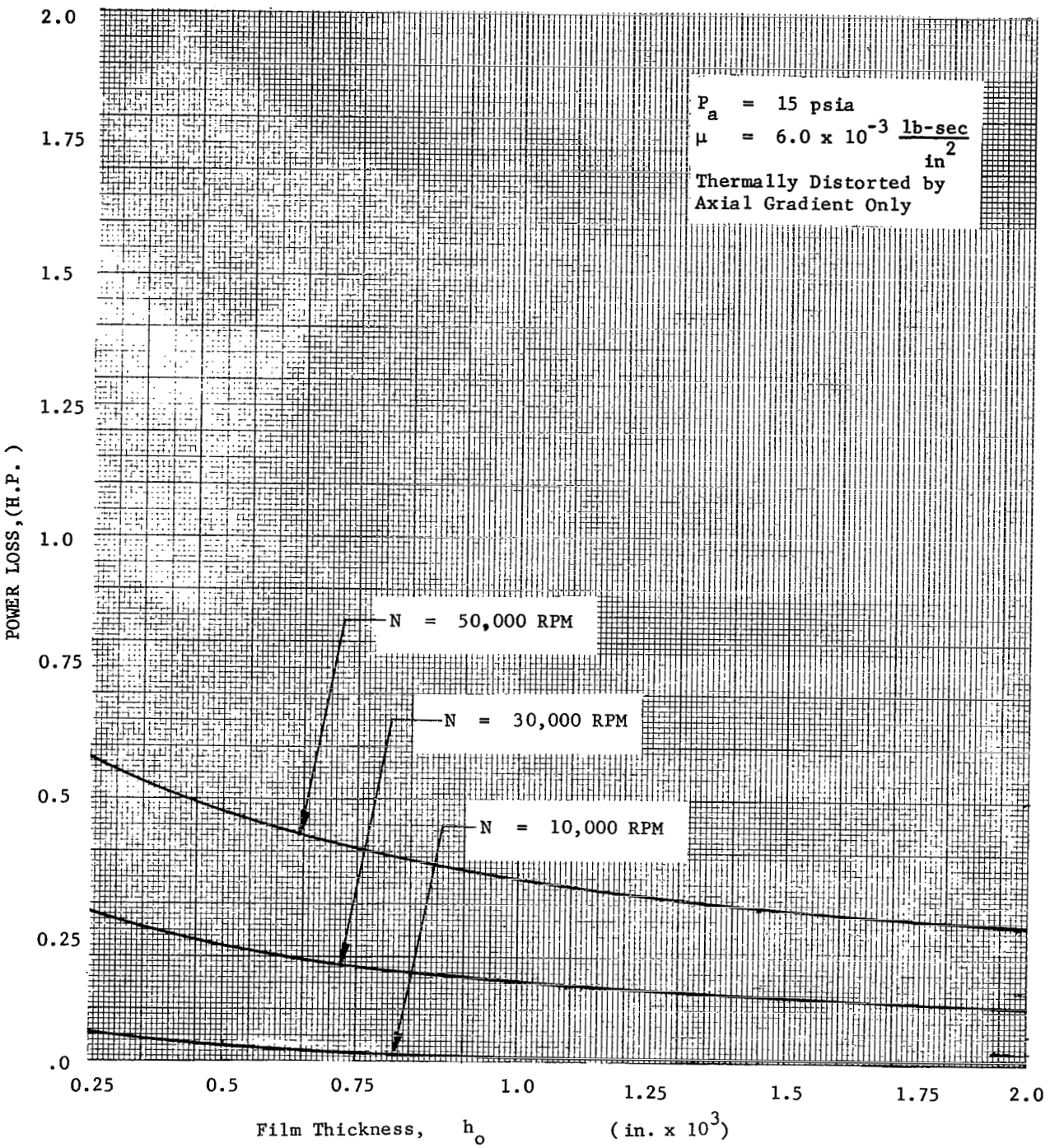

Fig. 67 Power Loss Curves for Thrust Bearing

REFERENCES

1. Cheng, H.S., Castelli, V., Wilson, D. and Arwas, E.B. "Research and Development of High Temperature Gas Bearings, TASK I - Gas Bearing Screening Analysis" Mechanical Technology Inc. Technical Report MTI-67TR41, June 23, 1967.

2. Curwen, P.W. "Research and Development of High Performance Axial-Flow Turbomachinery, Volume 2 - Design of Gas Bearings", NASA CR-801 June 1967, MTI report 67TR9.

3. Arwas, E.B. and Malanoski, S.B. "Tilting Pad Journal Bearings, Section 6.4. Design of Gas Bearings Volume 1: Design Notes" MTI Publication June 1967.

4. Gunter, E.J., Hinkle, J.G., Fuller, D.D. "Design Guide for Gas-Lubricated Tilting-Pad Journal and Thrust Bearings with Special References to High-Speed Rotors," Franklin Institute Research Laboratory Report I-A2922-3-1, U.S. Atomic Energy Commission Report NYO-2512-1 dated November 1964.

5. McCabe, J.T., Shapiro, W, and Chu, T.Y. "Research and Development of High-Performance Axial-Flow Turbomachinery, Volume 3 - Design of Backup Gas Bearings," NASA-CR-802 June 1967.

6. Peterson, M.B. et,al "Interim Report, Analytical and Experimental Investigation of Gas Bearing Tilting-Pad Pivots," Mechanical Technology Inc. Technical Report MTI-67TR84, November 1967.

7. Lund, J.W. "Stiffness and Damping Properties of Gas Bearings for Use in Rotor Dynamics Calculations," Paper No. 68-LUBS-19, presented at the Second International Symposium on Gas Lubrication, June 17-20, 1968, Las Vegas, Nevada.

8. Chu, T.Y., McCabe, J.T. and Elrod, H.G. "Stability Consideration for a Gas-Lubricated Tilting-Pad Journal Bearing, Part 1: Analytical Methods," Journal of Lubrication Technology Transaction of the ASME, Vol. 90. Series F, No. 1 Jan. 1968, pp. 162-172.

9. Licht, L. "Experimental Study of Foil Journal Bearing" Presentation at the Quarterly ONR Gas-Lubrication Meeting," February 1968, Cleveland, Ohio.

10. Licht, L, "On Experimental Study of Elastohydrodynamic Lubrication of Foil Bearings," Journal of Lubrication Technology, Transactions of the ASME. Vol. 90, Series F, No. 1, January 1968. pp. 199-221.

11. Eshel, A, and Elrod, H.G. "The Theory of the Infinitely Wide, Perfectly Flexible, Self-Acting Foil Bearing" Journal of Basic Engineering, Trans. ASME, Series D. Vol. 87, No. 4, Dec. 1965, pp. 831-836.

12. Barlow, E.J. "Self-Acting Foil Bearings of Infinite Width" Ampex Corporation Research Report, RR65-14, Jan. 1966.

13. Huckabay, A. and Stahl, A.F. "Analyzation, Design, Fabrication and Testing of a Foil Bearing Rotor Support System," Final Technical Report RR 66-21 June 1966, Ampex Corporation.

References (continued)

14. Whipple, R.T.P. "Herringbone Pattern Thrust Bearing" Atomic Energy Research Establishment, Harwell, Berkshire, England, T/M 29.

15. Muijderman, E.A. "Spiral Groove Bearings," thesis, Technological University, Delft, Holland, Philips Research Report Supplement, No. 2, 1964.

16. Pan, C.H.T. and Sternlicht, B. "Thermal Distortion of Spiral-Grooves Gas-Lubricated Thrust Bearing Due to Self-Heating" Journal of Lubrication Technology, Transactions of the ASME, Volume 89, Series F, No. 2, April 1967.

17. Burgdorfer, A, "The Influence of the Molecular M an Free Path on the Performance of Hydrodynamic, Gas-Lubricated Bearings," Journal of Basic Engineering T ansactions of ASME, March 1959, pp. 94-100.

18. Castelli, V., Pirvics, J. "Equilibrium Characteristics of Axial Groove Gas-Lubricated Bearings" Journal of Lubrication T chnology, Trans. ASME Series F. Vol. 89, 1967, pp. 177-196.

19. Castelli V, and Stevenson, C.H. "A Semi-Implicit Numerical Method for Treating the Time Transient Gas Lubrication Equation," Journal of Lubrication Technology, Trans. of ASME, Series F, Vol. 90, 1967, pp. 153 157.